

DYNAMIC PROPERTIES OF BEAUFORT SEA SOILS

CENTRE FOR NEWFOUNDLAND STUDIES

**TOTAL OF 10 PAGES ONLY
MAY BE XEROXED**

(Without Author's Permission)

DAN YANG





National Library
of Canada

Acquisitions and
Bibliographic Services Branch

395 Wellington Street
Ottawa, Ontario
K1A 0N4

Bibliothèque nationale
du Canada

Direction des acquisitions et
des services bibliographiques

395, rue Wellington
Ottawa (Ontario)
K1A 0N4

Your file *Votre référence*

Our file *Notre référence*

The author has granted an irrevocable non-exclusive licence allowing the National Library of Canada to reproduce, loan, distribute or sell copies of his/her thesis by any means and in any form or format, making this thesis available to interested persons.

L'auteur a accordé une licence irrévocable et non exclusive permettant à la Bibliothèque nationale du Canada de reproduire, prêter, distribuer ou vendre des copies de sa thèse de quelque manière et sous quelque forme que ce soit pour mettre des exemplaires de cette thèse à la disposition des personnes intéressées.

The author retains ownership of the copyright in his/her thesis. Neither the thesis nor substantial extracts from it may be printed or otherwise reproduced without his/her permission.

L'auteur conserve la propriété du droit d'auteur qui protège sa thèse. Ni la thèse ni des extraits substantiels de celle-ci ne doivent être imprimés ou autrement reproduits sans son autorisation.

ISBN 0-315-86611-X

**DYNAMIC PROPERTIES OF
BEAUFORT SEA SOILS**

By

© Dan Yang, B.Eng.

A thesis submitted to the School of Graduate Studies
in partial fulfillment of the requirements for the degree of
Master of Engineering

Faculty of Engineering and Applied Science
Memorial University of Newfoundland

December, 1992

St. John's

Newfoundland

Canada

Abstract

A study of the deformation behavior of marine soil subjected to long term cyclic loading is presented in this thesis. The study includes both experimental data and analytical predictions. Constitutive relationships relevant to time-dependent deformation behavior of marine cohesive soil under long term cyclic loading are derived based on a number of classic rheological models. The experimental method for determining the creep function is described. Long term cyclic loading tests were conducted on a load-controlled cyclic triaxial system. The theoretical predictions of the deformations are presented and compared to laboratory results. The potential applications of each rheological model to marine geotechnical engineering are discussed.

This thesis also presents the results of an investigation performed to study the liquefaction potential or cyclic strength of four soils from the Beaufort Sea and one from Newfoundland. Results from the different soils are compared under different drainage conditions and overconsolidation ratios. The effects of cyclic stress ratio, dilatancy and mean particle size were also studied and are presented. The stress-strain relationships of the soils are demonstrated and discussed.

An understanding of the stability threshold and dynamic stiffness behavior of marine soils under cyclic loading is required in the dynamic analysis of offshore structures subjected to earthquake excitation or storm wave action. Therefore, the third objective of this experimental investigation was to quantify the stability threshold and dynamic modulus for saturated Beaufort Sea soils under different over-consolidation ratios. The laboratory experiments were conducted on a load-controlled cyclic triaxial system.

Acknowledgements

The author would like to acknowledge the valued guidance and assistance received from many people. Especially Dr. Jack I. Clark and Mr. Mike Paulin without whose help and advice this thesis would not have been possible. A great debt is owed to Dr. Clark, my supervisor, for his motivated and continuous support throughout the project. Dr. Farrokh Poorooshab and Dr. Mervin A. Marshall provided much help and encouragement. I would also like to thank Pankaj Jain, Sanjay Singh, Daniel Nwosu, Ranjith Liyanapathirana, and Prasad Kavuri, Engineering graduate students, Mr. John F. Cross, Research Engineer at Oceans Ltd., and people in the wave tank, soils laboratory and structures laboratory at the Faculty of Engineering, for their assistance through my M.Eng. program. Finally, I wish to thank Mr. David L. Greening and Ms. Karen Muggeridge for their support in the preparation of this thesis.

The samples investigated in this project were provided by Golder Associates as authorized by Gulf Canada Resources Ltd., Calgary, Atlantic Geoscience Center – Bedford Institute of Oceanography, Dartmouth, and Energy, Mines and Resources Canada, Ottawa.

Contents

1	Introduction	1
1.1	Background	1
1.2	Objectives	2
1.3	Scope of Work	2
2	Review of Literature	4
2.1	Cyclic Strength and Liquefaction Potential	4
2.1.1	Factors Affecting Liquefaction Potential and Cyclic Strength of Cohesionless Soils	4
2.1.2	Factors Affecting Cyclic Characteristics of Cohesive Soils . .	11
2.2	Stability Threshold and Cyclic Strength Degradation	15
2.2.1	Definition of the Stability Threshold	15
2.2.2	Degree of Strength Degradation	15
2.3	Cyclic Stress-Strain Relationship	16
2.3.1	Hyperbolic Model	16
2.3.2	R-O Model	18
2.3.3	Normalized Behavior of Offshore Clay	19
3	Instrumentation for Cyclic Triaxial Measurements	20
3.1	Historical Development of Cyclic Triaxial Systems	20
3.2	Experimental Setup	23
3.2.1	Triaxial Cell	25
3.2.2	Cyclic Loading System	26

3.2.3	Back Pressure Saturation and Pore Pressure Measurement Systems	26
3.2.4	Volume Change Measurement Device	29
3.2.5	Axial Deformation Measurement Setup	32
3.3	Data Acquisition and Control System	32
3.3.1	Data Acquisition and Control System	32
3.3.2	Software Used	34
3.3.3	Signal Conditioning	34
3.4	Calibration Procedures	36
3.4.1	Calibration of Pressure Transducers	36
3.4.2	Calibration of LVDT	38
3.4.3	Calibration of Volume Change Transducer	38
3.4.4	Calibration of Load Cell	38
4	Identification and Preparation of Investigated Soils and Test Procedures	40
4.1	Types of Soils Tested	40
4.1.1	Sands	40
4.1.2	Silts	42
4.1.3	Clays	47
4.2	Sample Preparation Methods	53
4.2.1	Remoulded Nerlerk Sands	53
4.2.2	Remoulded Lundrigan Silt	53
4.2.3	Intact Marine Silt, Shelf Silty Clay, Shelf Clay, Beaufort Sea Clay and Slightly Disturbed Nerlerk Mud	54
4.3	Back Pressure Saturation	54
4.4	Consolidation	55
4.5	Rates of Loading	56
4.6	Cyclic Wave Forms	56

5	Deformation Characteristics and Predictions Under Long Term Cyclic Loading	57
5.1	Theoretical Derivations	58
5.1.1	Maxwell Model	60
5.1.2	Kelvin-Voigt Model	61
5.1.3	Standard Linear Model	62
5.1.4	Burgers Model	63
5.2	Test Materials and Load Form	64
5.3	Description of Results	65
5.4	Comparison Between the Theoretical and Test Results	71
5.5	Determination of Creep Function – Creep Test	76
6	Liquefaction Potential and Cyclic Strength	78
6.1	Criteria of Liquefaction and Cyclic Strength	79
6.2	Soil Types and Test Procedures	80
6.3	Analyses of Test Results of Cohesionless Soils	80
6.3.1	Effect of Cyclic Stress Ratio	80
6.3.2	Effect of Drainage	81
6.3.3	Effect of Dilatancy	84
6.4	Dynamic Behavior of Nerlerk Mud and Lundrigan Silt	84
6.4.1	Effect of Over-Consolidation Ratio	86
6.4.2	Effect of Mean Particle Size	88
6.5	Stress-Strain Relationship	88
6.6	Liquefaction Potential	89
6.7	Cyclic Strength	91
7	Stability Threshold and Dynamic Stiffness of Saturated Clays	93
7.1	Stability Threshold	93
7.1.1	Test Procedures	94
7.1.2	Test Results	94
7.1.3	Discussion	100

7.1.4	Comparison with Other Results	103
7.2	Dynamic Young's Modulus	103
7.2.1	Test Results	106
7.2.2	Discussion	106
8	Conclusions	112
8.1	Deformation under Long Term Cyclic Loading	112
8.2	Liquefaction Potential and Cyclic Strength	113
8.3	Stability Threshold and Cyclic Modulus	113
9	References	115
	Appendix A	124
A.1	Derivation of Equations 4.3 and 4.4	124
A.2	Derivation of Equations 4.7 and 4.8	125
A.3	Derivation of Equations 4.10 and 4.11	125
	Appendix B	127
B.1	Typical Results of u/σ_c (or u/σ'_p for OC specimens) vs N and ϵ_a vs N in Chapter 7	127

List of Figures

2.1	Effect of Specimen Preparation Method (After Mulilis et al., 1978).	5
2.2	Effect of Loading Wave Form on Cycles to Initial Liquefaction for Moist-Tamped Specimen (After Mulilis et al., 1978).	6
2.3	Effect of Specimen Size (After Wong et al., 1975).	8
2.4	Cyclic Stress Ratio at the 10th Cycle for Initial Liquefaction vs Relative Density (After Townsend and Mulilis, 1978).	9
2.5	Comparison of Cyclic Loading Strengths of Uniformly Graded and Well-Graded Soils (After Wong et al., 1975).	10
2.6	Effect of Dilatancy (After McCarron and Been, 1990).	14
2.7	Nature of Variation of Dynamic Moduli with Strain (After Skotheim et al., 1985).	17
3.1	Diagrammatic Layout of the Triaxial Apparatus (After Klementev, 1983).	21
3.2	General Layout of a Triaxial Test Unit in NGI (After Berre, 1981).	22
3.3	Assembly of the Experimental Setup.	24
3.4	Triaxial Cell and Control Panel.	27
3.5	Loading System.	28
3.6	Back Pressure Saturation and the Pore Pressure Measurement Systems.	30
3.7	Volume Change Measurement Device.	31
3.8	Data Acquisition and Control System.	33
3.9	Flow Chart for the Data Acquisition and Processing Routine.	35
3.10	Signal Conditioning.	37
3.11	Diagram for Calibration of Volume Change Transducer.	39

4.1	Grain Size Curves for Sands, Silts and Nerlerk Mud Tested.	41
4.2	Plasticity Chart.	43
4.3	Oedometer Curve of Lundrigan Silt.	44
4.4	Compaction Curve.	45
4.5	Location for Marine Silt and Beaufort Sea Clay (After Moran et al., 1989).	46
4.6	Oedometer Curve for Nerlerk Mud (After Golder Associates, 1989).	49
5.1	Maxwell Model.	60
5.2	Kelvin-Voigt Model.	61
5.3	Standard Linear Model.	62
5.4	Burgers Model.	63
5.5	Generalized Burgers Model.	64
5.6	Plot of Applied Loading.	65
5.7	Test Results for Beaufort Sea Clay.	67
5.8	Test Results for NC State Lundrigan Silt ($\sigma_3 = \sigma_c=100\text{kpa}$).	68
5.9	Test Results for OC State Lundrigan Silt ($\sigma_3 = \frac{1}{2}\sigma_c=50\text{kPa}$).	69
5.10	Relationship between Static and Cyclic Loading.	70
5.11	Definition of Rapidly Applied Static Loading.	71
5.12	Theoretical Deformation Curves for BS Clay (Corresponding to Fig- ure 5.7).	73
5.13	Theoretical Deformation Curves for L Silt (Corresponding to Figure 5.8).	74
5.14	Comparison Between Different Models.	75
5.15	Creep Features for Different Materials.	77
6.1	Typical Results from Nerlerk Sands (a) Nerlerk #1 Sand, (b) Nerlerk #2 Sand, and (c) Nerlerk #3 Sand.	82
6.2	Effect of Drainage on Liquefaction Resistance (a) Nerlerk #1 Sand and (b) Lundrigan Silt.	83

6.3	Effect of Dilatancy in Dense Nerlerk #2 (a) CSR=0.25 and (b) CSR=0.625.	85
6.4	Typical Results for (a) Nerlerk Mud and (b) Lundrigan Silt.	87
6.5	Effect of OCR on (a) Nerlerk Mud and (b) Lundrigan Silt.	88
6.6	Effect of D_{50}	89
6.7	Stress-Strain Relationship for (a) Medium Dense Nerlerk #2 Sand, (b) Dense Nerlerk #2 Sand, (c) Nerlerk Mud, and (d) Lundrigan Silt.	90
6.8	(a) Liquefaction Potential for Nerlerk Sands and (b) CSR vs N to Failure for Lundrigan Silt and Nerlerk Mud.	91
7.1	Test Results from Normally Consolidated Nerlerk Mud.	95
7.2	Stability Threshold versus Overconsolidation Ratio.	101
7.3	Effect of Overconsolidation Ratio.	104
7.4	The Definition of Moduli.	105
7.5	Stress-Strain Relationship for Normally Consolidated Shelf Clay.	106
7.6	Dynamic Young's Modulus vs Axial Strain for Nerlerk Mud.	107
7.7	Dynamic Young's Modulus vs Axial Strain for Marine Silt.	108
7.8	Dynamic Young's Modulus vs Axial Strain for Shelf Silty Clay.	109
7.9	Dynamic Young's Modulus vs Axial Strain for Beaufort Sea Clay.	110
B.1	Test Results from Overconsolidated Nerlerk Mud (OCR=2).	128
B.2	Test Results from Overconsolidated Nerlerk Mud (OCR=8).	129
B.3	Test Results from Normally Consolidated Marine Silt.	130
B.4	Test Results from Overconsolidated Marine Silt (OCR=4).	131
B.5	Test Results from Normally Consolidated Shelf Clay.	132
B.6	Test Results from Overconsolidated Shelf Clay (OCR=2).	133
B.7	Test Results from Slightly Overconsolidated Shelf Silty Clay (OCR=1.1).	134
B.8	Test Results from Overconsolidated Shelf Silty Clay (OCR=4.4).	135
B.9	Test Results from Normally Consolidated Beaufort Sea Clay.	136
B.10	Test Results from Overconsolidated Beaufort Sea Clay (OCR=4).	137

List of Tables

- Table 4.1: Physical Properties of Nerlerk Sands.
- Table 4.2: Physical Properties of Silts.
- Table 4.3: Physical Properties of Clays.
- Table 7.1: Published Data on Stability Thresholds.
- Table 7.2: Stability Thresholds for Nerlerk Mud.
- Table 7.3: Stability Thresholds for Marine Silt.
- Table 7.4: Stability Thresholds for Shelf Clay.
- Table 7.5: Stability Thresholds for Shelf Silty Clay.
- Table 7.6: Stability Thresholds for Beaufort Sea Clay.

Nomenclature

The symbols listed below and used in this thesis are defined when they first appear in the text.

A_f = pore pressure parameter at failure

B = Skempton's pore pressure coefficient

c' = effective cohesion intercept

C_C = coefficient of curvature

C_c = compression index

C_s = expansion index

CSR = cyclic stress ratio

C_U = uniformity coefficient

c_v = coefficient of consolidation

D_{50} = mean particle size

D_r = relative density

e_0 = initial void ratio

E_d = dynamic Young's modulus

E_R = elastic modulus during relaxation

G_d = dynamic shear modulus

G_s = specific gravity of solids

$I(t)$ = Heaviside step function

I_P = plastic index

K_c = consolidation ratio

K_0 = coefficient of earth pressure at rest

N = number of cycles

OCR = overconsolidation ratio

p' = mean effective stress

q' = deviatoric stress

$S(t)$ = deformation of the soil layer at a given time

S_t = sensitivity

u = pore pressure (= pore water pressure, u_w , when saturated)

γ = shear strain

γ_r = reference shear strain

γ_d = dry unit weight of soil

γ_{max} = maximum dry unit weight

γ_{min} = minimum dry unit weight

ϵ_a = axial strain

ϵ_c = peak-to-peak strain

η = coefficient of viscosity

μ = elastic modulus

ν = Poisson's ratio

ρ = density of soil

σ_1 = axial stress or longitudinal stress

σ_3 = confining stress or cell stress

σ_c = consolidation stress

σ_d = cyclic deviatoric stress

σ'_p = preconsolidation pressure

σ'_v = vertical effective stress

τ_d = cyclic shear stress

τ_c = relaxation time of displacement

τ_σ = relaxation time of loading

ϕ' = effective angle of internal friction

ω = water content

ω_L = liquid limit

ω_n = natural water content or *insitu* water content

ω_P = plastic limit

Chapter 1

Introduction

1.1 Background

The main areas of concern in offshore geotechnical engineering are connected with the foundations of gravity platforms, pipelines, sediment instability, and piling. It has been reported that liquefaction is a potential problem for the artificial islands used for hydrocarbon exploration in the Beaufort Sea (Ladd et al., 1985). The majority of reported damage to offshore structures has occurred in the Gulf of Mexico, where storms have resulted in sediment slides and slumps. Even in the denser soils of the North Sea, dynamic loading could also be a problem. Eide et al. (1979) reported on observed platform behavior of sandy and clayey sediments in the North Sea over the period 1973-1978. During storms with maximum wave forces up to 45% of the design wave forces, pore-water pressure increases up to 20kPa were recorded. The author thus concluded that storm wave loading does generate excess pore water pressure in both sand and clay, degrades the clay structure, and decreases the stiffness and strength of the soil. Also the sequences resulting from dynamic loadings may induce liquefaction of sandy sediments or strength degradation and significant deformation of clayey deposits. This may influence the design parameters for displacement and stability of offshore platforms.

Exploration and development of natural resources in the Arctic ocean have necessitated the construction of artificial drilling islands in the Alaskan and the Canadian Beaufort Sea. Safe and reliable data obtained from geotechnical inves-

tigations have been of importance for structures using sand fills. Nerlerk is an important case history in this regard, because massive failures of the Nerlerk berm occurred during construction, resulting in cancellation of the project. The present thesis topic was therefore put forward. A number of marine soils from the Beaufort Sea and Lundrigan Silt from St. John's, Newfoundland, were investigated under the conditions of cyclic loading using a cyclic triaxial testing system.

1.2 Objectives

The objectives of this project were:

- (1) to document the dynamic properties including cyclic deformation characteristics, cyclic strength, stability threshold, and cyclic modulus of various types of Beaufort Sea soils and Lundrigan Silt under cyclic loading;
- (2) to develop the constitutive relationship of marine soils for deformation characteristics under long term cyclic loading.

1.3 Scope of Work

The main focus of this research work is directed to the estimation of cyclic strength and liquefaction potential of a number of different marine soils with various overconsolidation ratios and different drainage conditions. The effects of dilatancy, mean particle size and cyclic stress ratio were also studied. The stress-strain relationships of various types of soils under different states of relative density are demonstrated and discussed.

This study also looked into the deformation characteristics and permanent deformation of marine soils under long term cyclic wave loadings with different frequencies and under different confining pressures. In addition, constitutive relationships relevant to time-dependent deformation behavior of ocean cohesive soils under long term wave loadings are derived based on a number of classic rheological models. The theoretical results of the deformation predictions are presented and compared with laboratory results.

The stability threshold and dynamic modulus for saturated Beaufort Sea soils were quantified under different overconsolidation ratios. The investigation also displayed the development of axial deformation, the changes of dynamic pore-water pressure, and the stress-strain relationship during testing.

Eight types of Beaufort Sea soils and Lundrigan Silt were investigated in this study. Types of soil ranged from sand, silt, silty clay to clay. The primary experimental setup is a load-controlled cyclic triaxial system.

The method of normalization for dynamic characterization of the tested soils is adopted in most data reduction.

Chapter 2

Review of Literature

2.1 Cyclic Strength and Liquefaction Potential

The effects of testing procedures and material characteristics on the cyclic triaxial strength of cohesionless soils are reviewed with the intent of categorizing the significance of these factors in relation to the author's experiments. The criteria of cyclic strength and liquefaction potential of soils are described in section 1 of chapter 6. From previous work, it is found that specimen preparation methods, differences between undisturbed and reconstituted specimens, density, and prestraining have major effects on cyclic strength.

Apart from those factors, intermediate but significant effects influencing cyclic strength are confining stress, loading wave form, material grain size (D_{50}) and gradation, overconsolidation ratio (OCR), consolidation stress ratio (K_c), and testing equipment. Other factors having minor effects are loading frequency, specimen size, and friction on the caps and bases (Townsend and Mulilis, 1978).

From the available literature, various factors influencing cyclic triaxial test results are summarized in this chapter.

2.1.1 Factors Affecting Liquefaction Potential and Cyclic Strength of Cohesionless Soils

Specimen Preparation

Mulilis et al. (1978) present data reproduced here as Figure 2.1 which shows that specimens of Monterey No. 0 sand prepared to a relative density of 60%

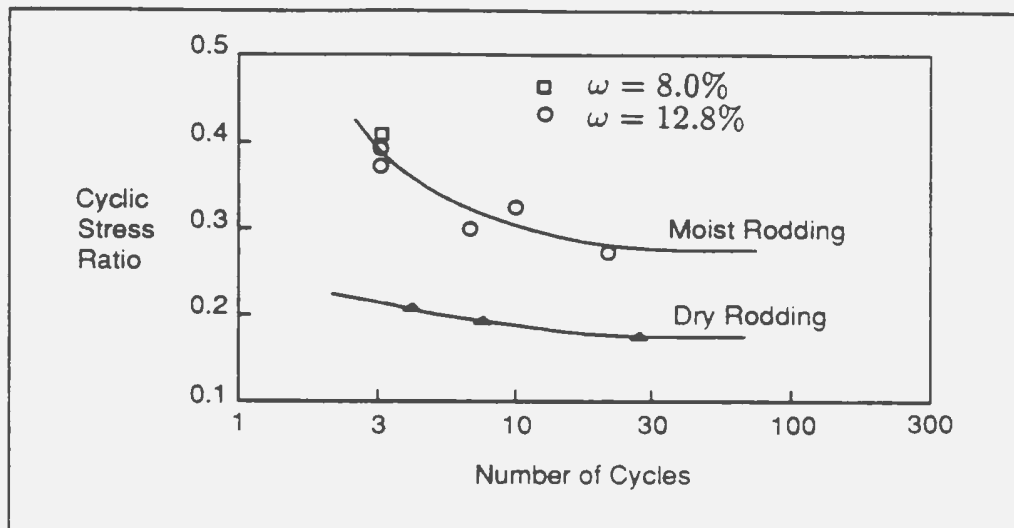


Figure 2.1: Effect of Specimen Preparation Method (After Mulilis et al., 1978).

by “moist tamping” are approximately 58% stronger than comparable specimens prepared by dry rodding.

These results concerning specimen preparation effects on cyclic strength of sands obviously indicate a different structure (fabric) (Mitchell et al., 1976) or K_0 (coefficient of earth pressure at rest) values or both.

Effects of Freezing Intact Specimens

Walberg (1977) examines freezing effects on cyclic strength of undisturbed and reconstituted sand specimens. His results indicate that freezing has practically no effect on cyclic strength, and hence becomes one method of preserving the fabric of clean sands during transportation and storage. The method of course is restricted to free-draining clean sands where pockets of water could not occur and form ice lenses during freezing.

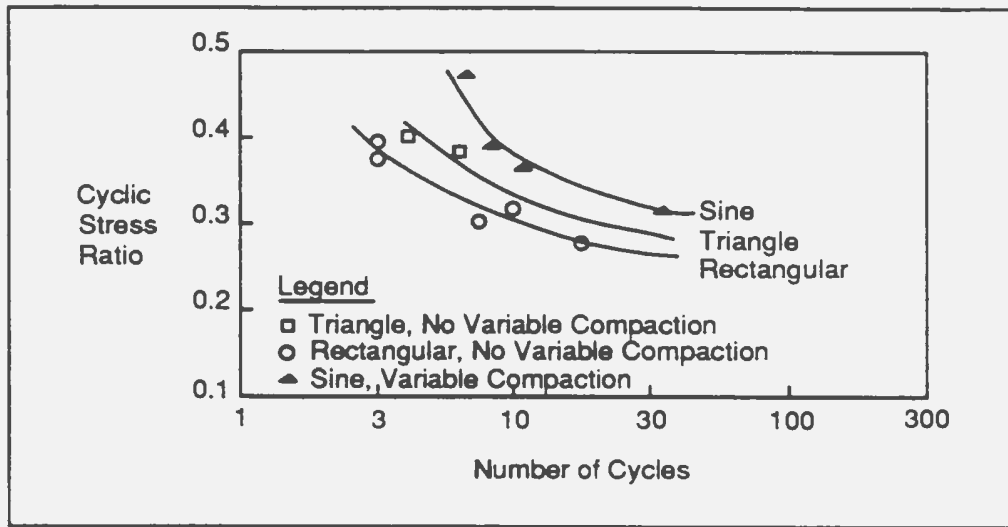


Figure 2.2: Effect of Loading Wave Form on Cycles to Initial Liquefaction for Moist-Tamped Specimen (After Mulilis et al., 1978).

Effects of Confining Stress (σ_3)

The data demonstrate that the cyclic stress ratio (i.e., $\frac{\sigma_d}{2\sigma_3}$) decreases with increasing confining pressure and that the magnitude of this decrease is dependent upon relative density, soil type, and specimen preparation procedure (Ladd and Foott, 1974). Nevertheless, as pointed out by Lee and Focht (1975), for practical purposes within small ranges of pressure, cyclic strength is directly proportional to effective confining pressure.

Effects of Loading Wave Form

The results obtained by Mulilis et al. (1978) demonstrate that rectangular loading wave forms produce cyclic strengths lower than smooth sine wave loading, with degraded rectangular or triangular loading wave forms (Figure 2.2).

Annaki and Lee (1976) observe that when converting from irregular to uniform cycles, extension peaks produce approximately 90% of the total damage, because

the undrained strength of sand is less in extension than in compression. Because of this asymmetric effect existing in triaxial tests, good agreement in converting from irregular to uniform extension cycles is obtained only when the damaging effects of compression and extension cycles are considered separately.

Effects of Frequency on Cyclic Strength

Many scholars have evaluated frequency effects over a range of 1 to 60 cpm (0.016667 to 1 Hz). Wang's experiments (1972) are over a range of 1 to 28 Hz, but the load wave form transforms from rectangular to rounded triangular at the higher frequencies. Lee and Fitton (1969) and Lee and Focht (1975) find that slower loading frequencies produce slightly ($< 10\%$) lower strengths. Wong et al. (1975), Mulilis (1975) and Wang (1972) find that slower frequencies give slightly higher strengths (approximately 10%). Although this is conflicting, it can be safely concluded that frequency effects have only a minor ($< 10\%$) effect on cyclic strength of cohesionless soils.

An interesting sidelight of Wang's work is the effect of confining medium on frequency effects due to a secondary resonant effect. This effect disappears when air is substituted for water as the confining medium.

Effects of Specimen Size and Shape

Wong et al. (1975) compares the effects of size on 70- and 300-mm diameter sand specimens with similar height-to-diameter ratios. Their results, Figure 2.3, show that the 300-mm (12 in) diameter specimen is approximately 10% stronger than the 70-mm (2.8 in) diameter specimen.

Wang (1972) compares the effects of height-to-diameter ratios of 1.0 to 2.3; however, these tests are conducted using full-friction stones. As might be anticipated, the specimens with a height-to-diameter ratio of 1.0 are approximately 20 to 50% stronger than the standard specimens.

Effects of Frictionless Caps and Bases

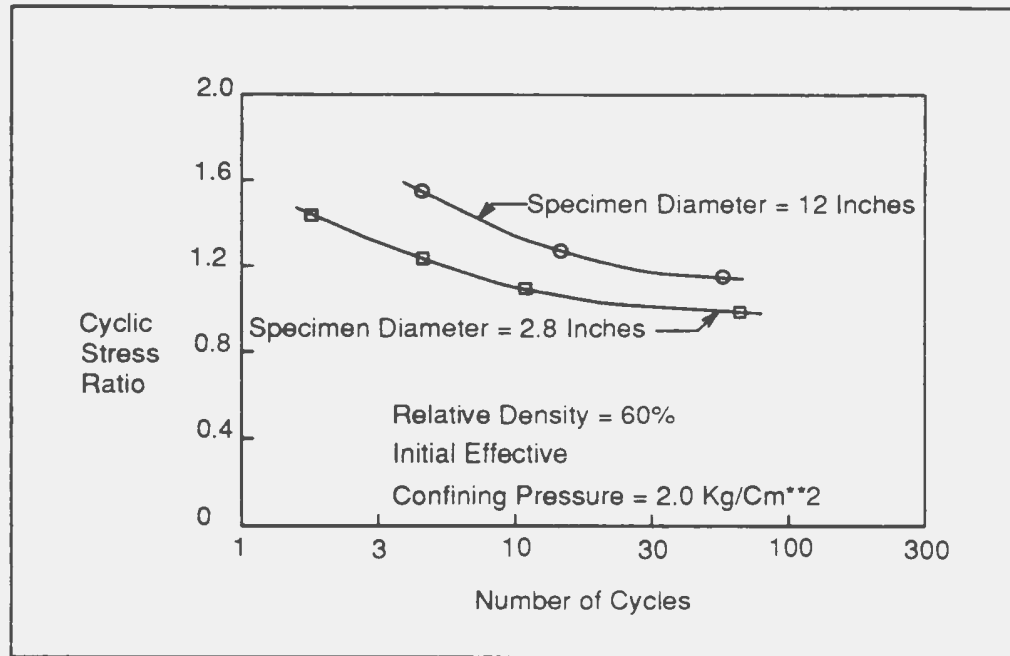


Figure 2.3: Effect of Specimen Size (After Wong et al., 1975).

Mulilis (1975) and Wang (1972) both find that cyclic strength is insensitive to cap and base roughness no matter if the frequencies are higher or lower.

Effects of Relative Density

Seed and Idriss (1971) use a linear relationship to calibrate cyclic stress ratio up to 50% relative density, whereby

$$\frac{\sigma_d}{2\sigma_c} (D_r) = \frac{\sigma_d}{2\sigma_c} (D_r = 50\%) \frac{D_r}{50\%} \quad (2.1)$$

where σ_d is the cyclic deviatoric stress, σ_c is the consolidation stress, and D_r is the relative density.

Mulilis (1975) also shows that cyclic stress ratio to cause liquefaction in 10 cycles is linear with relative density to approximately $D_r = 70\%$. Relative densities above 70% are required for safety against large strains. The data (Townsend and Mulilis, 1978) presented in Figure 2.4 show that the slope of this linear relationship

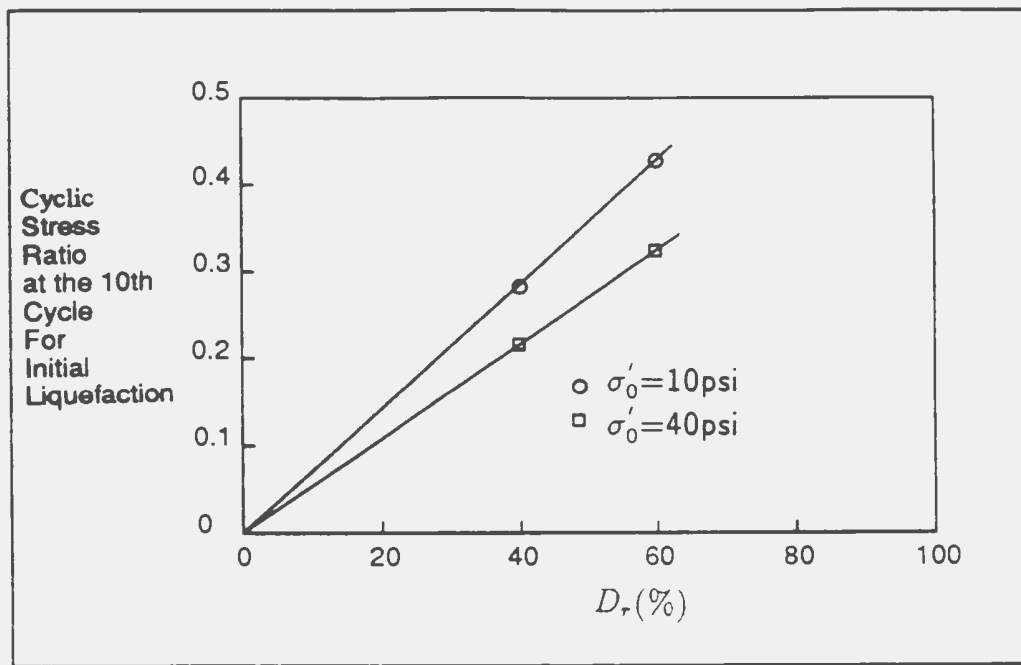


Figure 2.4: Cyclic Stress Ratio at the 10th Cycle for Initial Liquefaction vs Relative Density (After Townsend and Mulilis, 1978).

is a function of confining pressure, σ'_0 . Additional data (Ladd et al., 1977) indicate that this linear relationship is also a function of failure criteria.

Effects of Particle Size and Gradation

Wong et al. (1975) summarize the effects of particle size on cyclic strength, and show a 30-60% increase in cyclic strength to cause $\pm 2.5\%$ and $\pm 10\%$ strain, respectively, as the mean particle size, D_{50} , increases from 0.1 to 30 mm. At the opposite end of the grain size distribution, as the mean grain diameter, D_{50} , continues to decrease to silt and clay sizes, the cyclic strength rapidly increases. Hence, materials having a D_{50} of approximately 0.1 mm possess the least resistance to cyclic stresses.

Wong et al. (1975) also find as shown in Figure 2.5 that well-graded material is somewhat weaker than uniformly graded material. This finding is attributed to a greater densification tendency in well-graded soils. This densification tendency

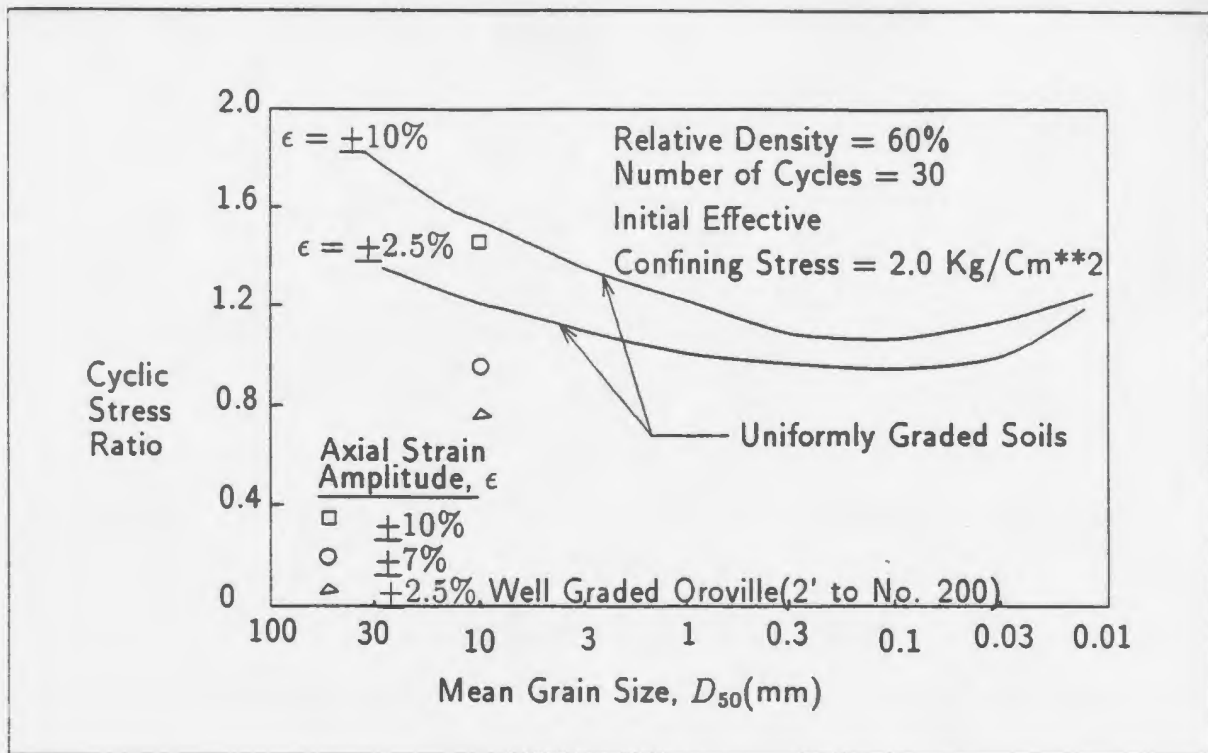


Figure 2.5: Comparison of Cyclic Loading Strengths of Uniformly Graded and Well-Graded Soils (After Wong et al., 1975).

could be reflected as a rise in pore pressure.

Effects of Prestraining

Seed et al. (1988), evaluating the effects of reliquefaction in cyclic triaxial tests, find that once a specimen has liquefied and reconsolidated to a denser structure, despite this densification, the specimen is much more susceptible to liquefaction.

Effects of OCR

Seed and Idriss (1971), Lee and Focht (1975), and Ladd (1976) all present results obtained from sand specimens illustrating that as the OCR increases, the stress ratio required to cause initial liquefaction increases. In addition, this increase in cyclic strength with OCR is a function of the fines content. These results are also confirmed by Ishihara et al. (1978).

Effects of Consolidation Ratio, K_C

The data from anisotropically consolidated tests show that, for a given confining pressure, the maximum deviatoric stress required to cause a critical strain for a specified number of cycles increases with the K_c ratio, where $K_c = \frac{\sigma_1}{\sigma_3}$ (Lee and Seed, 1966).

Castro and Poulos (1977), however, point out the opposite effect, i.e., cyclic strength for a critical strain in a specified number of cycles, should decrease with increasing K_c , as at higher K_c ratios the specimen is initially closer to failure. Furthermore, the data indicating that cyclic strength increases with K_c ratio suggest an unreasonable conclusion that steeper slopes are safer against earthquake loadings. The aforesaid phenomena could be explained by the concept of stress reversal (Lee and Seed, 1966). In anisotropically consolidated tests where no stress reversal occurs (i.e., $\frac{\sigma_d}{2\sigma_c} < \frac{K_c-1}{2}$), the axial stress is always the major principal stress and initial liquefaction does not occur. Conversely, in comparable tests where stress reversal does occur (i.e., $\frac{\sigma_d}{2\sigma_c} > \frac{K_c-1}{2}$), initial liquefaction and associated strains are observed. From these considerations, it is obvious that, as the K_c ratio increases, so must increase the cyclic deviatoric stress, σ_d , and the maximum deviatoric stress in order to achieve stress reversal for a given σ_c .

These results show that in some cases isotropic consolidation will provide conservative estimations of cyclic strength (e.g., when $\frac{\sigma_d}{2\sigma_c} < \frac{K_c-1}{2}$), while in other cases, anisotropic consolidation will provide a lower cyclic strength (e.g., $\frac{\sigma_d}{2\sigma_c} > \frac{K_c-1}{2}$).

2.1.2 Factors Affecting Cyclic Characteristics of Cohesive Soils

Earthquakes and ocean waves often induce severe undrained cyclic shear loading of deposits underlying offshore structures. Such repeated loading degrades the clay structure, changes the pore water pressure, and decreases the stiffness and strength of the soil. The influence of this cyclic degradation on the stability of the clay and supported structure is generally evaluated using laboratory tests, such as cyclic undrained triaxial and cyclic undrained direct simple shear. Investigations of the

behavior of seabed soils, under cyclic triaxial loadings have rarely been reported in the literature; and the present thesis is an attempt in this direction.

Effects of Soil Fabric

Lefebvre and LeBoeuf (1987) indicate in their studies that for structured clays (naturally overconsolidated), pore pressure generated at a given deviatoric stress is essentially independent of the strain rate, while the peak strength envelope is lowered as the strain rate is decreased. For destructured (i.e., normally consolidated) clay, a lower strain rate results in an increase in pore pressure generation during shearing, due to the tendency of the clay skeleton to creep, while the peak strength envelope remains the same. Nevertheless, from a quantitative standpoint, the increase in shear strength caused by an increase in strain rate is similar for both structured and destructured clay, and it is linear for at least five log cycles of strain rate.

Effects of Frequency

Procter and Khaffaf (1984) present their data from cyclic triaxial tests on remoulded clays with load or displacement control. They suggest that only the minimum cyclic stress ratio associated with the fully weakened state has a direct design relevance. The minimum cyclic stress ratio varies with frequency. The value of this limiting stress ratio is constant over the frequency range $\frac{1}{120} Hz \leq f \leq \frac{1}{5} Hz$, and decreases for $f > \frac{1}{5} Hz$. If data from load controlled tests are re-analyzed to account for rate effects on shear strength, then a constant value independent of frequency is observed.

Effects of Temperature

Limiting data indicate that a $20^{\circ}C$ increase in temperature can underestimate σ'_p , the preconsolidation pressure by 20 to 60% for some clays (Ladd et al., 1977). The results published by Ladd et al. (1985) show a 20% change, but the other two tests on low ω (water content) silt samples show little effect.

Effects of Shear Stress Reversal

Results obtained by Konrad (1985) show that unsymmetrical cyclic loading leads to compressive failure, in which the mode of failure is independent of the amount of shear stress reversal. Symmetrical cyclic loading leads to an extension failure characterized by large strains. The normalized cyclic deviatoric stress at failure for tests with $K_c = 2$ is 125% higher than that for tests with $K_c = 1$.

Effects of Dilatancy

The S-shaped effective stress paths for the normally consolidated (NC) specimens shown in Figure 2.6 (where $q' = \frac{\sigma'_1 - \sigma'_3}{2}$ and $p' = \frac{\sigma'_1 + \sigma'_3}{2}$) are unusual for cohesive soils, as they indicate significant dilation near failure. This behavior for cohesive Beaufort Sea soils has been mentioned in the literature (Wang et al., 1982; Jefferies, 1987, 1988). McCarron and Been (1990) have addressed this issue and noted that by consolidating specimens to pressure approximately three times the maximum previous consolidation pressure, this behavior typical of normally consolidated conditions is obtained (see the test T7 in Figure 2.6).

Effects of Shearing Strain Amplitude and Soil Type

The data (Stokoe et al., 1980) show that offshore silty samples degrade more at higher shearing strain amplitudes. This is consistent with data reported for fine-grained soils (Thiers and Seed, 1969; Idriss et al., 1978). In contrast, the data for more silty material (D_{50} equal to 0.041 mm versus D_{50} equal to 0.0075 mm for the specimens mentioned above), show that it stiffens with cyclic loading at strains above approximately 0.03%.

Effects of Plasticity

The general increase of normalized cyclic resistance with increasing plasticity is evident. It has been known since the inception of soil mechanics that clays are less susceptible to densification by vibration than sands. These results suggest a fair

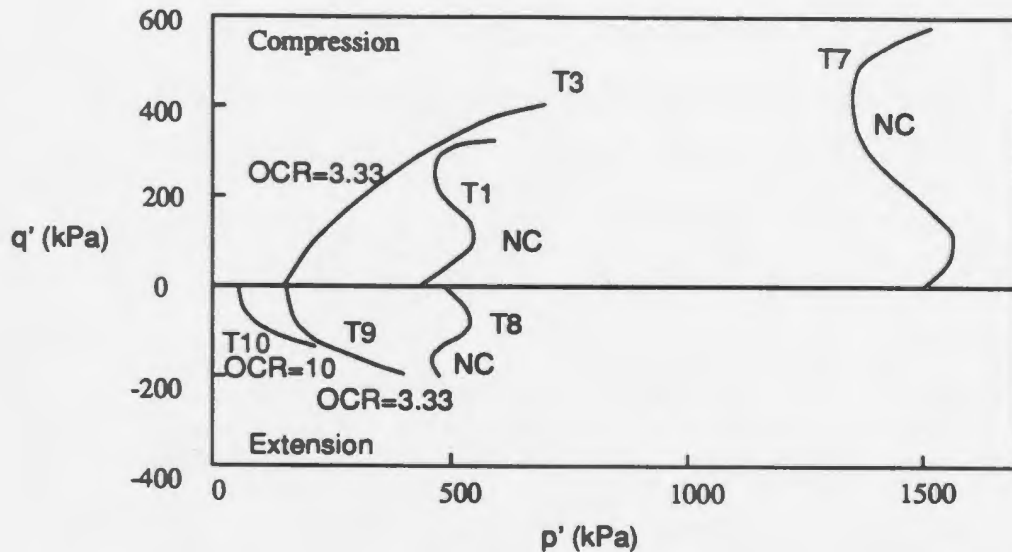


Figure 2.6: Effect of Dilatancy (After McCarron and Been, 1990).

correlation between cyclic resistance and plasticity index, but it seems likely that cyclic resistance depends on other factors in addition to the plasticity.

Effects of Pre-cycling

A series of monotonic, post-cyclic loading tests has shown that undrained shear strength remains essentially unchanged if the cyclic preloading is kept below the stability threshold (Lefebvre et al., 1989). This is because repeated cyclic loading below the threshold causes essentially no damage to the clay structure and leaves the original peak failure envelope unaltered. In addition, pre-cycling causes an apparent overconsolidation of a normally consolidated clay. The stress path followed by the specimen after pre-cycling in monotonic loading is similar to that occurring in a static test of an overconsolidated clay.

2.2 Stability Threshold and Cyclic Strength Degradation

2.2.1 Definition of the Stability Threshold

The cyclic stability threshold is defined as the maximum cyclic deviatoric stress level at which the soil will not suffer failure regardless of the number of applied cycles. It is asymptotic to the cyclic strength curve when defined. In this study, the stability threshold has been assumed to lie between the lowest stress ratio for a test ended by failure and the highest stress ratio for stabilized test. A specimen is considered to be "stabilized" when both pore pressure and axial strain remain practically constant with additional loading cycles.

Cyclic strength parameters presented in this study are normalized with the vertical consolidation pressure for normally consolidated specimens and with the apparent preconsolidation pressure for over-consolidated specimens. This is an extension to the normalization concepts presented by Ladd and Foott (1974).

2.2.2 Degree of Strength Degradation

Undrained cyclic shear loading of clay deposits is induced by earthquakes and ocean wave storms. Under such repeated loading, clay structure deteriorates, pore pressure changes, and consequently the clay stiffness and strength degrade. The influence of cyclic degradation on the stability of clay deposits and supported structures is generally evaluated on the basis of undrained cyclic triaxial and undrained cyclic direct simple shear tests.

Considering that many offshore and onshore clay deposits are overconsolidated rather than normally consolidated, the concept of cyclic degradation of clay stiffness by Idriss et al. (1978) has been extended to include OC clays (Vucetic and Thilakaratne., 1987; Vucetic and Dobry, 1988). The analyses show that for OC clays the cyclic modulus degradation after N cycles can also be modeled by the degradation index, δ , the degradation parameter, t , using the following expression,

$$\delta = \frac{(E_s)_N}{(E_s)_1} = N^{-t} \quad (2.2)$$

where

N = the number of cycles of loading,

E_s = the secant Young's modulus from cyclic triaxial tests, and

t = the slope of $\log \delta - \log N$ curve

This expression is modified for use with shear modulus test results and is defined by:

$$\delta = \frac{G_N}{G_1} = N^{-t} \quad (2.3)$$

where G_1 and G_N equal the secant shear moduli for the first full load cycle and the N th load cycle, respectively, and t equals the slope of the δ vs. load-cycle curve.

2.3 Cyclic Stress-Strain Relationship

The stress-strain relationship of soils under cyclic loading has two obvious features: nonlinearity and hysteresis effect. Many constitutive models have been developed during the recent past. They could reflect the features of soils from different regions. Of these models, the hyperbolic model, the visco-elastic model and the idealized elasto-plastic model are close to the actual stress-strain curves of soils. However, the hyperbolic model and the R-O (Ramberg-Osgood) model are the most commonly-used cyclic constitutive relationships in soil mechanics.

2.3.1 Hyperbolic Model

Based on experimental observations, Hardin and Drnevich (1972) proposed a generalized method according to which the variation of shear stress versus strain of all soils can be approximated by a hyperbolic relation (Hardin-Drnevich Model, abbreviated as H-D model) as (see the experimental data in Figure 2.7)

$$\tau = \frac{\gamma}{\frac{1}{G_{max}} + \frac{\gamma}{\tau_{max}}} \quad (2.4)$$

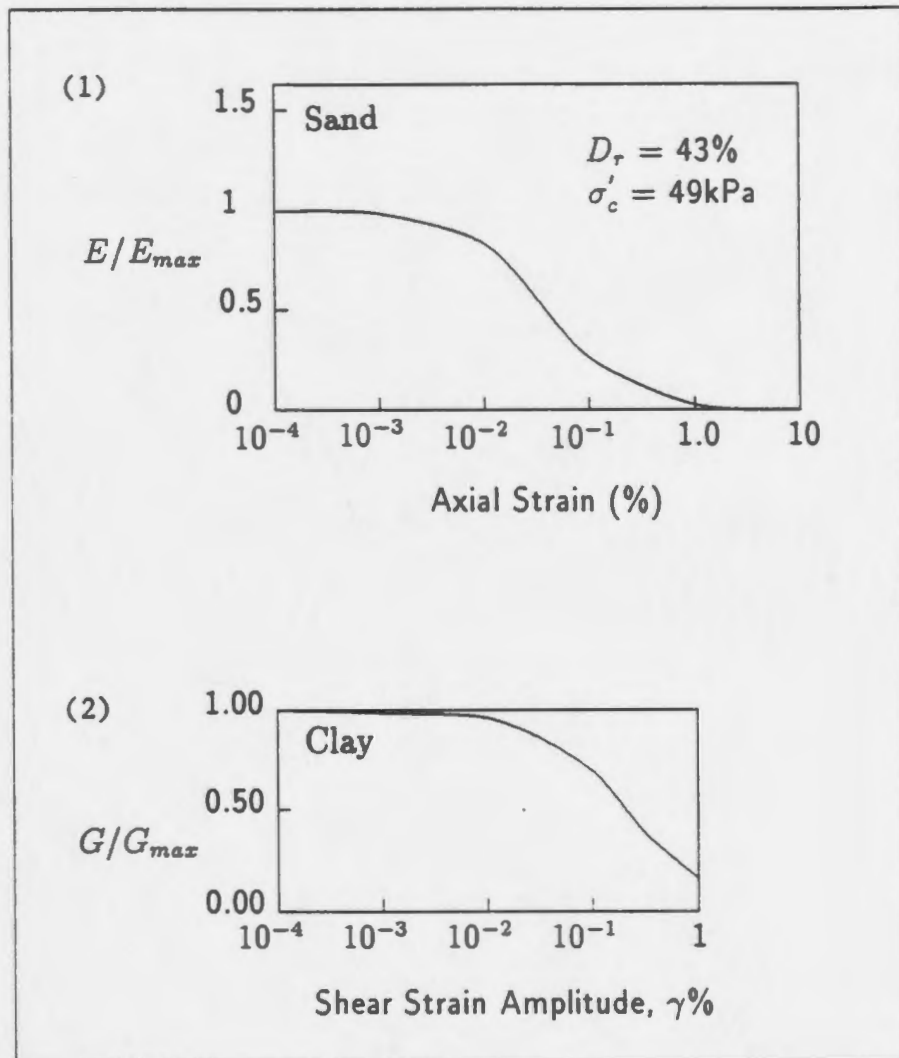


Figure 2.7: Nature of Variation of Dynamic Moduli with Strain (After Skotheim et al., 1985).

where τ is the shear stress, γ is the shear strain, $G_{max} = \frac{\tau_{max}}{\gamma_r}$, γ_r is the reference strain, τ_{max} is the maximum shear stress at failure and can be obtained from Mohr's circle. The relation for τ_{max} can be derived as

$$\tau_{max} = \left\{ \left[\frac{1}{2}(1 + K_0)\sigma'_v \sin\phi' + c' \cos\phi' \right]^2 - \left[\frac{1}{2}(1 - K_0)\sigma'_v \right]^2 \right\}^{1/2} \quad (2.5)$$

where c' is cohesion, ϕ' is the effective angle of friction of the soil, K_0 is the lateral earth pressure coefficient at rest and σ'_v is the vertical effective stress. Eq.(2.5) refers to in situ conditions.

Knowing that $G = \tau/\gamma$ and $G_{max} = \tau_{max}/\gamma_r$, Eq.(2.4) can be rewritten in the form

$$G = \frac{G_{max}}{1 + \frac{\gamma}{\gamma_r}} \quad (2.6)$$

At this point it needs to be mentioned that, the stress-strain relationship of soils is somewhat deviated from that given by Eq.(2.4). Therefore, Eq.(2.6) has to be modified slightly as

$$G = \frac{G_{max}}{1 + \gamma_h} \quad (2.7)$$

where hyperbolic strain

$$\gamma_h = \frac{\gamma}{\gamma_r} [1 + a e^{-b(\gamma/\gamma_r)}] \quad (2.8)$$

and a and b are constants for soils.

Equation (2.7) can now be used to determine the shear modulus of a soil at any given strain level.

2.3.2 R-O Model

The R-O model was first proposed by Sereeter et al. (1974). The expression of the model is as follows:

$$\frac{\gamma}{\gamma_r} = \frac{\tau}{\tau_{max}} \left[1 + \frac{\alpha}{C^{R-1}} \left(\frac{\tau}{\tau_{max}} \right)^{R-1} \right] \quad (2.9)$$

or

$$\frac{G}{G_{max}} = \frac{1}{1 + \frac{\alpha}{C^{R-1}} \left(\frac{\tau}{\tau_{max}}\right)^{R-1}} \quad (2.10)$$

where α , C and R are constants for soils, and G_{max} , γ_r and τ_{max} are the same as in the H-D model.

Based on test data, it is found that the R-O model and the H-D hyperbolic model are basically the same if proper α , C and R values are selected.

2.3.3 Normalized Behavior of Offshore Clay

A procedure for cyclic characterization of normalized behavior of NC and OC clays has been presented and verified by Vucetic (1988). The results show that if a clay exhibits static normalized behavior with respect to the vertical consolidation stress $\bar{\sigma}_{vc}$, it can be characterized along the lines of the SHANSEP method (Ladd and Foott, 1974; Ladd et al., 1977). It also exhibits similar cyclic normalized behavior. In this way, various aspects of the SHANSEP method for static characterization are extended to cyclic loading conditions. In particular, the method proposed can describe cyclically, with relatively fewer cyclic tests, a clay deposit where OCR is varying with depth.

Chapter 3

Instrumentation for Cyclic Triaxial Measurements

3.1 Historical Development of Cyclic Triaxial Systems

Cyclic loading problems in the ocean environment arise from two primary sources: wave action and earthquakes. The physical and mechanical behavior of seafloor soils under such loading conditions has a major influence on the design of offshore structures. The stability of the natural seafloor and excavations is also affected by cyclic loads.

Various systems for cyclic loading in geotechnical engineering have been developed (Klementev, 1983). The simple ones are mechanical, like that of Grainger and Lister (1962). The more sophisticated systems are electro-hydraulic, which enable programable closed-loop controlled loading, such as the system of Cullingford et al. (1972). Hydraulically operated triaxial apparatus can be easily adapted for cyclic loading by adding a hydrodynamic pulsator and by employing limiters to keep the maximum and minimum values of load unchanged. Such a cyclic triaxial system is shown in Figure 3.1.

Figure 3.2 presents the layout of a triaxial system used at the Norwegian Geotechnical Institute (NGI) which is suitable for both static and cyclic loading tests.

Computer-controlled triaxial systems now in use can automatically:

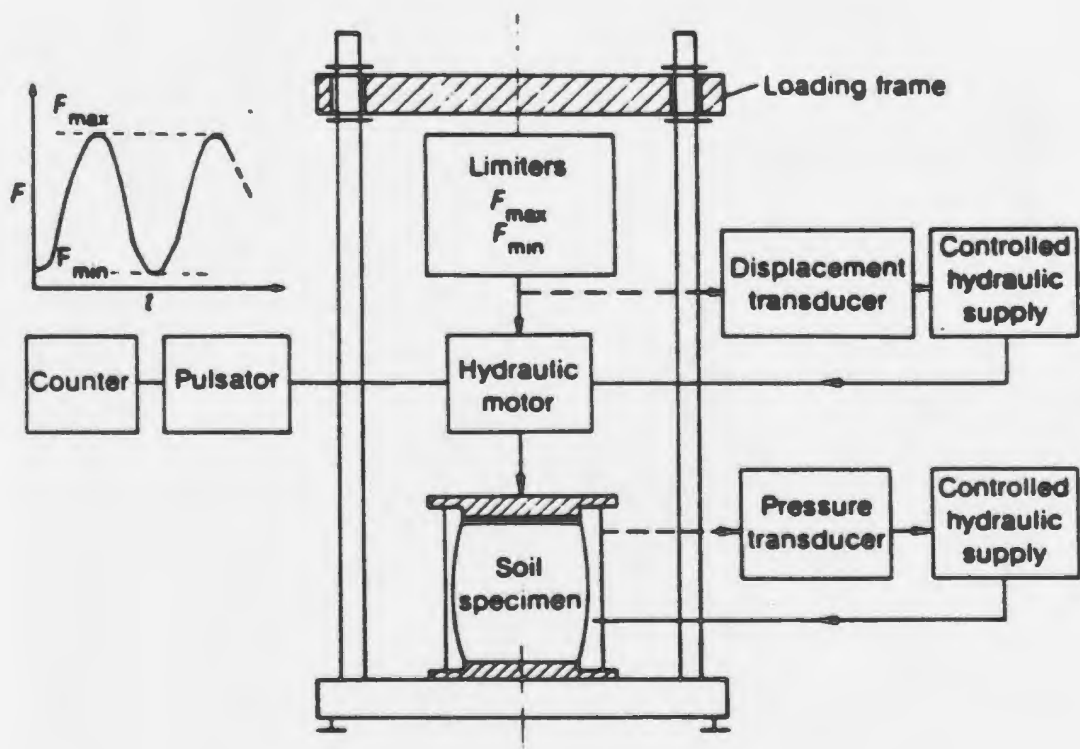


Figure 3.1: Diagrammatic Layout of the Triaxial Apparatus (After Klementev, 1983).

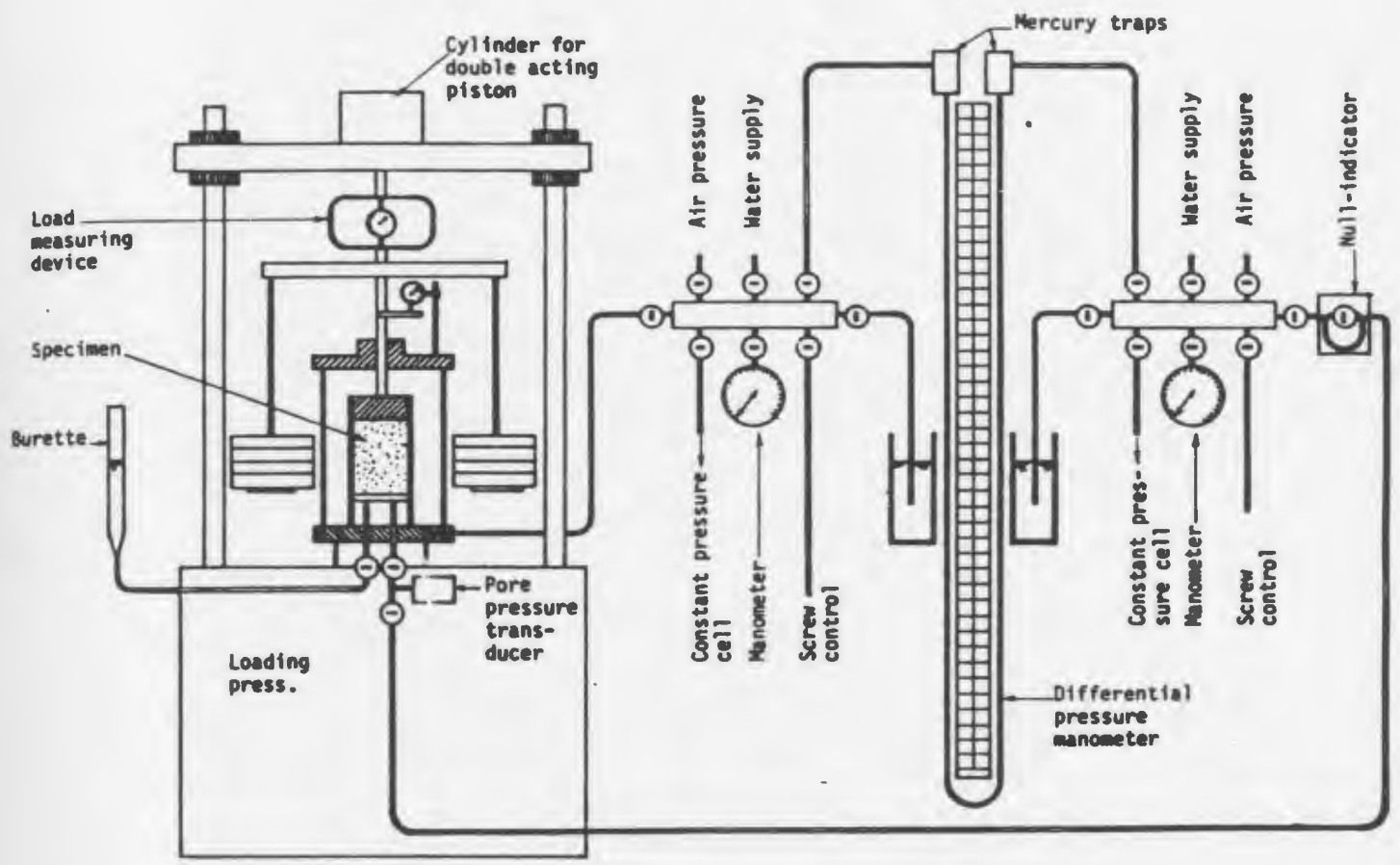


Figure 3.2: General Layout of a Triaxial Test Unit in NGI (After Berre, 1981).

- consolidate specimens (isotropically, K_0 , or with specified consolidation stress ratios, $K_c = \frac{\sigma_1}{\sigma_3}$, where σ_3 and σ_1 are confining pressure and axial pressure),
- shear specimens along specified stress paths in both compression and extension, either drained or undrained,
- perform cyclic loading,
- record data and use real-time data as feedback to control the test, and
- reduce data and produce report-quality graphics.

The most commonly performed cyclic tests are: (1) undrained cyclic loading tests, and (2) drained cyclic loading tests. Undrained cyclic tests are performed to record the deformation, pore pressure response and liquefaction potential of samples. Drained cyclic tests are performed to record the volume change of samples and to calculate cyclic modulus.

The cyclic triaxial experimental setup used in this study and the data acquisition systems implemented by the Centre for Cold Ocean Resources Engineering (C-CORE) at Memorial University will now be described in detail.

3.2 Experimental Setup

The main components of the cyclic triaxial systems are the triaxial cell, loading system, control panel, and external measuring systems (cell pressure and pore pressure transducers, volume change transducer, a Linear Variable Differential Transducer (LVDT), and a mechanical or electrical load cell). Assembly of the experimental setup is shown in Figure 3.3.

The triaxial testing setup was designed by C-CORE and manufactured in the university machine shop. It is similar to the one at the National Research Council in Ottawa. Some modifications were made by the author in order to achieve the objectives of this study.



Figure 3.3: Assembly of the Experimental Setup.

3.2.1 Triaxial Cell

A triaxial cell consists of four major components:

- a base, which forms a pedestal on which a specimen rests and incorporates various pressure connections,
- a removable cylinder and top plate, which encloses the specimen and enables fluid pressure to be applied,
- a load shaft, which applies the axial cyclic stress to the specimen, and
- an efficient connection between the specimen cap and the loading shaft, which will produce enough force (suction and friction) to support two-way loads, i.e., extension and compression forces resulting from cyclic loading. Beside the friction and suction type, the join between cap and loading shaft can be designed as magnetic type or mechanical type.

The triaxial cell used in this study has the following features:

- a cylindrical specimen of 35.6 mm in diameter and 80 mm long,
- capability of applying compression as well as extension loading,
- two ends drainage,
- cell pressure (confining pressure) is applied by compressed air and transmitted by water, the confining medium,
- the cell is designed to accept specimens of different sizes, where the base pedestal and specimen cap could be replaced correspondingly, and
- the cell cannot be used for static strength tests.

A picture of the triaxial cell and control panel is shown in Figure 3.4. The cylindrical acrylic chamber is 300 mm in outside diameter, 12.8 mm thick, and 450 mm long. O-rings were used for sealing the top plate and the base plate to the acrylic chamber.

The cell may be used for a maximum allowable internal pressure of 800 kPa. Three 6 mm diameter stainless steel rods and tightening screws were used to join the top plate (with the loading shaft), the acrylic chamber and a stainless steel sealing ring. The other three 9 mm diameter rods with 3 round handles were used to fasten the aforesaid chamber to the base plate.

3.2.2 Cyclic Loading System

Cyclic loads, both compression and extension, are applied to specimens with a Bellofram piston actuated by an air pressure regulator that is, in turn, powered by an electric-to-pneumatic transducer. This loading piston resulted from a long-term development program that included some very precise machining so that low-level loads could be applied consistently without excessive or variable friction. Another Bellofram is placed at the junction of the loading shaft and the top plate to allow the loading shaft to move freely. The design finally adopted is capable of many millions of load applications without significant wear or change in friction. With this system, it is possible to maintain a full-amplitude load pattern even when the specimen fails and exhibits drastic reduction in stiffness.

A function generator provides a variety of wave form loadings with different frequencies and amplitudes. A load cell is joined with the loading shaft to measure the actual load applied on the specimen. The loading system is shown in Figure 3.5.

An oil seal inlaid with a spring is embedded in a hole in the specimen cap. With the aid of the spring and the vacuum pressure forming inside the specimen cap, the oil seal can produce enough force to hold the loading shaft when it is moving away from the specimen.

3.2.3 Back Pressure Saturation and Pore Pressure Measurement Systems

The back pressure system is used to improve the degree of saturation of the specimens. The back pressure applied to specimens during saturation is provided by

Figure 3.4: Triaxial Cell and Control Panel.

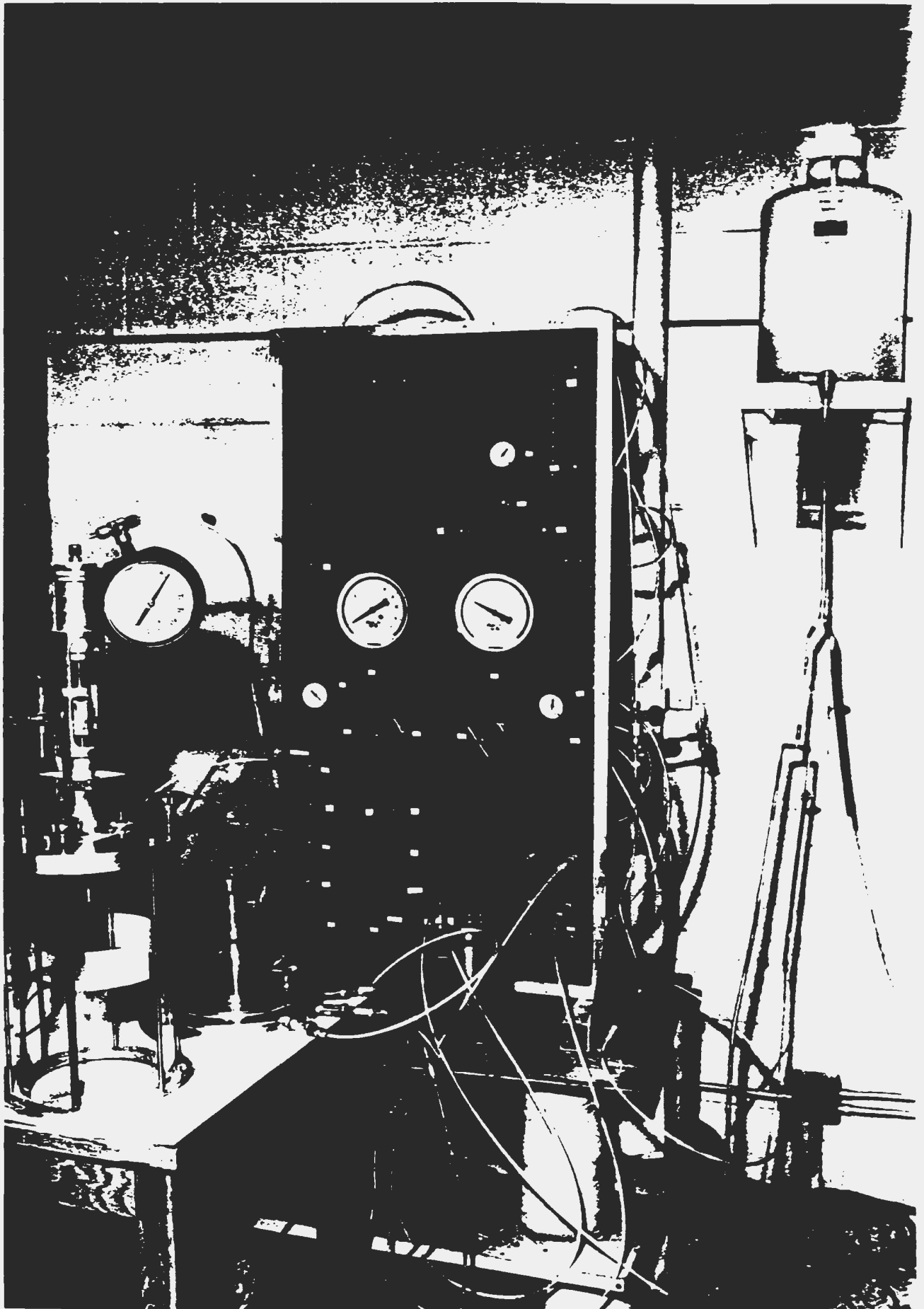
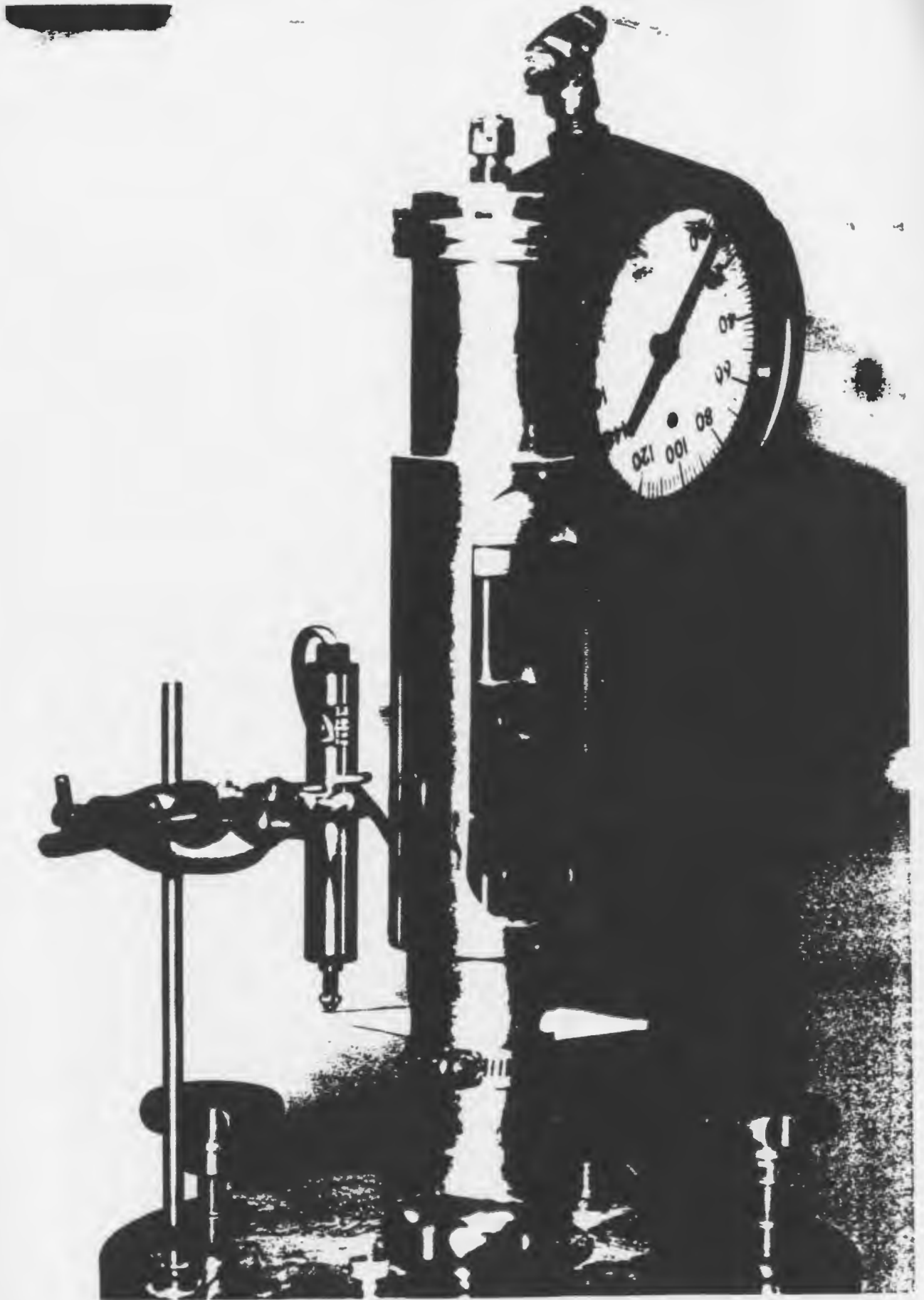


Figure 3.5: Loading System.



compressed air through a de-aired water reservoir (as shown in Figure 3.6). The pressure can be accurately maintained for any desired period of time using air pressure regulators that maintain the desired pressures regardless of minor fluctuations in the air pressure.

The pore pressure measurement systems make use of the same line as the back pressure system. A pore pressure transducer is connected to the line to allow accurate measurement of pore-water pressure. All of the connecting lines on the pressure control systems are made of 6.35 mm (1/4 in) diameter high pressure plastic tubing. The pressure control system is also connected to the volume change device described in the next section.

A quick connect system for line connections provides a great versatility in conducting tests and also avoids trapping air bubbles in the line.

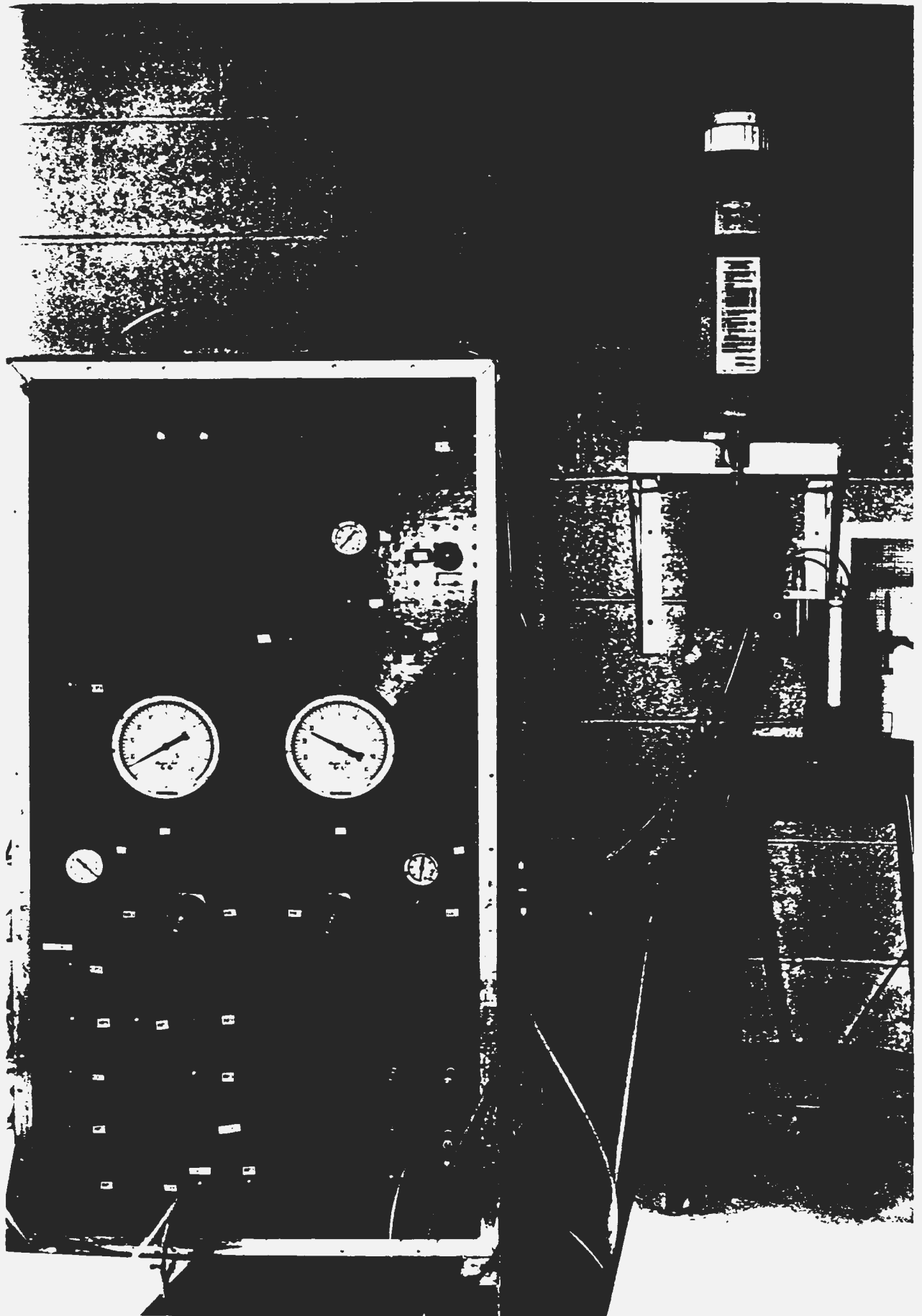
3.2.4 Volume Change Measurement Device

Automatic recording of displacements, loads and pressures in soil dynamics testing is now common, and transducers are readily available for such measurements. However, the recording of volume changes still presents difficulties because of very small change on specimen void volume during tests. In view of this fact, the volume change measurement device was bought commercially. The sensitivity of the device is 0.01 cc.

The device is shown schematically in Figure 3.7, and consists of a hollow brass cylinder contained by two diaphragms on the top and bottom, attached to a 'floating' frictionless piston. Water flowing into or out of the top chamber sealed by a Bellofram causes the piston to move and this movement is measured externally by means of a displacement transducer mounted on the outside of the cylinder.

The two quick connects are mounted on the control panel and provide connections for the volume change measurement device.

Figure 3.6: Back Pressure Saturation and the Pore Pressure Measurement Systems.



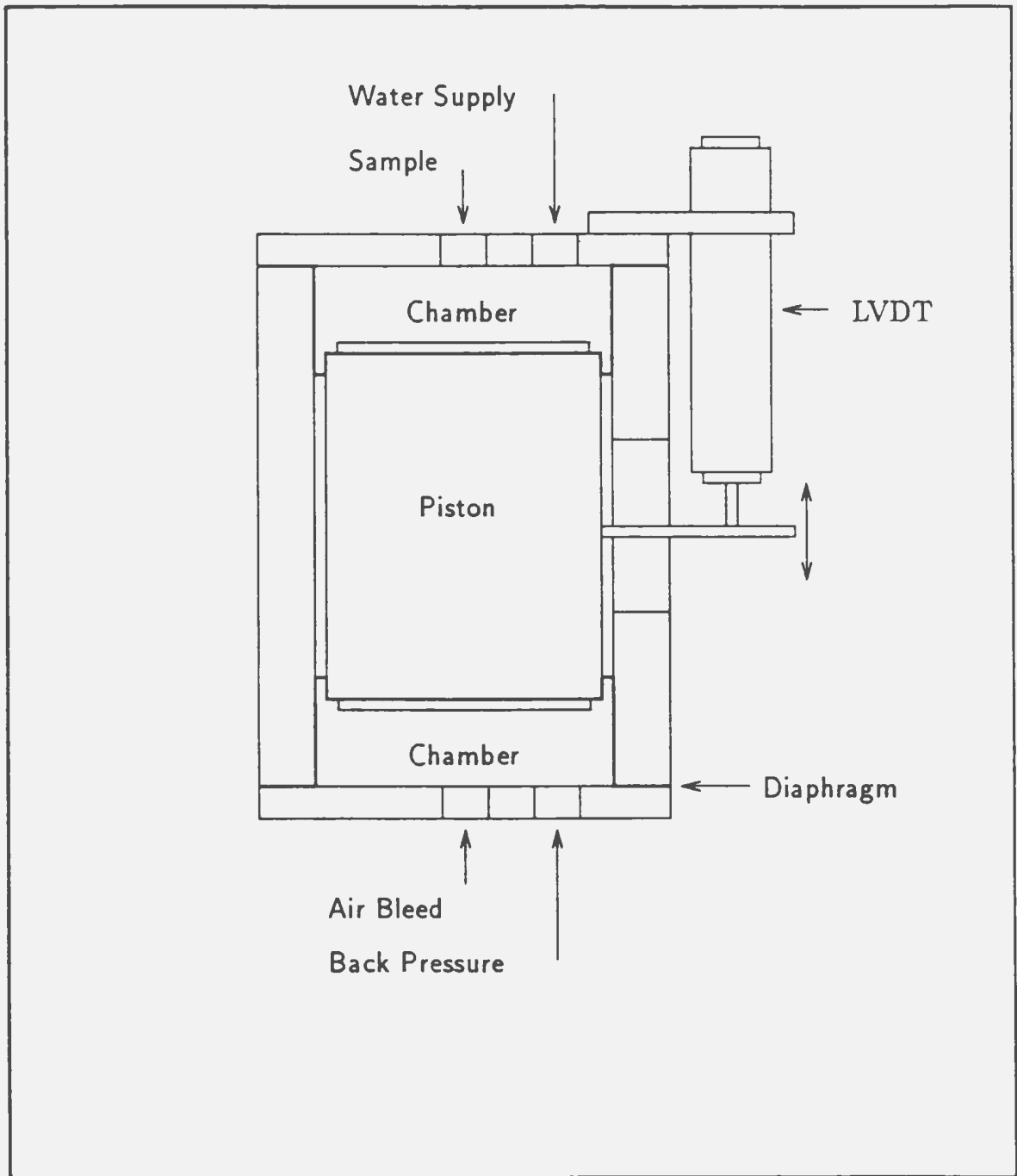


Figure 3.7: Volume Change Measurement Device.

3.2.5 Axial Deformation Measurement Setup

Axial deformation in the specimen during the test is measured by means of a LVDT mounted on a clamp. The clamp is held by a rigid steel rod which is extended from one of three rods between the top plate and the base. The probe of the LVDT rests on the LVDT holder which is attached to the loading shaft. Such a device is shown in Figure 3.5.

3.3 Data Acquisition and Control System

3.3.1 Data Acquisition and Control System

The data acquisition and control system used in this study is Keithley's Model 575-2 as shown in Figure 3.8. This system is a high speed, high resolution data acquisition system for analogue input and output, digital I/O, and power control. The system is ideal for small-scale measurement and control tasks requiring high performance and expansion capability.

This system has the following features:

- high-performance instrumentation support for testing,
- 16-bit (50,000 rdg/sec) A/D for high-speed and sensitive measurements,
- fully software programmable,
- true hardware trigger circuit for external analogue, or digital control of analogue input,
- expansion slot for specialized signal conditioning or I/O modules,
- directly powered from PC, or from optional AC wall transformer or automotive adapter,
- interface for IBM PC/XT/AT/386, PSY2 25 & 30 and compatibles, and KDAC500/I software for interpreted BASIC, C, or other Microsoft and Borland languages.



Figure 3.8: Data Acquisition and Control System.

3.3.2 Software Used

The data acquisition system was driven by a software interface. The program which was used for recording the signals from sensors, such as pressure transducers, LVDT, load cell, etc. is called S575 and was provided by the Fluid Lab of the Faculty of Engineering and Applied Science. This program is written in C, and has the following capacities:

- to conduct basic data acquisition,
- to calibrate all channels,
- to zero any number of channels, then complete data acquisition task,
- to trigger a channel, starting the data acquisition when a predefined threshold is met,
- to save data in binary format (ASCII is default),
- to produce a signal used to drive a wave spectrum while data from input channels are simultaneously recorded, and
- to display line graphs of each channel's results.

In order to review the graphs of a file saved on a disk, another program called PLTKLY was used to display the graphs. Other programs such as SPECGEN and MATLAB on the Computer Aided Design Centre's network were used for data reduction.

The flow chart of the data acquisition and processing routines is shown in Figure 3.9.

3.3.3 Signal Conditioning

The experimental setup was installed in the soils laboratory at the Faculty of Engineering and Applied Science. At this site, noise can be a problem. Hence, DC

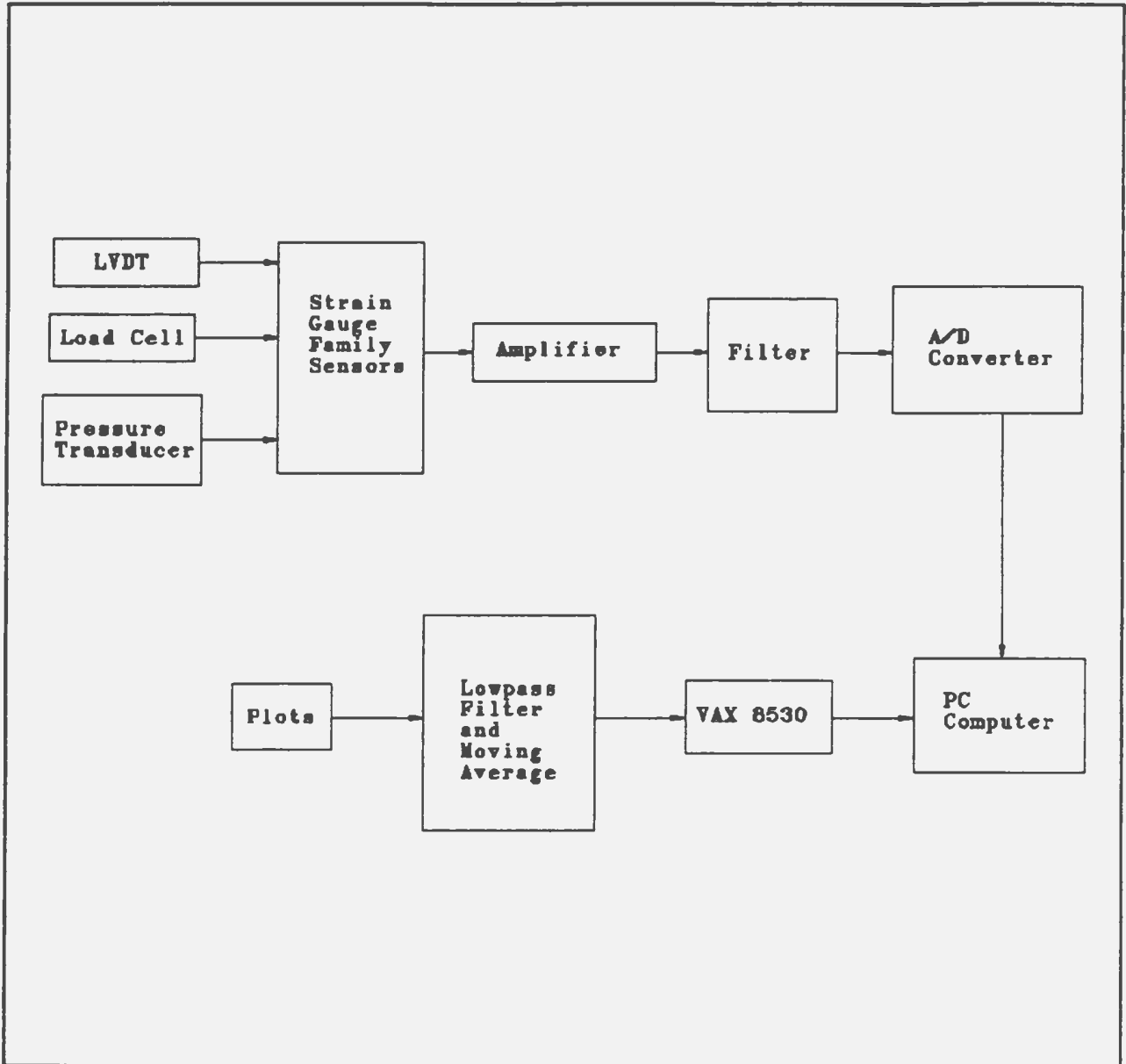


Figure 3.9: Flow Chart for the Data Acquisition and Processing Routine.

bridge amplifiers were used to increase the signal-to-noise ratio. Furthermore, filtering was desired. A single-pole input filter was designed and placed in the incoming signal line for any analogue input (see Figure 3.10).

The relative RC (Resistance and Capacitance) values will depend on a variety of factors, including the frequency of noise, required attenuation, and necessary response time. The RC values can be computed from the following formula:

$$f_{(3db)} = \frac{1}{2\pi RC} \quad (3.1)$$

where f is the frequency in Hz, C is the capacitance in Farads, and R is the resistance in Ohms.

Note that there are hundreds of RC values that can be used in a given application. To minimize the effects of the series resistance, however, it is recommended that the value of R be kept as low as possible. In the designed filter, R and C were chosen as 100Ω and $800\mu\text{F}$ respectively in order to cut off frequencies higher than 2 Hz.

3.4 Calibration Procedures

Every sensor used in the triaxial system needs to be individually calibrated. The calibration is carried out before testing by a PC-based software called S575/C. This program can be used for the calibration of linear variable transducers. The sampled-data feedback from the system forms a calibration line. The program saves offset and slope values to an initialization file for each sensor after collecting the data on predetermined sampling points. The program may calibrate all channels at one time.

3.4.1 Calibration of Pressure Transducers

Pressure transducers including cell pressure transducer and pore pressure transducer are calibrated by a parallel calibration gauge. The load is applied in steps. The calibration program takes the reading on each step.

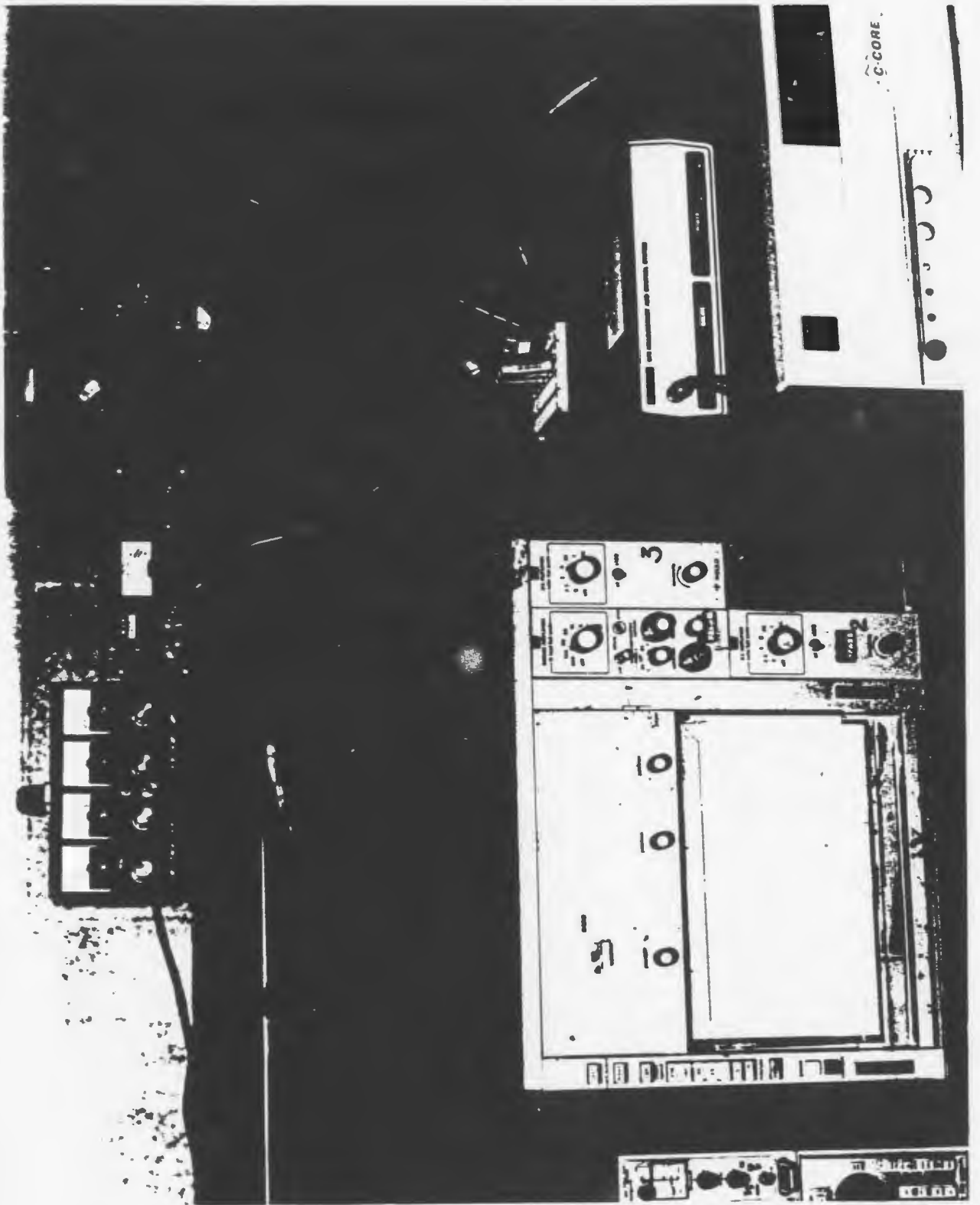


Figure 3.10: Signal Conditioning.

3.4.2 Calibration of LVDT

LVDT for axial deformation is calibrated by a LVDT calibrator. The full scale range of the LVDT is 30 mm.

3.4.3 Calibration of Volume Change Transducer

This calibration can be carried out easily using the arrangement shown in the diagram (see Figure 3.11). Before commencing calibration, the back pressure should be increased to the maximum operating value, and the volume change device operated over its full range a few times to ensure that the Bellofram seals are properly seated. If very precise calibration is required, it is necessary to use a small burette. A pump is used to empty or recharge the burette.

3.4.4 Calibration of Load Cell

The load cell can be accurately calibrated on a jack, and loaded in steps. The full scale range of the load cell is 680.4 kg (1500 lbs).

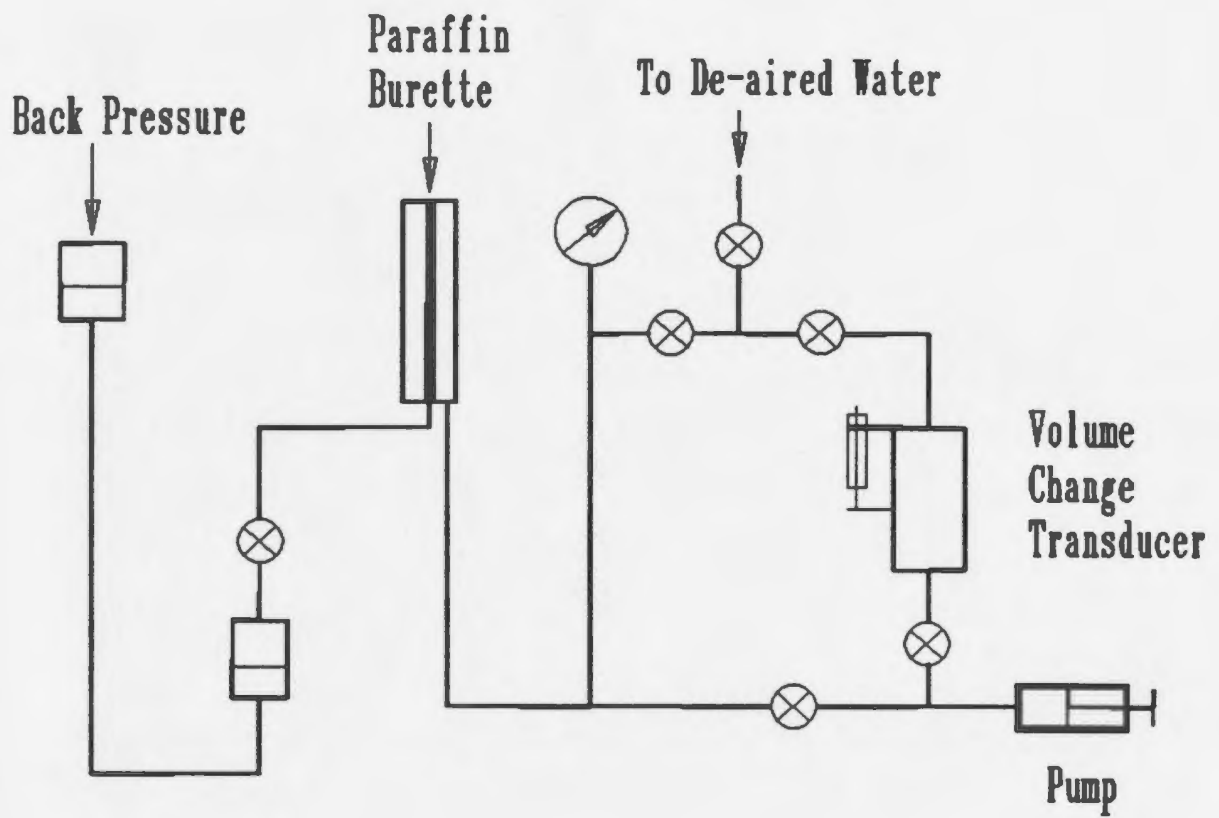


Figure 3.11: Diagram for Calibration of Volume Change Transducer.

Chapter 4

Identification and Preparation of Investigated Soils and Test Procedures

4.1 Types of Soils Tested

4.1.1 Sands

The Nerlerk sands used in this investigation were obtained by Gulf Canada Resources Ltd. (GCR) during the summer of 1988. The samples were obtained near the northeast crest of the Nerlerk Berm, a subsea berm designed to form part of an offshore, bottom-founded, hydrocarbon exploration platform at Nerlerk in the Canadian Beaufort Sea. Five liquefaction slides occurred during the construction of this hydraulically placed berm in 1983 (Sladen et al., 1985). Although limited information was available on the samples, the construction materials were probably obtained from the Nerlerk borrow pit.

A small sample of the Nerlerk sands was subjected to detailed analysis of mineralogy by Gulf's Geological Services Laboratory. The sand grains are predominantly quartz (84%) with some Feldspar Plagioclase (13%) and minor amounts of Dolomite and Calcite. The grains are sub-angular to sub-rounded and have an appearance similar to Erksak sand (Golder Associates, 1989).

Table 4.1 shows the physical properties of the Nerlerk sands from the different areas of the berm.

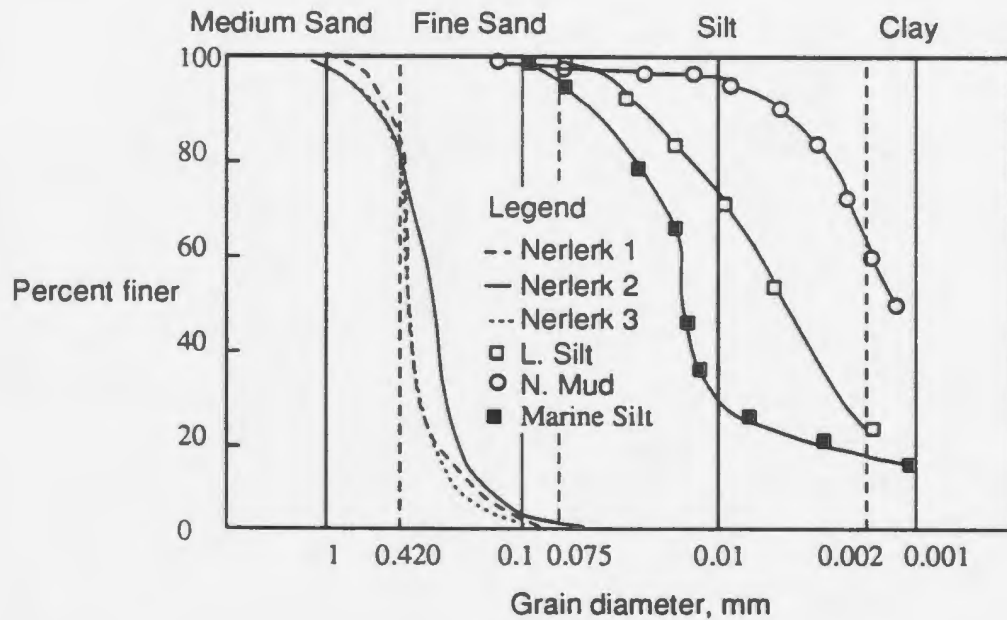


Figure 4.1: Grain Size Curves for Sands, Silts and Nerlerk Mud Tested.

Nerlerk #1 Sand (Nerlerk #1)

Nerlerk #1 was a light brown uniform medium sand with particles of sub-round shape. Sieve analysis was carried out according to ASTM D422 and the results are shown in Figure 4.1. C_U and C_C were 2 and 1.194 respectively. According to the Unified Soil Classification (USC) system, Nerlerk #1 is a poorly graded medium sand with little fines. The maximum and minimum unit weight γ_{max} and γ_{min} were 17.50 and 14.90 kN/m^3 .

Nerlerk #2 Sand (Nerlerk #2)

Nerlerk #2 was a medium brown, uniform sand. The grain size analysis curve is shown in figure 4.1. C_U and C_C were 2.22 and 1.42 respectively. According to the USC system, this material is a poorly graded sand with some fines. γ_{max} and γ_{min} were 17.50 and 14.20 kN/m^3 .

Nerlerk Sand #3 (Nerlerk #3)

This material was a dark brown uniform medium sand. The grain size analysis curve is shown in Figure 4.1. C_U and C_C were 1.82 and 1.06 respectively. According to the USC system, this material is a poorly graded sand with little fines. γ_{max} and γ_{min} were 16.90 and 13.90 kN/m^3 .

From the classification test results given above, it can be observed that the grading curves and gradation indices are similar for all three Nerlerk sands. Testing will determine if they also have similar liquefaction characteristics.

4.1.2 Silts

Lundrigan Silt

The Lundrigan Silt used in the study was obtained from a settling pond at a rock crushing plant in St. John's, Newfoundland. This soil had been air dried prior to the current testing program. Atterberg limits, grain size analysis, oedometer, direct shear box and CIU triaxial tests were carried out for classification and future studies.

The soil was found to have a low Plasticity Index, with a Liquid Limit (ω_L) of 31%, Plastic Limit (ω_P) 27%, and Plasticity Index (I_P) of 4. The soil is classified as ML, inorganic silt (see Figure 4.2).

A hydrometer analysis was conducted to determine the particle size distribution. The soil grain size analysis curve is presented in Figure 4.1. The uniformity coefficient, C_U , and coefficient of curvature, C_C , were found to be 10 and 1.8 respectively. According to the USC, this material is a well-graded silt with 21% clay (see Figure 4.1).

Oedometer tests were carried out on the silt in order to obtain the compression index, expansion index and creep indices required in Chapter 5. The water content $\omega = 38\%$ and $\gamma_{sat} = 20kN/m^3$ were used. The same water content and same saturated unit weight will be used in the long term cyclic deformation tests in

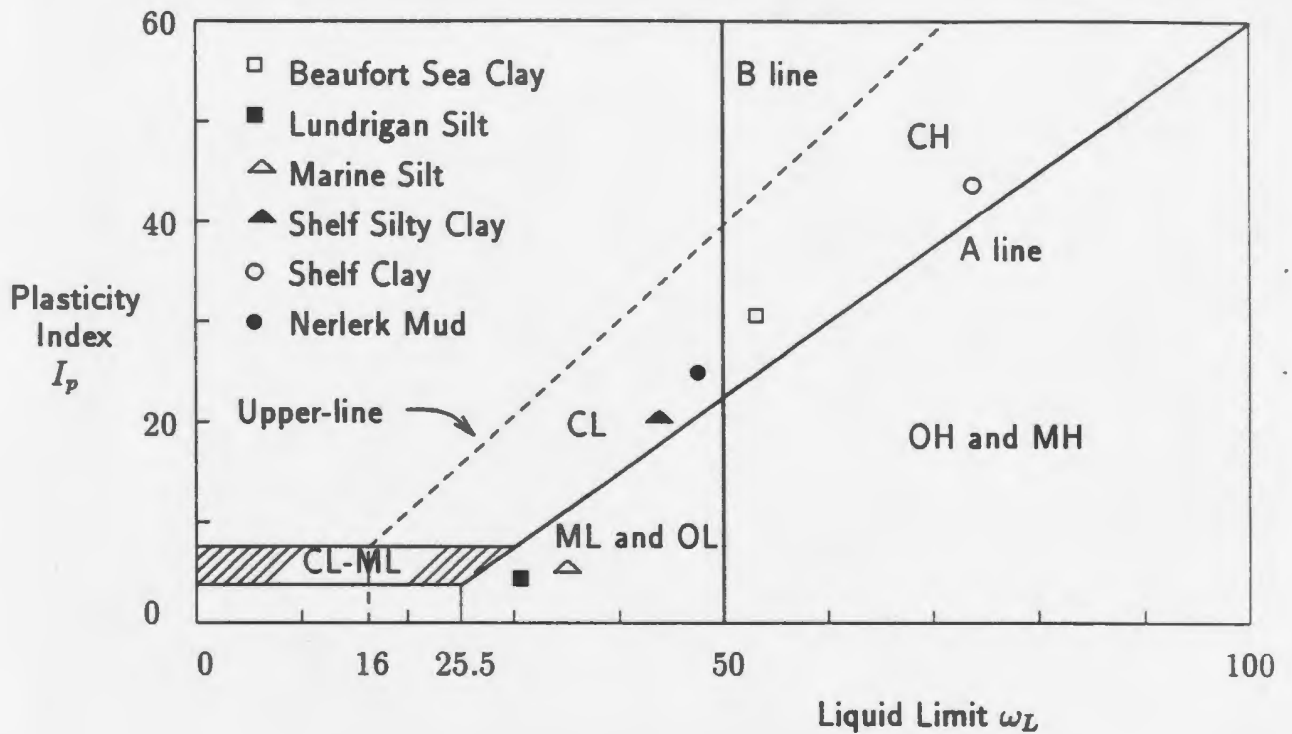


Figure 4.2: Plasticity Chart.

Chapter 5. The consolidation curve is shown in Figure 4.3. The major parameters determined from the curve are:

Compression index: $C_c=0.124$,

Expansion index: $C_s=0.012$, and

Coefficient of consolidation when the vertical stress is 100kPa: $c_v=8.4 \cdot 10^{-7} \text{ m}^2/\text{s}$.

Because the soil was air dried and the samples used in the tests were remoulded, the consolidation parameters obtained from the oedometer test were only an estimation. However, since the same test conditions were chosen in the other oedometer tests here and in the long term cyclic deformation tests in Chapter 5, the creep indices obtained from the oedometer tests were of significance (see Section 5.5 for details).

The results of CIU triaxial tests are summarized below:

Angle of internal friction: $\phi' = 29.5^\circ$ and

Cohesion intercept: $c' \approx 0$.

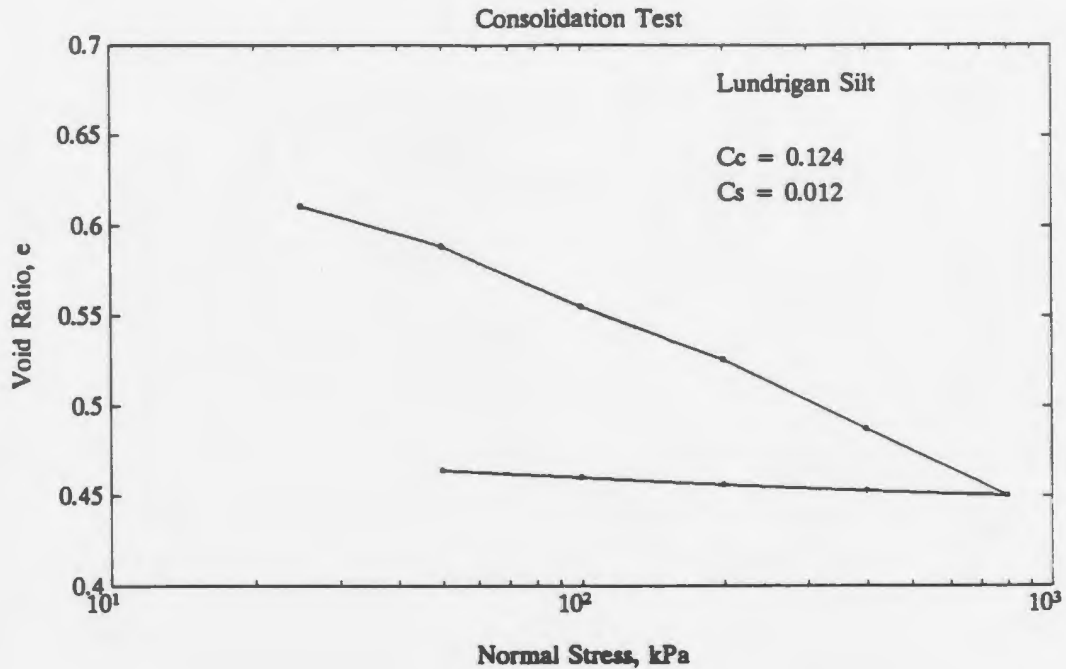


Figure 4.3: Oedometer Curve of Lundrigan Silt.

Direct shear box tests were also carried out on the material. The results obtained from the shear box tests differed considerably from the triaxial tests, owing partially to the different stress paths, difficulties encountered in mounting of the samples and maintaining the gap between the halves of the shear box during testing. The results are summarized below:

Cohesion intercept: $c' = 2\text{kPa}$ and

Angle of internal friction: $\phi' = 36^\circ$.

A standard compaction test (Proctor tests) was performed on the Lundrigan Silt in order to obtain the moisture-unit weight relationship for a given compaction energy. The compaction rammer used in the tests was a 24.5 N rammer which was dropped 0.305 m. Approximately 3 kg of soil was compacted each time into a 944 cm^3 mold in three layers with 25 blows per layer. The compaction curve is shown in Figure 4.4. The optimum water content obtained from Figure 4.4 is approximately 17.3%.

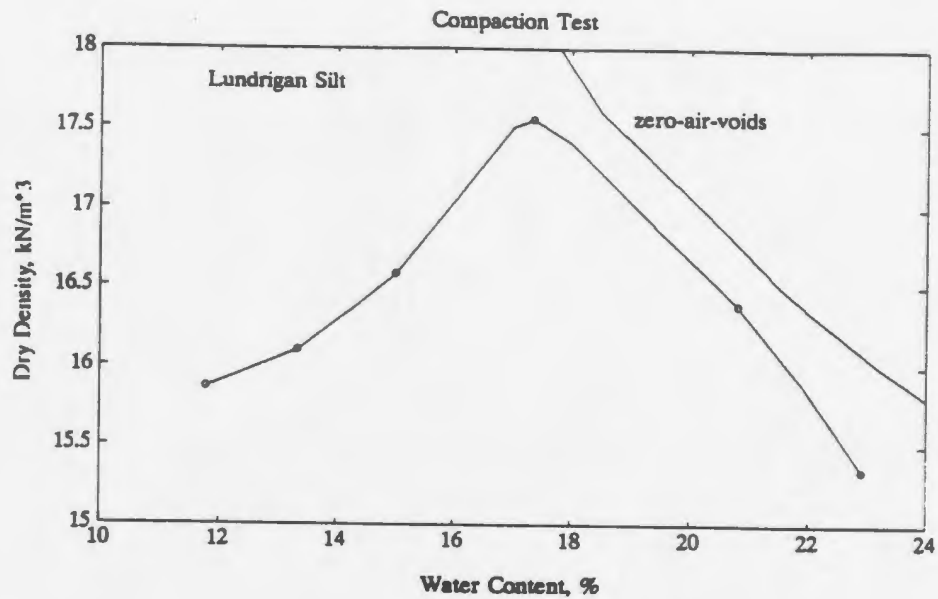


Figure 4.4: Compaction Curve.

The main physical indices are summarized in Table 4.2.

Marine Silt

In the summer of 1990, the Geological Survey of Canada (GSC) conducted a field program to investigate the geology and geotechnical conditions of the Beaufort Sea Shelf and coastal areas in the vicinity of northern Richards Island to the east of the Mackenzie Delta. The location of the site was bounded by latitude $N69^{\circ}39'$ to $N69^{\circ}52'$ and longitude $W134^{\circ}03'$ to $W134^{\circ}29'$, and is shown in Figure 4.5. This material has been termed Unit B silt by the GSC and is described as follows (GSC, 1990):

Borehole 90BH03 – Unit B – silt – located at a depth of 1~14m-dark grey, with sand interbedded, moderate bioturbation, some graded beds.

The samples were intact and obtained from various depths. A considerable effort was made to maintain the in-situ environment so the seafloor specimens were

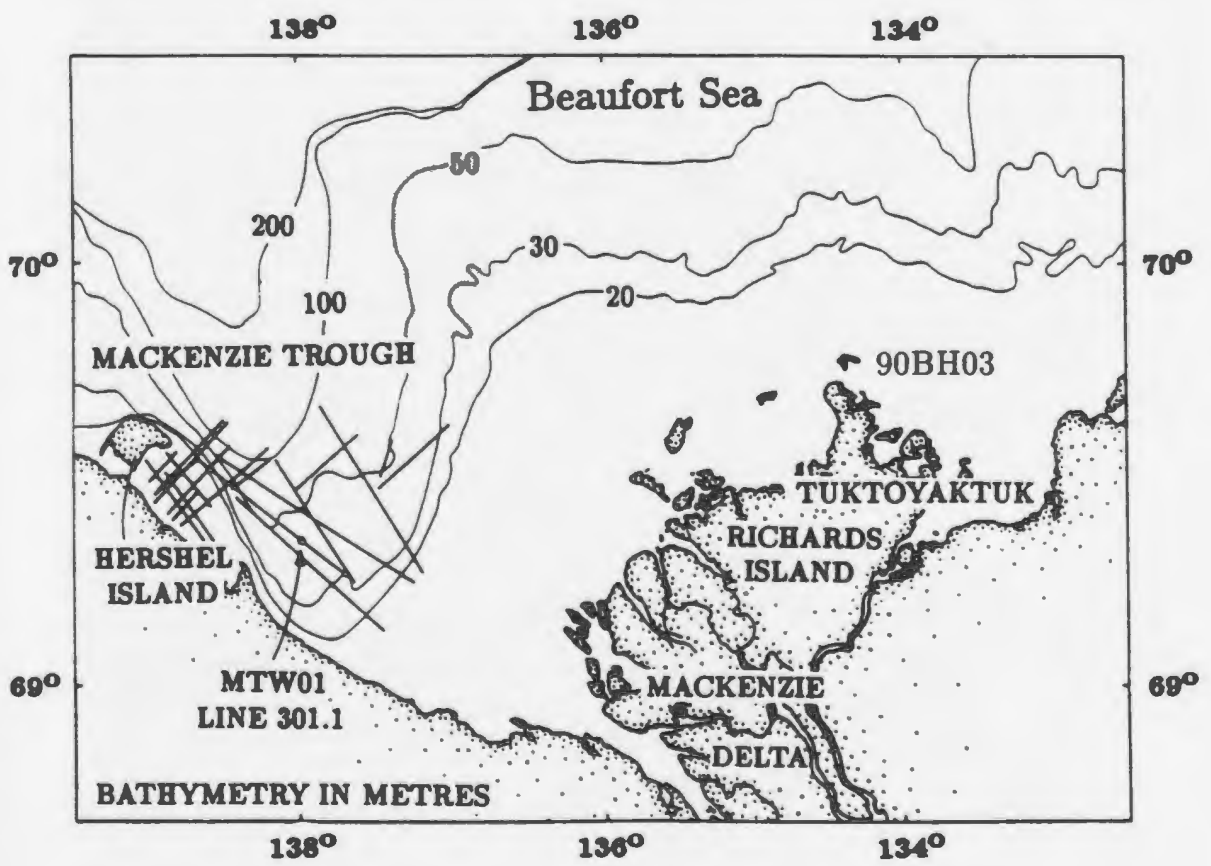


Figure 4.5: Location for Marine Silt and Beaufort Sea Clay (After Moran et al., 1989).

stored in a humidity controlled room until tested.

The major physical properties are described in Table 4.2. A hydrometer analysis was carried out to determine the grain size distribution shown in Figure 4.1. C_U and C_C were 21 and 3.86 respectively. According to the USC system, this material is a medium well-graded silt with 17% clay. According to the Plasticity Chart shown in Figure 4.2, the soil is classified as ML, inorganic silt.

The natural water content of this marine silt was determined to range from 26 to 31%.

4.1.3 Clays

Beaufort Sea Shelf Silty Clay (Shelf Silty Clay)

Shelf Silty Clay was obtained from the same area as the Marine Silt described in the last section. This material has been described as follows (GSC, 1990):

Borehole 90BH02 – Unit B – Silty Clay – located at a depth of 4~5m-grey to black, moderately to extensively bioturbated.

The natural water content was found to range from 32 to 39%. The liquid limit, ω_L , is approximately 44%, the plastic limit, ω_P , is approximately 22%, and the plasticity index, I_P , is 22. From Figure 4.2, this soil is classified as CL, inorganic silty clay of medium plasticity.

According to the GSC Report (GSC, 1990), the preconsolidation pressure, σ'_p , of this soil was approximately 220 kPa. All specimens exhibited high levels of overconsolidation with an OCR of approximately 1.4~2.6.

The classification tests results are summarized in Table 4.3.

Beaufort Sea Shelf Clay (Shelf Clay)

Like the Shelf Silty Clay, Shelf Clay was obtained from the Beaufort Sea Shelf. This material is described as follows:

Borehole 90BH02 – Unit B – clay – located at a depth of 14~15m-grey to black, with high plasticity.

The natural water content of this soil was determined to be 47 to 58%, $\omega_L=73\%$,

and $\omega_P=30\%$. According to the USC system, this soil is classified as CH, inorganic clay of high plasticity (see Figure 4.2).

According to the GSC Report (GSC, 1990), the preconsolidation pressure, σ'_p , for this soil was approximately 250 kPa. The OCR for this soil is approximately 1.6~2.0. The physical indices are shown in Table 4.3.

Nerlerk Mud

The Nerlerk Mud tested in this program was obtained from two boreholes, NEB6788 S25 and S28, under the Nerlerk Berm. The samples were obtained by Shelby tube but were slightly disturbed due to long-distance transport and the long duration of storage. Three specimens were treated as undisturbed samples from the 40cm long sampling tube after the two ends of the samples were cut off.

Figure 4.1 shows the grain size distribution curve for the Nerlerk Mud. Clay size particles constitute 59% of the material, with the remainder being silt size particles or fine sand. The fines fraction is mainly quartz but the clay contained in the fines is mainly Illite (85%), with some Chlorite (9%) and Kaolite (6%) (Golder Associates, 1989). The samples consisted of a very soft to firm, dark grey silty clay, of medium plasticity, with some organics and occasional sand lenses. The ω_L is 47%, ω_P is 22%, and I_P is 25. According to the USC system, the soil is classified as CL, inorganic silty clay with medium plasticity (see Figure 4.2).

An oedometer test was also performed on the Nerlerk Mud by Golder Associates (1989). The in-situ vertical pressure was approximately 41kPa as shown in Figure 4.6. The physical properties (Golder Associates (1989) for the Nerlerk Mud are summarized in Table 4.3, where ω_n is the natural water content.

Beaufort Sea Clay

The Beaufort Sea Clay, provided by the Atlantic Geoscience Center, was obtained from the Mackenzie Trough in the Canadian Beaufort Sea, with thin-walled steel tubes, 3.7 cm in diameter, and extruded in the laboratory. The location of the Mackenzie Trough is shown in Figure 4.5. The laboratory shear strength is

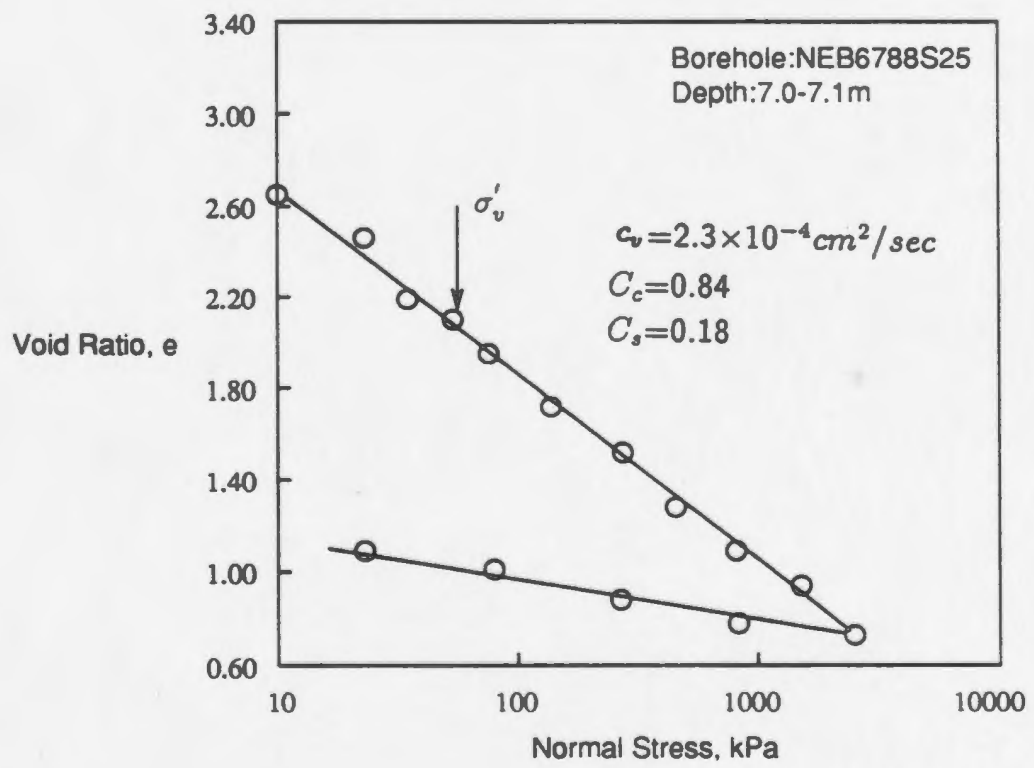


Figure 4.6: Oedometer Curve for Nerlerk Mud (After Golder Associates, 1989).

approximately 4-20 kPa (Moran et al., 1989).

The physical properties of the Beaufort Sea Clay are summarized in Table 4.3. According to the USC system, Beaufort Sea Clay is classified as CH, inorganic clay of high plasticity (see Plasticity Chart Figure 4.2).

Table 4.1: Physical Properties of Nerlerk Sand.

Type of Soil	G_s	C_u	C_c	γ_{min} kN/m^3	γ_{max} kN/m^3
Nerlerk #1 Sand	2.65	2.0	1.194	14.90	17.50
Nerlerk #2 Sand	2.67	2.22	1.42	14.20	17.50
Nerlerk #3 Sand	2.67	1.82	1.06	13.90	16.90

Table 4.2: Physical Properties of Silts.

Type of Soil	Borehole	Depth m	ω_l %	ω_p %	I_p	Gradation	ω_n %	Sensitivity
Marine Silt	90BH03	5.98~6.40 14.40~14.66	35	29	6	medium well graded	26~31	1.4
Lundrigan Silt	—	—	31	27	4	well graded	—	—

Table 4.3: Physical Properties of Clay.

Type of Soil	Borehole	Depth m	w_l %	w_p %	I_p	c_c	w_n %	Sensitivity
Shelf Silty Clay	90BH02	5.35~5.52 9.81~9.86	44	22	22	2.70	32~39	2.8
Shelf Clay	90BH02	14.21~14.36	73	30	43	2.72	47~58	3.3
Nerlerk Mud	NEBG788S28	0.0~0.83	47	22	25	2.71	62~71	4.6
Beaufort Sea Clay	MTW01 ARK84	12.31~23.43	53	23	30	2.70	51.4~59.8	3.1

4.2 Sample Preparation Methods

4.2.1 Remoulded Nerlerk Sands

The sands were oven dried before testing. Particles with a diameter of grains greater than No.10 U.S. (2mm) sieve (approximate 8%) were removed. Data on natural void ratios were not available. Therefore, a procedure was developed to prepare sand specimens. Several methods of pouring sand into the mold were tested to determine which method could provide a sample close to medium density, i.e. dry unit weight, γ_d , when relative density $D_r = 50\%$ ($\gamma_d = \frac{G_s}{1+e_{(D_r=50\%)}}$ and $e_{(D_r=50\%)} = e_{max} - (e_{max} - e_{min}) * 50\%$, where e_{min} was obtained by vibrating the mold and e_{max} was obtained by pluviating the sands into the mold). The method adopted was to pluviate the sand through a funnel and then tap the mold wall until medium density was achieved. For dense sand samples, a small shaking table was used to achieve a relative density of $D_r = 75\%$ in the mold. The cyclic stress ratio (CSR) to cause liquefaction is linearly proportional to relative density to approximately $D_r = 70\%$ (Mulilis, 1975). The linear relationship to calculate CSR up to 70% relative density knowing CSR at $D_r = 50\%$ is

$$\frac{\sigma_d}{2\sigma_3}(D_r) = \frac{\sigma_d}{2\sigma_3} \times \frac{D_r}{50\%}. \quad (4.1)$$

In order to compare the results obtained from different relative densities, the CSR can be normalized to the CSR measured when $D_r=50\%$ using the above equation.

4.2.2 Remoulded Lundrigan Silt

All samples tested using Lundrigan Silt were of remoulded soil because the silt was previously air dried. The size of the chosen mold was the same as the final size of the sample to be tested. Remoulded soil was placed in the triaxial mold in layers and compacted to a selected unit weight (i.e., $\gamma = 20kN/m^3$ when saturated at a water content of $\omega=38\%$ as discussed in Section 4.1.2). The mold was then

unclamped and the sample was mounted in the triaxial cell. Care was taken to achieve the same density for each type of the remoulded samples.

4.2.3 Intact Marine Silt, Shelf Silty Clay, Shelf Clay, Beaufort Sea Clay and Slightly Disturbed Nerlerk Mud

After removing the wax around the samples, the soils were extracted from the plastic tubes and trimmed to a diameter of 36mm. The length of the specimens was 80mm. The trimmed specimens were weighed and the initial volume was recorded from which the unit weight was calculated.

A special mold was designed to enclose the trimmed specimens with triaxial membranes. The size of the mold was a little greater than the final size of the specimen and a membrane was mounted on the mold wall. A vacuum pump was used to create a vacuum between the membrane and mold wall. The specimen could then be put into the membrane easily.

The slightly disturbed Nerlerk Mud samples were used as "undisturbed samples" as discussed previously in Section 4.1.3.

4.3 Back Pressure Saturation

The back pressure saturation was applied to all silt and clay specimens.

Lee and Black (1972) provide theoretical and experimental data for time and magnitude of back pressure required to dissolve air bubbles in specimens.

The base of the triaxial cell was initially de-aired by flushing with de-aired distilled water. Filter paper discs were then placed over the porous stones to prevent them from becoming clogged with clay particles. 2 to 3 mm of de-aired distilled water was left covering the base filter plate during mounting. As the specimen was mounted on the base, this layer of water was displaced preventing air from entering the filter. The procedure adopted for back pressure saturation is to incrementally increase the cell pressure and pore pressure simultaneously, allowing equalization at each increment. After equalization, the value of a pore-water pressure parameter,

$B = \frac{\Delta u}{\sigma_3}$ (Skempton, 1954), was measured by applying the next increment. Several variables are involved in this procedure:

- the magnitude and duration of back pressure increment,
- the magnitude of the effective consolidation pressure during the saturation which may or may not permit the specimen to swell,
- the magnitude of the cell pressure increase when checking the B-parameter, and
- the magnitude of back pressure applied which should not pre-stress the specimen, i.e. the effective confining pressure should not be greater than that under which the specimen is to be sheared.

Three other methods, which were not used in this study, can be applied to saturate the samples and to remove air bubbles from the samples:

- circulation of water through the sample under a slight hydraulic gradient,
- partial vacuum applied after the circulation of water to the sample in order to make sure that there are no air bubbles left in the circuit, and
- circulation of CO_2 through the sample to dissolve air bubbles.

Finally, a back pressure is applied to dissolve any gas remaining in the sample. A back pressure of 200kPa was found to be sufficient to produce a B-parameter greater than 0.9, indicating that all the gas was dissolved in the pore water of the soils.

4.4 Consolidation

In this study, all soil samples were isotropically consolidated. The consolidation pressure was applied by means of an actuator connected to a compressed air supply. The required confining pressure was obtained via an air-water cylinder. The

drainage connections were then opened to allow the sample to consolidate (two-way). The amount of water expelled was measured using a volume change apparatus. The B-parameter was measured for each sample before consolidation pressure was applied. No difficulty was found in obtaining $B=0.95$ within one hour back pressure saturation for sands and $B=0.9$ within 5 to 6 hours for the rest of the samples. For the NC samples, however, the compressed air system could not supply a sufficiently high pressure to allow a back pressure to be applied while still providing the required effective stress. B values were therefore somewhat lower than those observed for the OC specimens. B values for the clays after consolidation were found slightly higher than their initial values before consolidation (after back pressure saturation). A sample was discarded if its B value was found to be less than 0.9.

4.5 Rates of Loading

Frequencies of 1 - 2 Hz are typically of interest for earthquake loading and liquefaction problems (Konrad, 1985), and therefore a frequency of 1 Hz was used in liquefaction potential and stability threshold analysis during this study.

Frequencies of 0.01 - 0.1 Hz are of interest when considering introgravity and gravity wave loading. Therefore frequencies of 0.1 and 0.01 Hz were chosen to correspond to a gravity wave and an introgravity wave respectively. The long term deformation characteristics of the marine soils were tested at these frequencies.

4.6 Cyclic Wave Forms

A function generator was used to supply sinusoidal and rectangular (square) wave loadings which were considered to simulate waves and storms. The amplitude of loading was varied by simply adjusting the amplitude of the command signal.

Chapter 5

Deformation Characteristics and Predictions Under Long Term Cyclic Loading

Dynamic loading in a marine environment can induce deformation in soils around or beneath offshore structures. Storm wave loading is of great importance, either directly by causing pressure fluctuations in sub-bottom sediments, or indirectly by impacting structures and causing cyclic loading of the soil beneath the structure. Offshore geotechnical design requires that possible permanent deformations produced by wave loading of prescribed intensity and duration be evaluated. Therefore, there is a need to develop more general constitutive relations in marine geotechnical engineering.

This chapter presents a theoretical method which uses rheological mechanics to evaluate the time-dependent deformation of soil subjected to long term cyclic loading. This method takes into consideration the rheological quality of cohesive soils. Various models such as the Maxwell Model, the Kelvin-Voigt Model, etc. were adopted to simulate the viscous characteristics of cohesive soils. The numerical results from these models under a rectangular wave cyclic load were evaluated.

Cyclic triaxial testing was conducted to investigate the validity of these rheological models. The results of theoretical analysis were compared with those from the cyclic triaxial testing to ascertain the accuracy of the models for the evaluation of permanent deformation (i.e., long term deformation). The materials tested were

Lundrigan Silt and Beaufort Sea Clay. The tests were performed using a rectangular (or square) wave cyclic loading under conditions similar to an ocean environment.

5.1 Theoretical Derivations

An important characteristic of cohesive soils is viscosity. In order to account for its effects, a method based on rheological mechanics can be used to derive expressions for layer deformation caused by long term cyclic loading.

An ocean gravity wave can be described approximately as a rectangular wave form without introducing significant error. The loading function for a rectangular wave can be written in the following form:

$$\sigma = \sigma_d [I(t) - I(t - T) + \dots] \quad (5.1)$$

$$= \sigma_d \sum_{k=0}^N [I(t - 2kT) - I(t - 2kT - T)] \quad (5.2)$$

where

$I(t)$ is the Heaviside step function, $I(t) = 0$, when $t < 0$; $I(t) = 1$, when $t \geq 0$,

t is the overall time coordinate,

T is the semi-period of cyclic loading,

N is the number of cycles, $N = 0, 1, 2, \dots$,

σ_d is the amplitude of repeated load, and

k is an integer, $k = 0, 1, 2, \dots$.

The expression for soil layer strain $\epsilon(\bar{t})$ due to rheological mechanics can be derived as (see Appendix A):

$$\begin{aligned} \epsilon(\bar{t}) &= \sigma * J(t) \\ &= \sigma_d \sum_{k=0}^{N-1} [J(t - 2kT) - J(t - 2kT - T)] + \\ &\quad \sigma_d * [J(\bar{t}) - J(\bar{t} - T)I(\bar{t} - T)] \end{aligned} \quad (5.3)$$

i.e.,

for the loading period

$$\epsilon(\bar{t}) = \sigma_d \sum_{k=0}^{N-1} [J(t - 2kT) - J(t - 2kT - T)] + \sigma_d * [J(\bar{t})],$$

for the unloading period

$$\begin{aligned} \epsilon(\bar{t}) = & \sigma_d \sum_{k=0}^{N-1} [J(t - 2kT) - J(t - 2kT - T)] + \\ & \sigma_d * [J(\bar{t}) - J(\bar{t} - T)] \end{aligned} \quad (5.4)$$

where

\bar{t} is the local time coordinate within one cycle, $\bar{t} = t - 2NT$, $0 < \bar{t} < 2T$, and

$J(t)$ is a creep function, as defined in rheological theory. It is a deformation caused by a unit force which varies with time. The test for determining $J(t)$ is given in a following section.

In the early development of rheological theory, materials were primarily modeled by networks made up of simple elastic and viscous elements (Ferry, 1980). The elastic element is a spring, for which stress and strain are related by the relation $\sigma = \mu\epsilon$, where μ is the elastic modulus. The simple viscous element is represented by a dashpot for which the constitutive relation is represented by $\sigma = \eta \dot{\epsilon}$, where η is the viscosity of the element, and $\dot{\epsilon}$ is the rate of strain.

Since rheological materials combine elastic and viscous effects, it is possible to model them approximately by combining elastic and viscous components in various parallel and series arrangements. In this study, four combinations were used to evaluate the creep function, $J(t)$, under long term cyclic loading. These elasto-viscous models were the Maxwell Model (Figure 5.1), the Kelvin-Voigt Model (Figure 5.2), the Standard Linear Model (Figure 5.3), and the Burgers Model (Figure 5.4). The expressions for permanent deformation appropriate to these models were derived (see Appendix A) and are presented below.

The one-dimensional deformation of a soil layer at a given moment $S(t)$ is

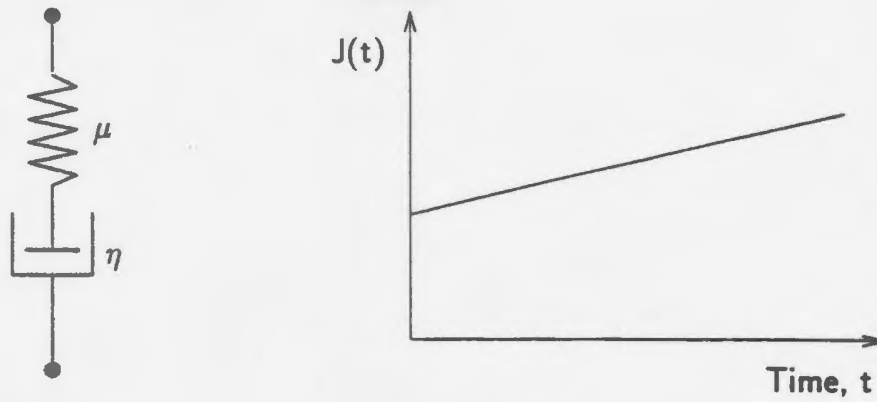


Figure 5.1: Maxwell Model.

$$S(t) = \sum_{i=1}^M \epsilon_i(t) \Delta H_i \quad (5.5)$$

where

M is the number of soil layers,

$\epsilon_i(t)$ is the strain of the i th layer, and

ΔH_i is the height of the i th layer.

From the following derivations, the respective expressions of strain for the four models can be obtained.

5.1.1 Maxwell Model

The creep function for the Maxwell Model is given by (Lockett, 1972)

$$J(t) = \left(\frac{1}{\mu} + \frac{1}{\eta} t \right) * I(t). \quad (5.6)$$

By substituting this equation for $J(t)$ in Eqn (5.4), the following can be derived as shown in Appendix A:

For the loading period

$$\epsilon(\bar{t}) = \left(\frac{1}{\mu} + \frac{NT}{\eta} + \frac{\bar{t}}{\eta} \right) \sigma_d. \quad (5.7)$$

For the unloading period

$$\epsilon(\bar{t}) = \frac{(N+1)T}{\eta} \sigma_d. \quad (5.8)$$

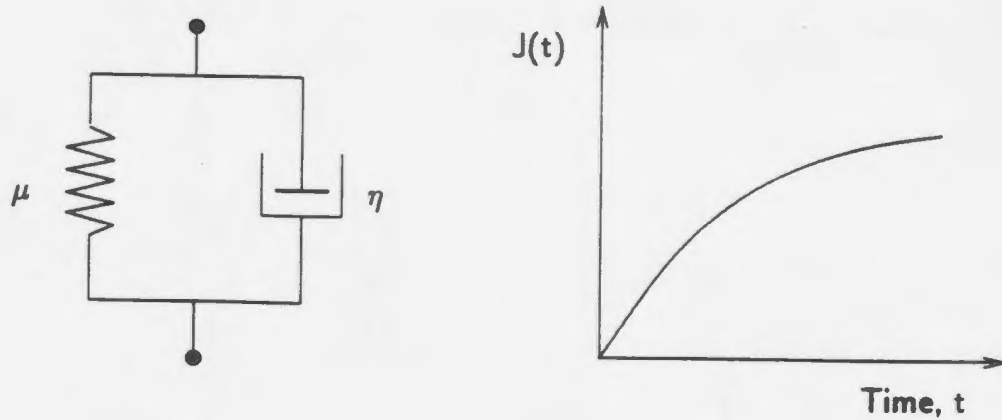


Figure 5.2: Kelvin-Voigt Model.

5.1.2 Kelvin-Voigt Model

The creep function of the Kelvin-Voigt Model is (Lockett, 1972)

$$J(t) = \frac{1}{\mu}(1 - e^{-\frac{\mu}{\eta}t})I(t). \quad (5.9)$$

Substitution of the above in Eqn (5.4) can lead to the deduction of the following (shown in Appendix A):

For the loading period

$$\epsilon(\bar{t}) = \frac{\sigma_d(1 - e^{-\frac{\mu}{\eta}T})(1 - e^{-\frac{2N\mu}{\eta}T})}{\mu(1 - e^{-\frac{2\mu}{\eta}T})}e^{-\frac{\mu}{\eta}\bar{t}} + \frac{\sigma_d}{\mu}(1 - e^{-\frac{\mu}{\eta}\bar{t}}). \quad (5.10)$$

For the unloading period

$$\epsilon(\bar{t}) = \left[\frac{\sigma_d(1 - e^{-\frac{\mu}{\eta}T})(1 - e^{-\frac{2N\mu}{\eta}T})}{\mu(1 - e^{-\frac{2\mu}{\eta}T})} + \frac{\sigma_d}{\mu}(e^{-\frac{\mu}{\eta}T} - 1) \right] e^{-\frac{\mu}{\eta}\bar{t}}. \quad (5.11)$$

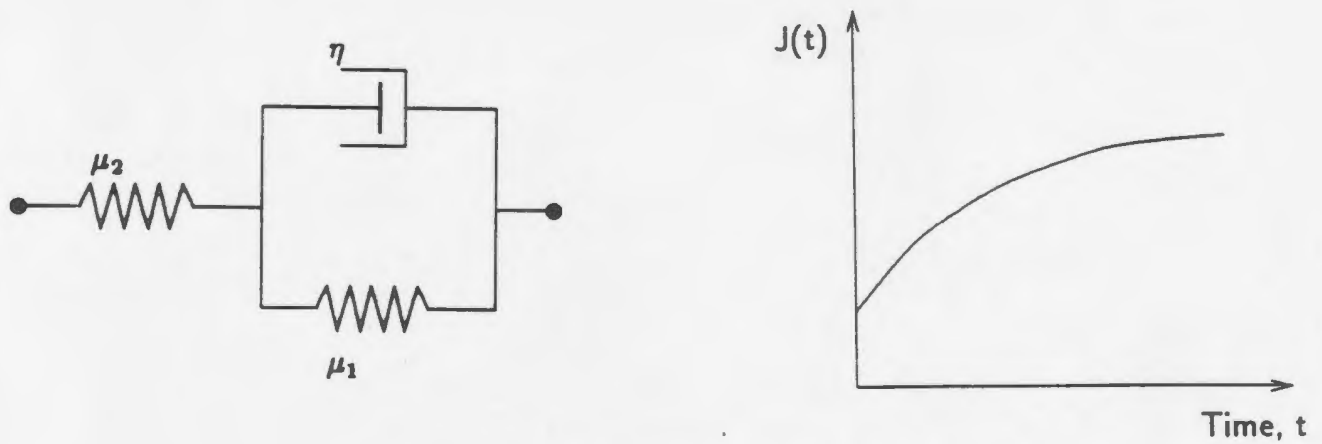


Figure 5.3: Standard Linear Model.

5.1.3 Standard Linear Model

The creep function for this model is (Lockett, 1972)

$$J(t) = \frac{1}{E_R} \left[1 - \left(1 - \frac{\tau_\epsilon}{\tau_\sigma} \right) e^{-\frac{t}{\tau_\sigma}} \right] \quad (5.12)$$

where

$E_R = \mu_2$ elastic modulus during relaxation,

$\tau_\epsilon = \frac{\eta}{\mu_1}$ relaxation time of displacement, and

$\tau_\sigma = \eta \left(\frac{1}{\mu_1} + \frac{1}{\mu_2} \right)$ relaxation time of loading.

Substitution of Eqn (5.12) in Eqn (5.4) leads to the following:

For the loading period

$$\epsilon(\bar{t}) = \sigma_d \{ A + [B + C(1 - e^{-\frac{2NT}{\tau_\sigma}})] e^{-\frac{\bar{t}}{\tau_\sigma}} \}. \quad (5.13)$$

For the unloading period

$$\epsilon(\bar{t}) = \sigma_d [C(1 - e^{-\frac{2NT}{\tau_\sigma}}) + B(1 - e^{-\frac{\bar{t}}{\tau_\sigma}})] e^{-\frac{\bar{t}}{\tau_\sigma}} \quad (5.14)$$

where

$$A = \frac{1}{E_R},$$

$$B = -\frac{1}{E_R} \left(1 - \frac{\tau_\epsilon}{\tau_\sigma} \right), \text{ and}$$

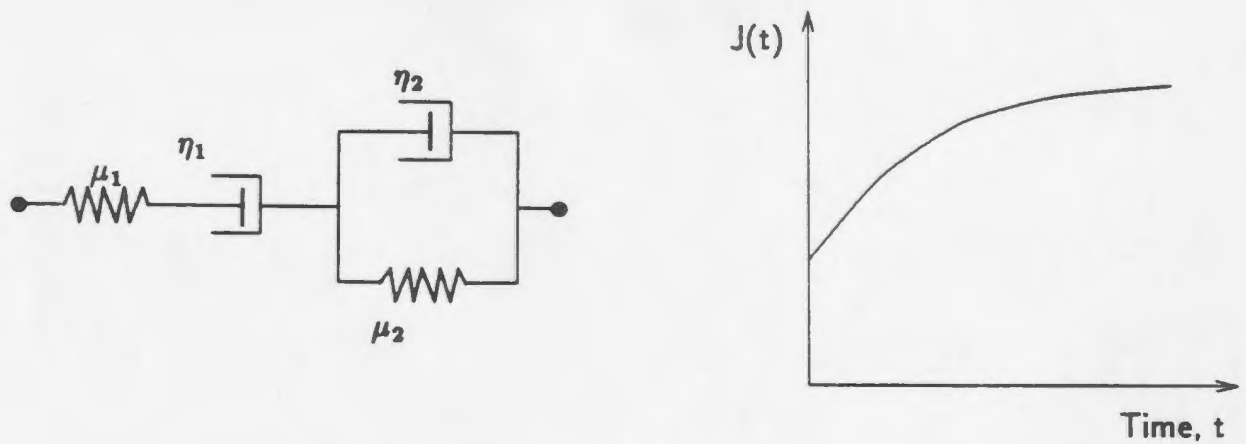


Figure 5.4: Burgers Model.

$$C = \frac{(1 - \frac{\tau_1}{\tau_0})(1 - e^{-\frac{T}{\tau_0}})}{E_R(1 - e^{-\frac{2T}{\tau_0}})}$$

5.1.4 Burgers Model

The creep function of the model is given by (a combination of the Maxwell Model and the Kelvin-Voigt Model):

$$J(t) = \frac{1}{\mu_1} + \frac{1}{\mu_2} + \frac{t}{\eta_1} - \frac{1}{\mu_2} e^{-\frac{\mu_2}{\eta_2} t} \quad (5.15)$$

Substitution of Eqn (5.15) in Eqn (5.4) produces the following:

For the loading period

$$\epsilon(\bar{t}) = \sigma_d \{ (A + NBT) + [CE(e^{-2NTD} - 1) + C]e^{-D\bar{t}} + B\bar{t} \} \quad (5.16)$$

For the unloading period

$$\epsilon(\bar{t}) = \sigma_d \{ (N + 1)BT + [CE(e^{-2NTD} - 1) + C(1 - e^{DT})]e^{-D\bar{t}} \} \quad (5.17)$$

where

$$A = \frac{1}{\mu_1} + \frac{1}{\mu_2},$$

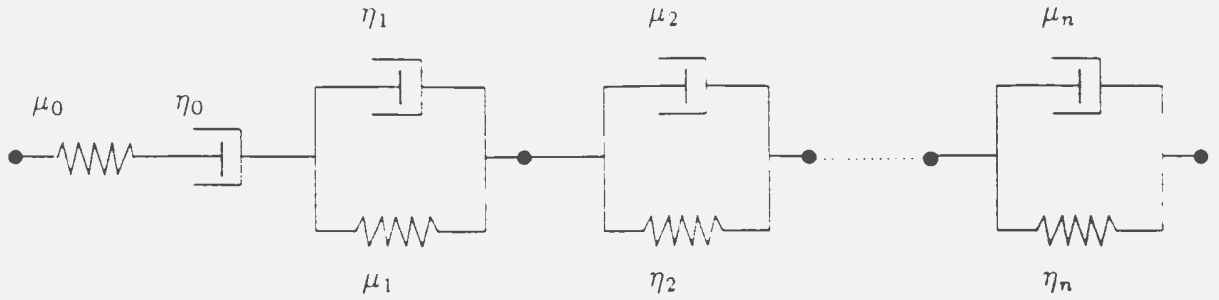


Figure 5.5: Generalized Burgers Model.

$$B = \frac{1}{\eta_1},$$

$$C = -\frac{1}{\mu_2},$$

$$D = \frac{\mu_2}{\eta_2}, \text{ and}$$

$$E = \frac{1 - e^{DT}}{1 - e^{2DT}}.$$

To quantitatively fit the true creep curve, a more complex model is required. The following equation introduces the Generalized Burgers Model (Figure 5.5).

The creep function for this model is

$$J(t) = \frac{1}{\mu_0} + \frac{1}{\eta_0}t + \sum_{i=1}^n \frac{1}{\mu_i} (1 - e^{-\frac{\mu_i}{\eta_i} t}). \quad (5.18)$$

The proper selection of the parameters μ_i and η_i in the model can yield a good fit of the true creep curve.

5.2 Test Materials and Load Form

The samples investigated in this portion of the study were Beaufort Sea Clay (BS Clay) and Lundrigan Silt (L Silt). Frequencies of 0.01 - 0.1 Hz are of interest when considering introgravity and gravity wave loading. Testing frequencies of 0.1 and

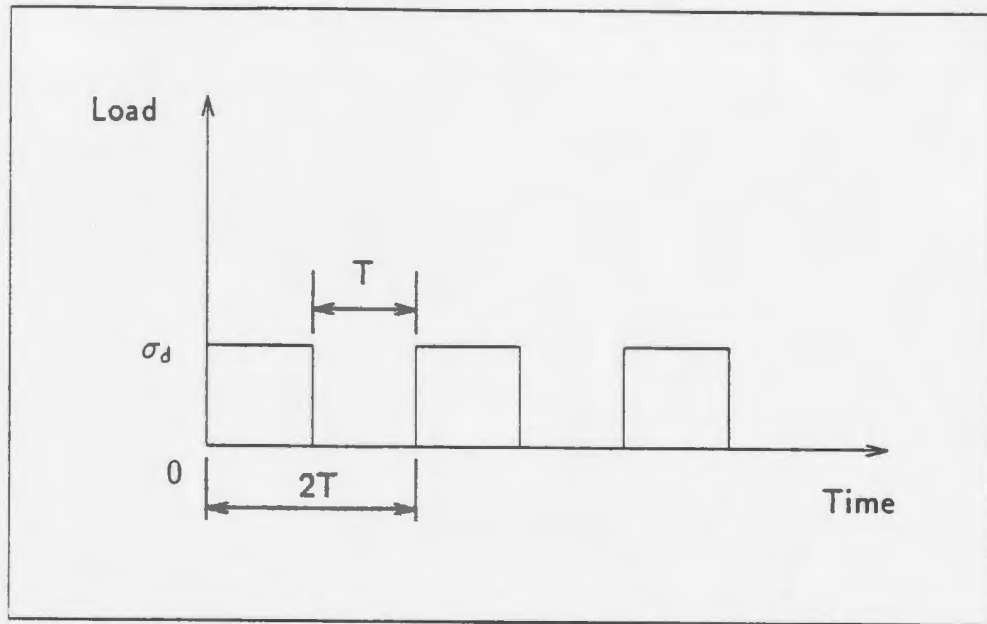


Figure 5.6: Plot of Applied Loading.

0.01 Hz were chosen to correspond to a gravity wave and an introgravity wave respectively. The long term deformation characteristics of the soils were tested at these frequencies. A square wave cyclic loading (see Figure 5.6) was used to simulate waves or storms.

The tests were conducted on isotropically consolidated specimens under the condition of two-way open drainage.

5.3 Description of Results

The test results are shown in Figure 5.7, Figure 5.8 and Figure 5.9, where σ_3 is the confining pressure and σ_d is axial cyclic deviatoric load. In Figure 5.7, the jumps shown in (a), (b) and (c), at times of approximately 120s, 600s, and 1200s respectively, are due to the fact that only deformations at the beginning and at the end of the time period were recorded. This was due to the memory limitation of the computer. The total test times are shown on the graphs. Deformation

characteristics of Beaufort Sea Clay and Lundrigan Silt can be obtained from these deformation curves and are summarized as follows:

- The curves of permanent deformation caused by the cyclic loading fell between the deformation curves for rapidly applied static loadings of σ_0 and $\frac{1}{2}\sigma_0$ (see Figure 5.10). The definition of rapidly applied static loading is shown in Figure 5.11. The actual distance between the curves was a function of the OCR of the soil and the cyclic period of the loading. The distance between the central axial cord of the deformation curve caused by axial cyclic deviatoric loading, σ_d , and the deformation curve of rapidly applied static loading $\frac{1}{2}\sigma_0$ was inversely proportional to the degree of consolidation and the loading frequency; the distance was directly proportional to the magnitude of permanent deformation.
- The loading phase consisted of an initial (elastic) deformation phase and an ensuing phase of plastic deformation and viscous flow; whereas an unloading phase was composed of an initial (elastic) rebound phase and an ensuing phase of elastic after-effect (viscous recovery following the initial elastic rebound) (see Figures 5.7c and 5.7d, etc.).
- The average (i.e. the central axial cord) deformation curve of the cyclic loadings approximated a static deformation curve (see Figure 5.8c, etc.). After long term loading and unloading, the value of double amplitude strain (i.e. peak-to-peak strain) in the deformation curves tended to be constant, i.e., the sample reached steady-state vibration (see Figure 5.8d, etc.). The slope of the average deformation curve may approach zero or a finite non-zero value depending on the type of soil, the magnitude of cyclic loading, the OCR and the frequency of loading.
- The higher the confining pressure, the smaller the permanent deformation. This is because confining pressure restricts the lateral expansion of the soil and increases stiffness (see Figures 5.7a and 5.7b). The smaller the cyclic

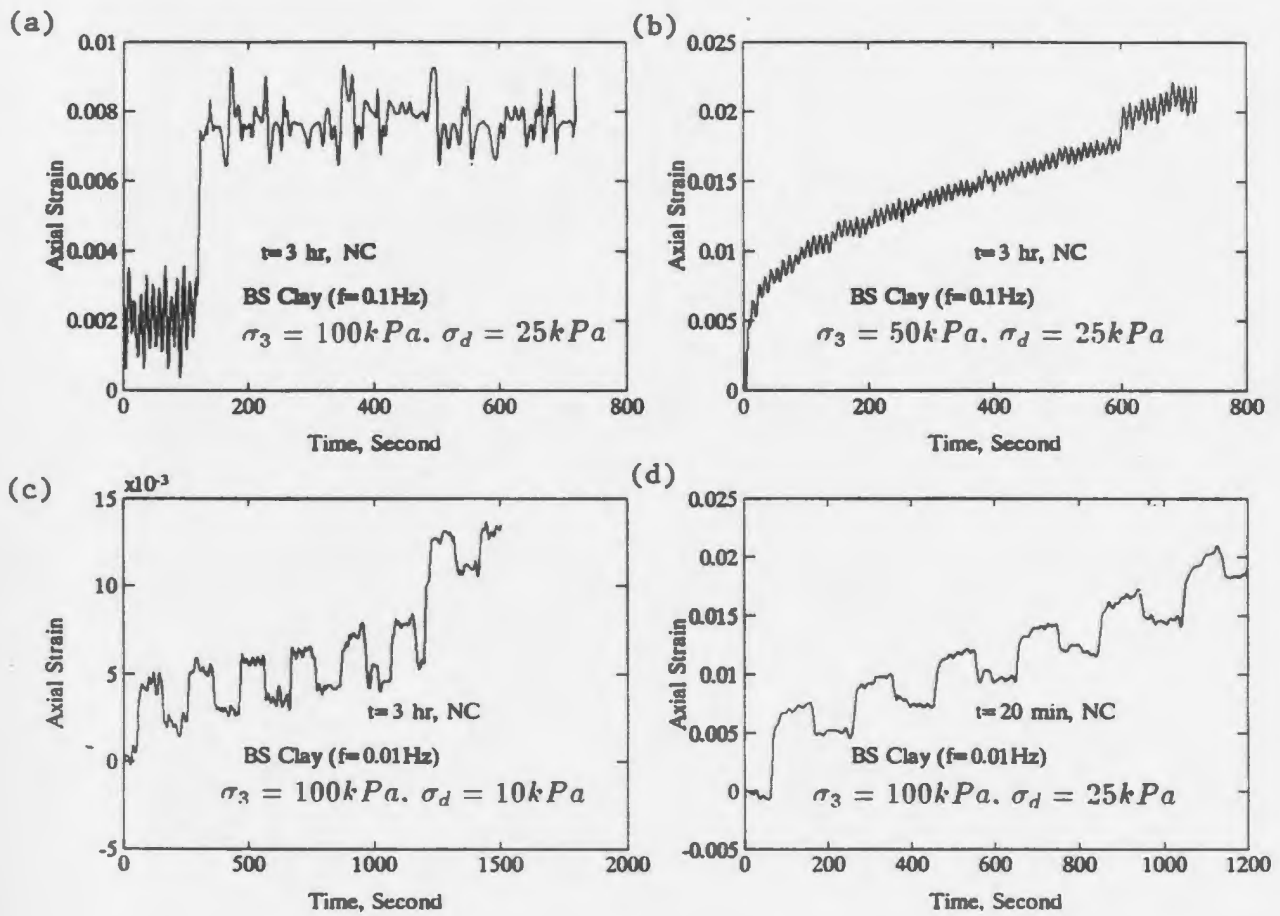


Figure 5.7: Test Results for Beaufort Sea Clay.

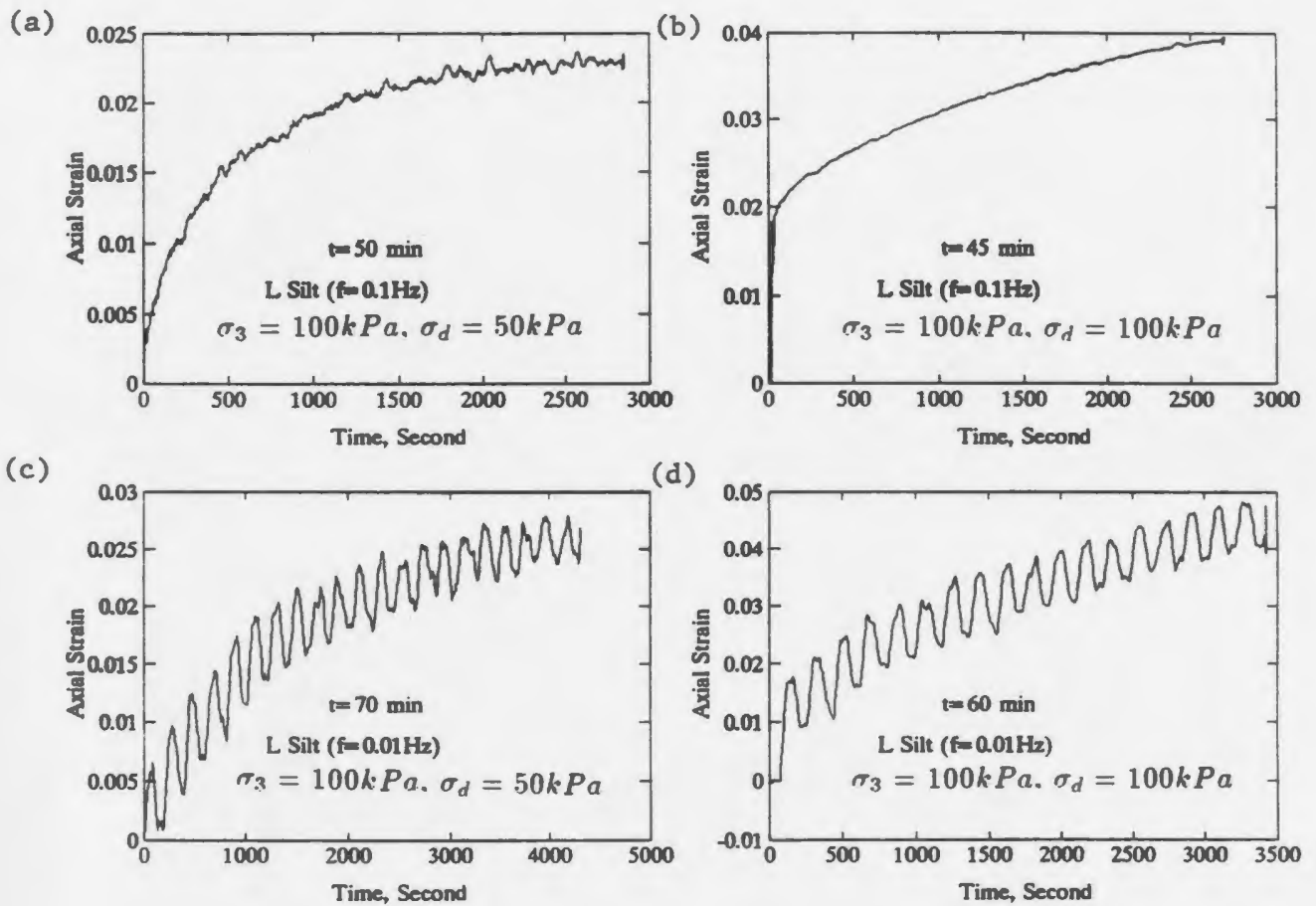


Figure 5.8: Test Results for NC State Lurdrigan Silt ($\sigma_3 = \sigma_c = 100$ kPa).

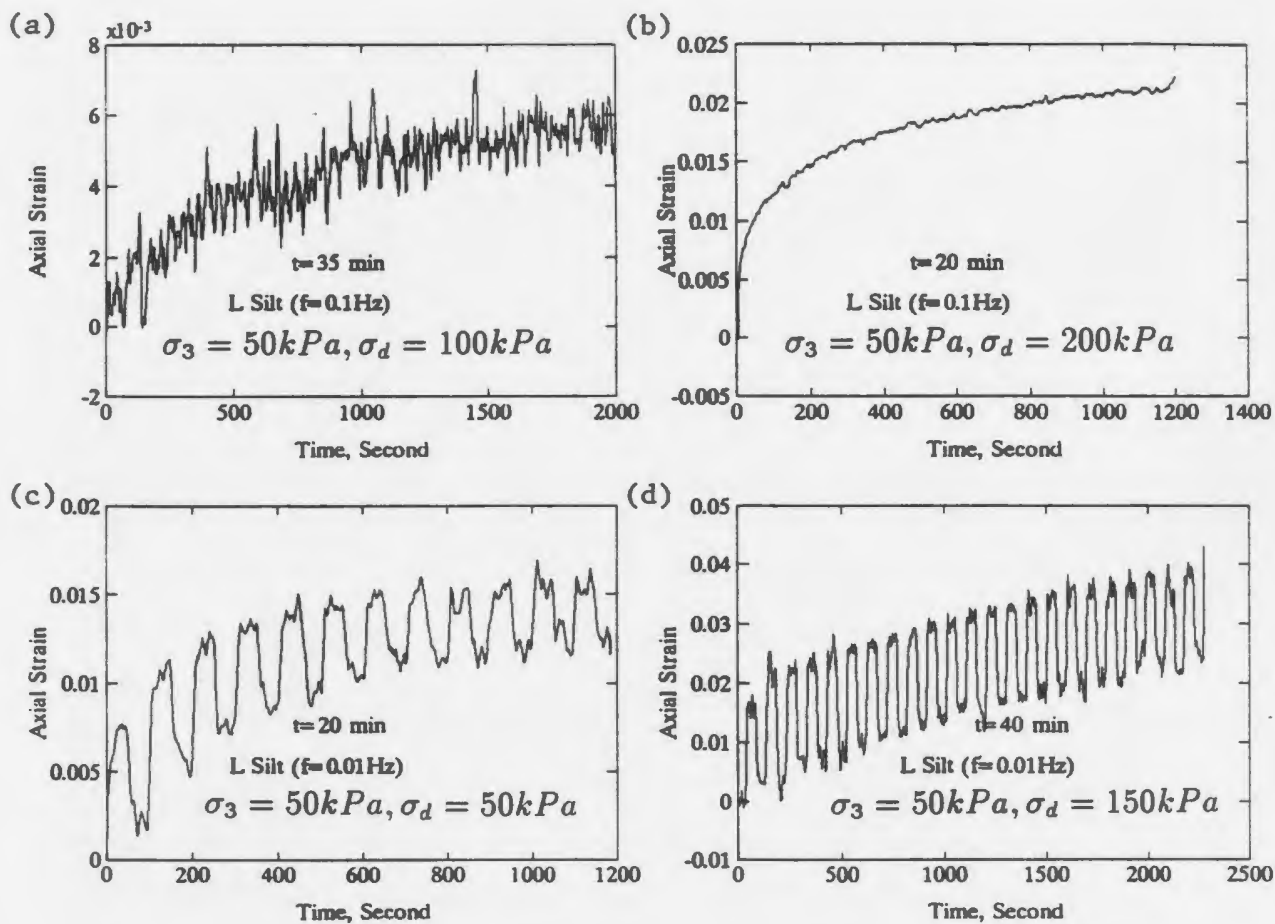


Figure 5.9: Test Results for OC State Lundrigan Silt ($\sigma_3 = \frac{1}{2}\sigma_c = 50$ kPa).

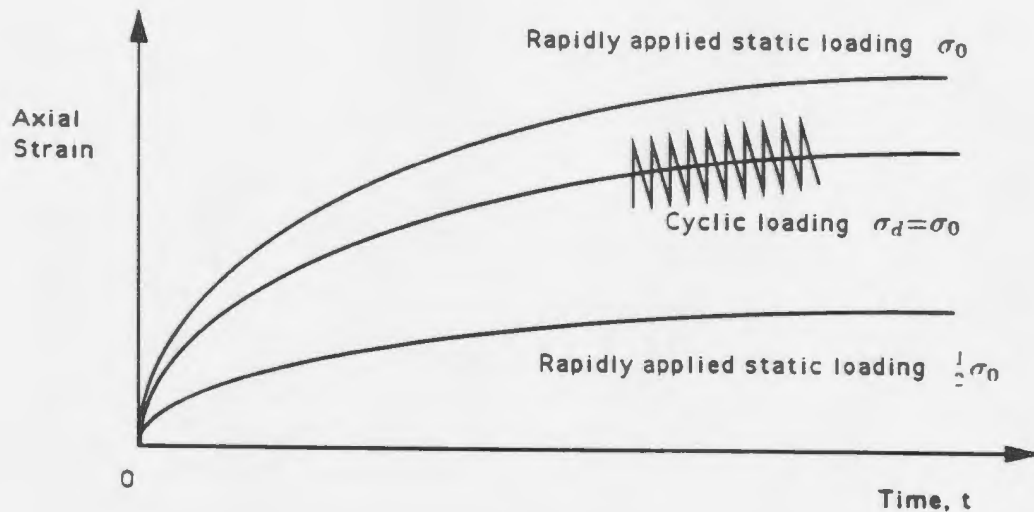


Figure 5.10: Relationship between Static and Cyclic Loading.

period, the smaller the permanent deformation and the vibration amplitude of the sample (see Figures 5.7a and 5.7d, and Figures 5.8b and Figure 5.8d, etc.).

- More elasticity (relatively small permanent deformation or relatively large rebound) is shown in Lundrigan Silt than in Beaufort Sea Clay due to the former's lower plasticity. More elasticity is shown in the specimens subjected to higher vibration frequency than in those subjected to lower vibration frequency (see Figures 5.8a and 5.8c, etc.). The ideal elastic material vibrates about the static deformation curve of one-half applied cyclic loading, i.e., the deformation curve caused by a static loading $\sigma_0 = \frac{1}{2}\sigma_d$. Relatively speaking, overconsolidated (OC) soils exhibit more noticeable elasticity (e.g., more rebound) than normally consolidated (NC) soils do, and so their residual deformation value is found to be smaller (see Figures 5.8c and 5.9c).

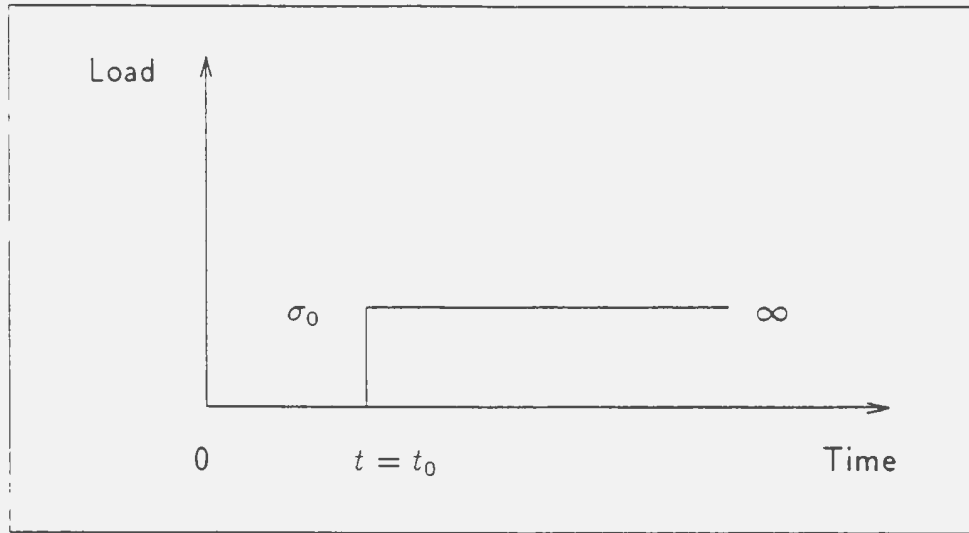


Figure 5.11: Definition of Rapidly Applied Static Loading.

- Previous tests (Mulilis et al., 1978) have shown that a much larger deformation is caused by rapidly applied loads (e.g. square wave cyclic loading) than by progressively applied loads (e.g. sine wave cyclic loading, triangular wave cyclic loading or trochoidal wave cyclic loading). Therefore, the selection of square wave cyclic loading in this study to evaluate permanent deformations caused by gravity waves is conservative.

5.4 Comparison Between the Theoretical and Test Results

The numerical analysis results from this study for the Kelvin-Voigt and Burgers Models are shown in Figure 5.12 and Figure 5.13. Figure 5.14 displays the permanent deformations obtained from the different rheological models. By comparing Figure 5.14 with Figure 5.8c, the following conclusions relevant to the four rheo-

logical models can be made.

- The Maxwell Model reflects the initial deformation and the following constant rate of viscous flow of the soil, which would be more suitable to soft clay and mud (Figure 5.14d).
- The Kelvin-Voigt Model disregards the initial deformation of the soil, but takes into account the non-linearity of the deformation of cohesive soils (Figure 5.14c). It can approximately simulate the deformation characteristics of high plasticity soils or rapidly dynamically loaded soils (e.g., $f \geq 0.1\text{Hz}$, see Figures 5.13a and b, etc.), as the initial deformation can be roughly regarded as zero.
- The Standard Linear Model can reflect the initial elastic rebound and elastic after-effect of the soil, but it fails to reflect the non-linear viscous flow of the soil (Figure 5.14b). Therefore, it is a more appropriate model to use in the initial period of the creep or deformation of OC soils (see Figures 5.9d and 5.14b, neglect the difference in σ_d).
- Being a series combination of the Maxwell Model and the Kelvin-Voigt Model, the Burgers Model can reflect not only the elastic after-effect, but also the viscous flow of the soil (Figure 5.14a). Therefore, it gives a better qualitative prediction than other soil models. This can also be seen in Figures 5.12c, 5.12d, 5.13c, and 5.13d.

Looking at the deformation curves obtained from numerical analysis and test results (Figures 5.12, 5.7, 5.13, and 5.8) indicates that the actual permanent deformation values obtained from laboratory tests and the theoretical permanent deformation values achieved in the numerical modeling are close. Also, the numerical analysis curves fit the actual permanent curves in shape although the curves in Figure 7 did not turn out very well due to the memory limitations of the computer. The comparison made between the characteristics of the deformation curves, be-

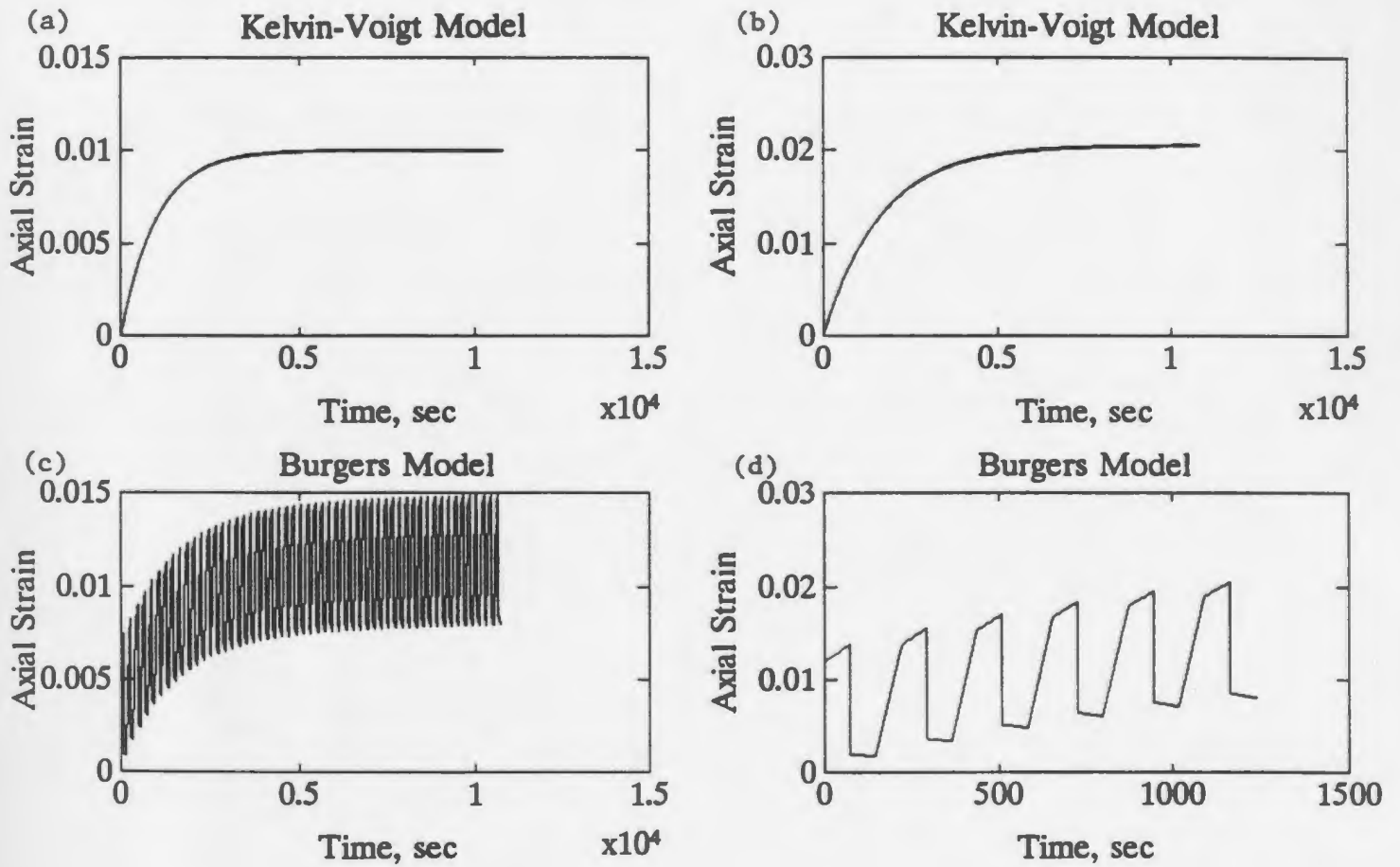


Figure 5.12: Theoretical Deformation Curves for BS Clay (Corresponding to Figure 5.7).

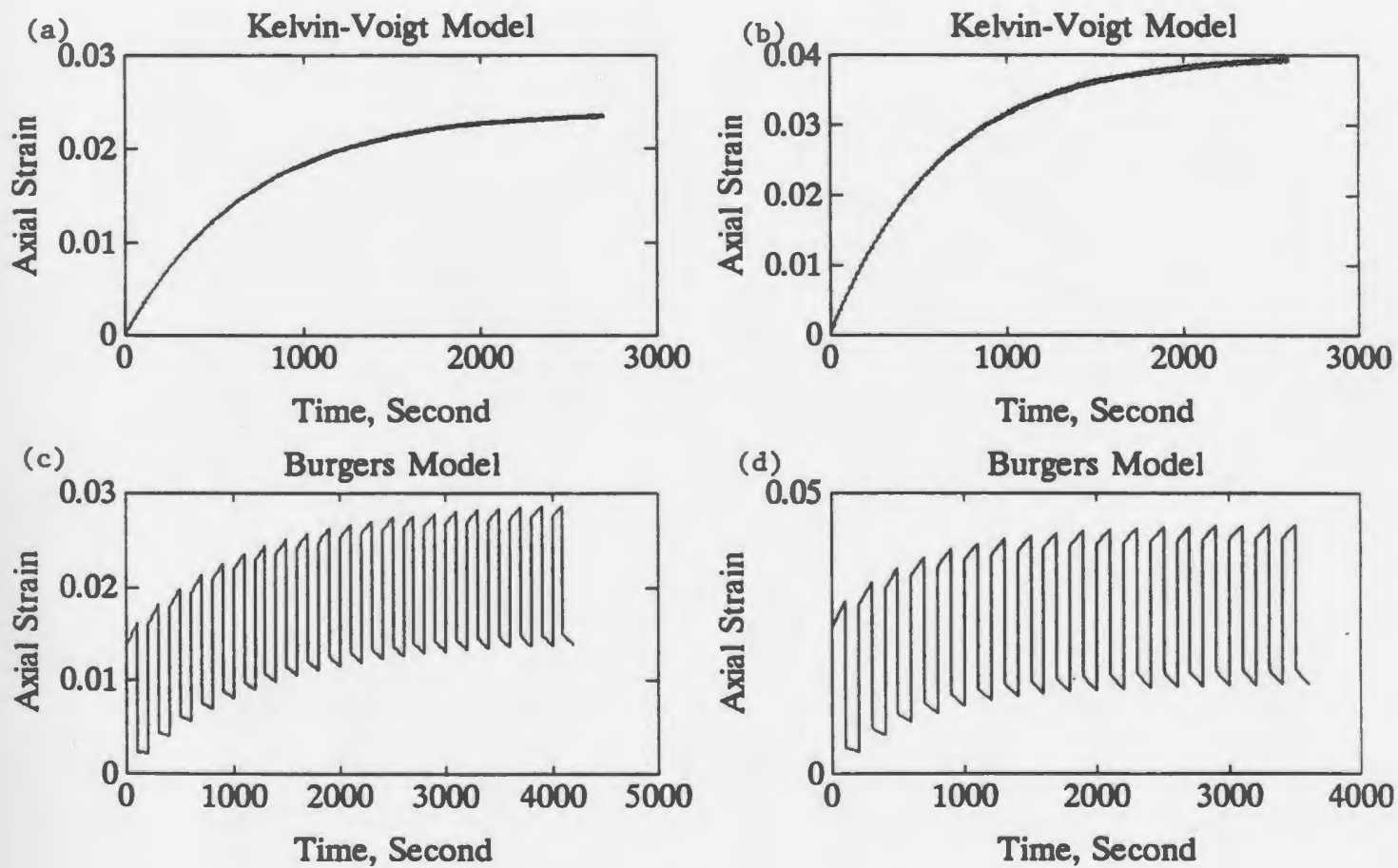


Figure 5.13: Theoretical Deformation Curves for L Silt (Corresponding to Figure 5.8).

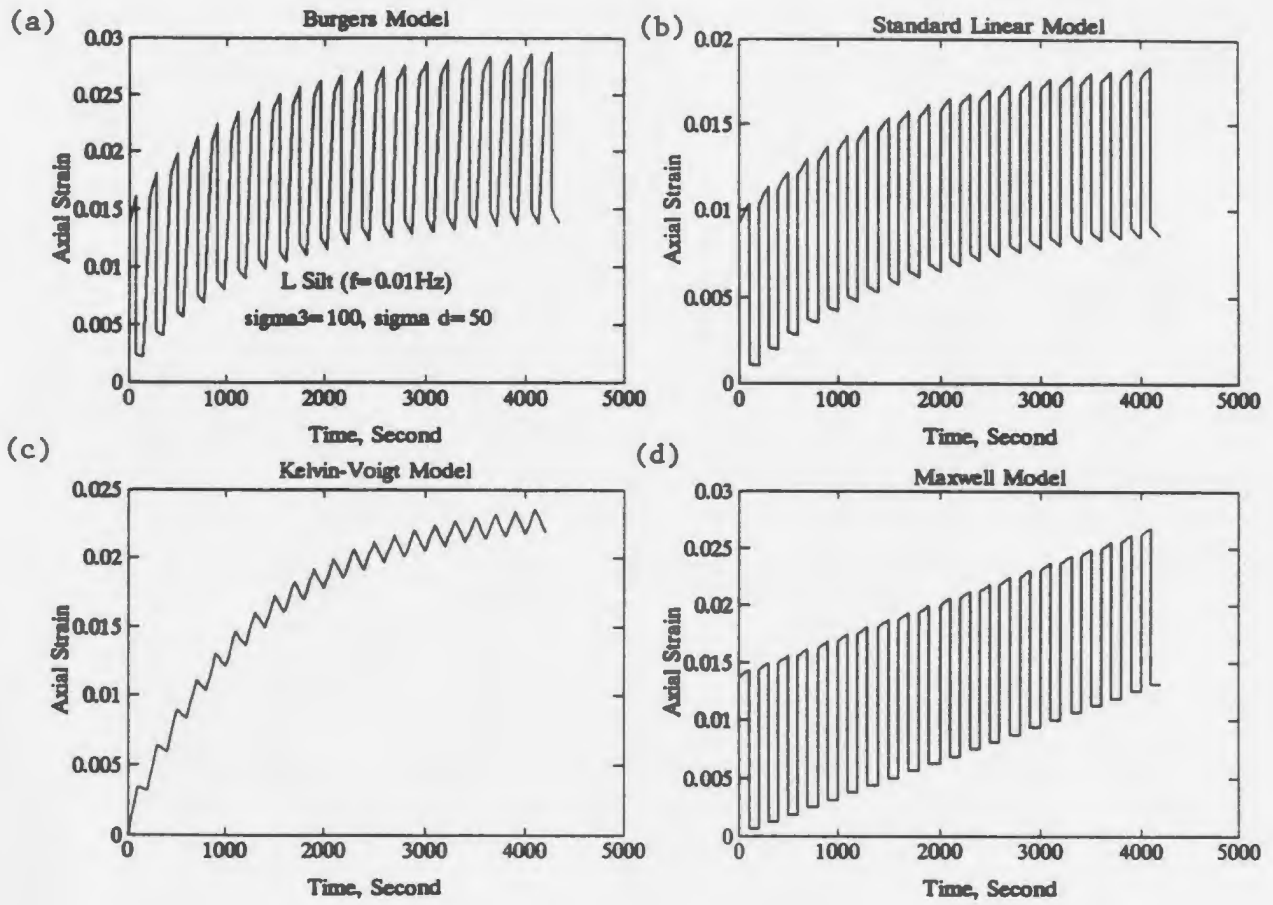


Figure 5.14: Comparison Between Different Models.

tween the permanent deformation values and between numerical analysis and test results leads to the following conclusions.

The deformation characteristics described in the results of the last section are reflected in the rheological models as shown in the respective deformation curves. The models also reflect the rebound of the soil during unloading. The permanent deformation values shown in the figures indicate that the deformation values obtained from the rheological models are close to the actual deformations. For soils with high plasticity, like Beaufort Sea Clay, taking viscous flow into account is important during the evaluation of the deformation under long term cyclic loading. In addition, the longer the cyclic period of repeated loading, the better the results from the rheological models, as the soil is allowed to develop viscous deformation under long period loading.

5.5 Determination of Creep Function – Creep Test

In a creep test, the material specimen, which is initially in a virgin state, is subjected to an instantaneous load which is varied in such a manner so as to keep the effective stress at a constant value after load application. The resulting deformation or strain in the specimen is measured as a function of the time elapsed from application of the load. If the time of load-application is chosen as the origin of the time scale, the stress in the specimen will have the form

$$\sigma(t) = \sigma_0 * I(t). \quad (5.19)$$

In the above equation, σ_0 is a constant depending on the magnitude of the applied load and the dimensions of the specimen, and $I(t)$ denotes the Heaviside step function. The strain responds to the stress in the form

$$\epsilon(t) = \sigma_0 * J(t). \quad (5.20)$$

Thus the creep function, $J(t)$, can be readily determined by dividing the measured strain response by the known constant σ_0 . The μ and η values for the different

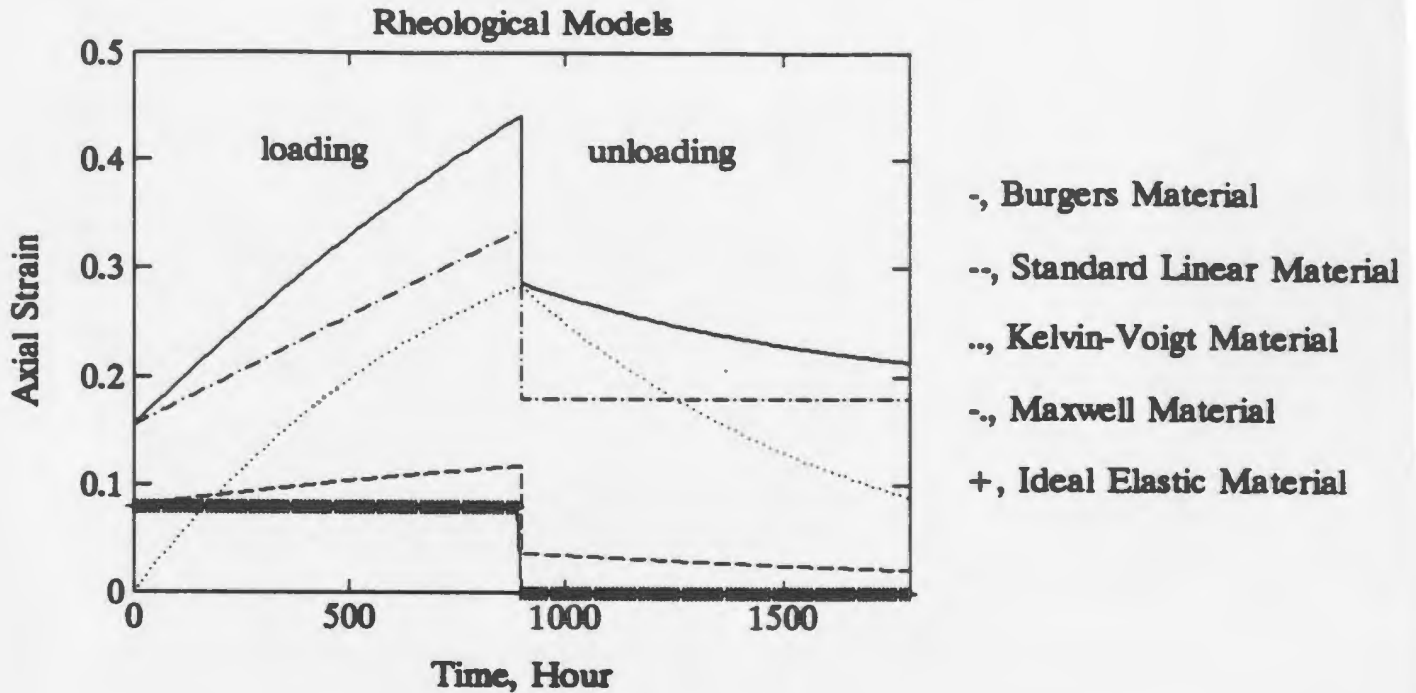


Figure 5.15: Creep Features for Different Materials.

rheological materials used in this study were obtained from the available data and back analyses of the specified oedometer test data.

The general features of the creep function for various materials are shown schematically in Figure 5.15. Provided that inertia effects are negligible, the strain in an elastic material immediately attains some value and then remains constant. For a viscous fluid, the material flows at a constant rate, so that $J(t)$ is proportional to time, t . These remarks are consistent with the requirements that $J(t) = 1/\mu$ and $J(t) = t/\eta$ in order to obtain the constitutive relations for elastic and viscous materials. In a rheological material there is a relatively rapid increase in $J(t)$ for small values of t (i.e., soon after application of the load), which may (e.g., the Burgers material) or may not (e.g., the Kelvin-Voigt material) contain an instantaneous elastic component. As t increases, the slope of the curve decreases and as $t \rightarrow \infty$ the slope may approach zero or a finite non-zero value.

Chapter 6

Liquefaction Potential and Cyclic Strength

An understanding of the behavior of marine soils is required in the dynamic analysis of offshore structures which may be subjected to earthquake excitation or loaded through storm wave action. This behavior of dynamically loaded soil is commonly expressed in terms of liquefaction potential or cyclic strength of the soil. The objective of this experimental investigation was to quantify the liquefaction resistance and cyclic strength of soils under different drainage conditions and consolidation states and to also identify other influencing factors when assessing dynamically loaded soils.

The tests were conducted on saturated specimens obtained from the Beaufort Sea and locally. The specimens investigated in this portion of the study were Nerlerk #1 sand, Nerlerk #2 sand, Nerlerk #3 sand, Nerlerk Mud and Lundrigan Silt. The Beaufort Sea soils had been previously subjected to an intensive investigation by Golder Associates on behalf of Gulf Canada Limited (Golder Associates, 1989). A description of these soils was presented in Chapter 4. Because of the range of investigations carried out on the influencing factors of dynamic strength during this portion of the study, the results are useful in the analysis of a variety of seafloor dynamic loading problems and in the earthquake engineering design of offshore structures.

Various types of laboratory testing procedures for determining liquefaction potential or cyclic strength of soils are available, such as the cyclic triaxial, cyclic sim-

ple shear and torsional shear tests. In this portion of the study, the cyclic triaxial test was used to investigate the liquefaction potential and strength characteristics of the soils.

6.1 Criteria of Liquefaction and Cyclic Strength

The most commonly used liquefaction criterion for liquefiable cohesionless soils is the initial liquefaction criterion. The initial liquefaction corresponds to the condition when the pore water pressure, u , becomes equal to the confining pressure, σ_3 . To compare the results of liquefaction tests conducted by different investigators on various types of soils, a standard curve for initial liquefaction at a given number of load cycles has been developed. This is a plot of cyclic stress ratio (CSR), $\frac{\sigma_d}{2\sigma_3}$, vs N , where σ_d is the axial cyclic deviatoric stress and N is the number of cycles to cause initial liquefaction under certain conditions. However, due to the fact that dense soil dilates when its strain exceeds a certain value, and also due to the pre-shearing effect under the consolidation condition of deviatoric stress, initial liquefaction cannot always be reached. This is because the dilation of the soil reduces pore water pressure and pre-shearing helps to stabilize the soil under dynamic load. This is referred to as cyclic mobility (Castro and Poulos, 1977). The cyclic strain criterion, therefore, was developed to consider the cyclic strength of this type of cohesionless soil or cyclic strength of cohesive soil. In most cases, 10% double amplitude strain (i.e. peak-to-peak strain) is considered failure although it depends on the type of soil. In some cases, 5%, 3%, or even 2% residual or double amplitude strain is considered as failure. It can be seen that, for a given value of σ_d , the initial liquefaction and failure occur simultaneously for loose sand. However, as the relative density of the soil increases, the difference between the number of cycles to cause 10% residual or double amplitude strain and to cause initial liquefaction (if it can even be reached) increases.

In this portion of the study, because the cyclic loading was applied through a load-controlled system, the load was one-way (from 0 to σ_d). The double amplitude

strain was thus lower than the residual strain after a certain point. For this study, a soil was determined to have reached its liquefaction potential or cyclic strength whenever either the pore pressure or the residual strain reached the corresponding liquefaction or cyclic strain criterion.

6.2 Soil Types and Test Procedures

The materials used in this investigation were the three Nerlerk sands, the Nerlerk Mud and the Lundrigan Silt. A frequency of 1 Hz was used in this portion of the study.

A series of cyclic triaxial tests were performed on Nerlerk #1, #2 and #3 sands, Nerlerk Mud and Lundrigan Silt. The estimated *in-situ* void ratio of each sample was strived for during sample preparation of the remoulded sands. The samples were isotropically consolidated to varying over-consolidation ratios (OCR) between 1.0 and 8.0. In cases where pore pressure developed slowly and did not approach liquefaction ($u = \sigma_3$), axial deformation was accepted as failure when the residual strain reached 2.5%.

6.3 Analyses of Test Results of Cohesionless Soils

6.3.1 Effect of Cyclic Stress Ratio

Cyclic stress ratio is the ratio of single amplitude cyclic deviatoric stress $\sigma_d/2$ to confining pressure σ_3 , i.e., $CSR = \frac{\sigma_d}{2\sigma_3}$. Figure 6.1 shows typical results for Nerlerk #1, #2 and #3 sands for the undrained conditions. The results are presented as plots of axial strain vs number of cycles (N) and normalized pore pressure (u/σ_3) vs number of cycles. It should be mentioned here that in most of the u/σ_3 vs N plots, there are initial values of pore pressure. This is due to the fact that the author had to open the valve for applied cyclic loading before triggering the data acquisition system located three meters away from the control panel where the valve

was mounted. The two seconds or so time difference between the start time and recording time resulted in the initial readings of pore pressures which should have been zeros. The same situation occurred in the u/σ_3 vs N plots of Chapter 7.

The test results of the Nerlerk sands showed that the number of cycles required to failure is a function of the CSR. As the CSR increased, the number of cycles to cause failure decreased. This is attributed to the effect of soil crushing at high CSR levels. The soil crushing resulted in failure by extra deformations.

In general, the pore water pressure in sands developed rapidly during the cyclic loading and failure in most cases was caused by initial liquefaction. For a CSR less than a certain value (stability threshold; for sands, this is normally very small), the buildup in pore pressure was not sufficient to cause failure by initial liquefaction in both cohesionless and cohesive soils.

6.3.2 Effect of Drainage

Figure 6.2 shows the effect of drainage on the cyclic stress ratio for Lundrigan Silt and Nerlerk #1 sand. These plots indicate that the value of CSR to achieve initial liquefaction or 2.5% strain at a given number of cycles could be 30-50% less for samples subjected to cyclic loading under undrained conditions, as compared to those under partially drained conditions. Even for a relatively slow rate of dissipation, such as under a partial drainage condition, it appears likely that a significant increase in CSR would result. This indicates that it is necessary to consider the effect of drainage for practical purposes. The determination of a precise degree of drainage could be achieved during the cyclic triaxial test through a parametric study of drainage conditions. Drainage and overconsolidation, as shown in Figure 6.2(b), have similar effects on the increase of liquefaction resistance in that the number of cycles required to induce liquefaction or 2.5% residual strain is increased for a given CSR.

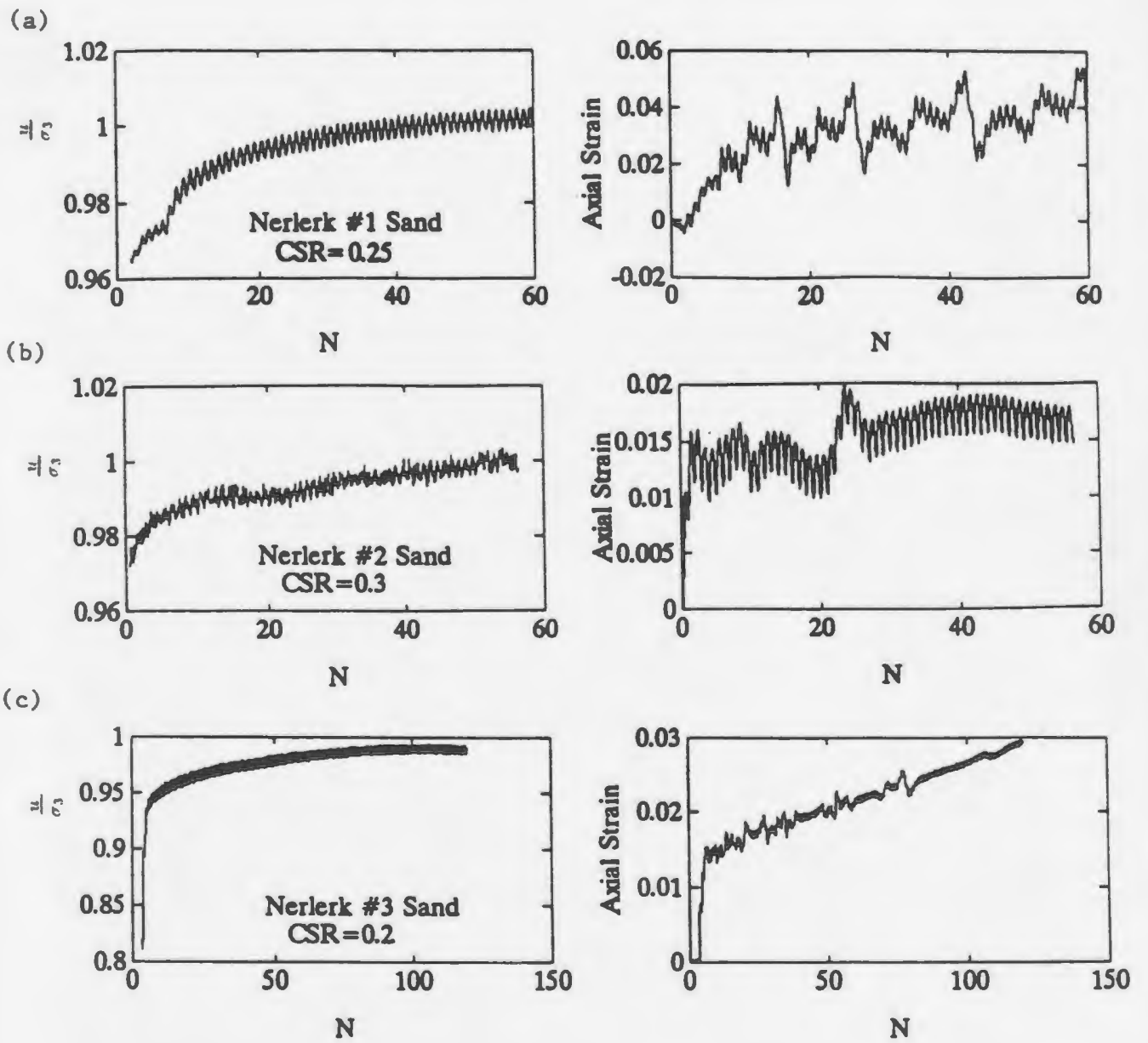
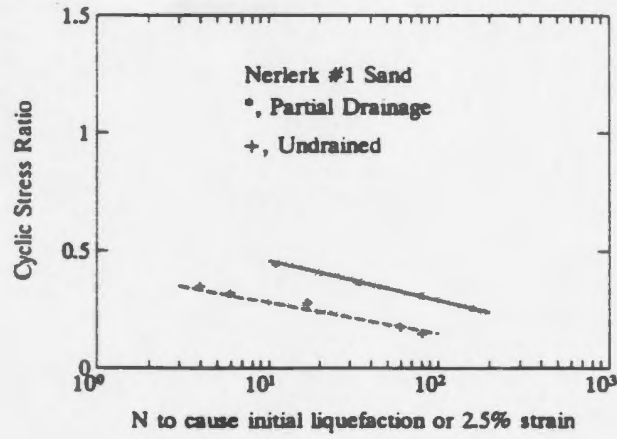


Figure 6.1: Typical Results from Nerlerk Sands (a) Nerlerk #1 Sand, (b) Nerlerk #2 Sand, and (c) Nerlerk #3 Sand.

(a)



(b)

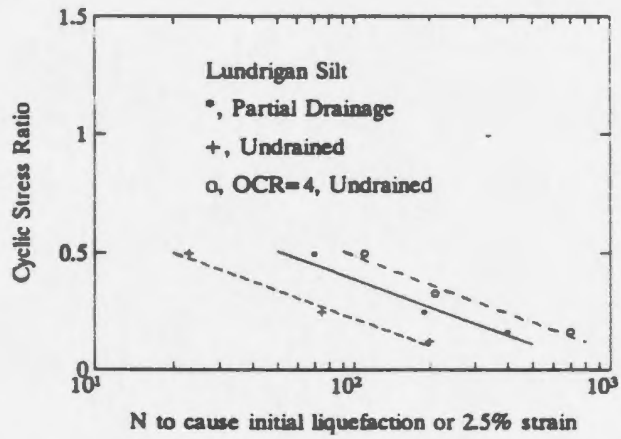


Figure 6.2: Effect of Drainage on Liquefaction Resistance (a) Nerlerk #1 Sand and (b) Lundrigan Silt.

6.3.3 Effect of Dilatancy

Overall test results obtained from dense Nerlerk #2 sand specimens indicated that the samples did not fail under the same cyclic stress ratio conditions which caused initial liquefaction in medium dense samples. The test results also indicated that as the confining pressure was increased, the decrease in the rate of pore pressure was not as great. In no case, did pore pressures reach negative values. This means that the confining pressure can impede the decrease of the pore pressure.

Figure 6.3 shows the typical results for dense Nerlerk #2 sand ($D_r = 75\%$) obtained from the cyclic triaxial tests. These tests typically showed that normalized pore pressure increased rapidly in the first few cycles, and subsequently decreased. The final value of the pore pressure in some cases was lower than the initial value of pore pressure. As can be seen from comparing Figure 6.3(a) and 6.3(b), this phenomenon is more evident under conditions of lower axial cyclic deviatoric stress.

This behavior indicates that the dense Nerlerk #2 sand is to some degree dilatant. The failure was not caused by excess pore water pressure as in the case of medium dense Nerlerk #2 sand, but through excessive axial deformation. Dilation in the dense Nerlerk #2 sand also lengthened the time to failure of the samples and also retarded the development of axial deformation.

6.4 Dynamic Behavior of Nerlerk Mud and Lundrigan Silt

The cyclic characterization of normalized behavior of NC and OC offshore clays has been verified by Vucetic (1988). The test results of u and σ_d are thus presented as the plots of $\frac{u}{\sigma'_3}$ and $\frac{\sigma_d}{2\sigma'_3}$ (CSR) versus the number of cycles N , where σ'_3 is the consolidation stress σ'_c for NC clays, and apparent preconsolidation pressure σ'_p for OC clays.

For all samples, the residual pore water pressure, u , increased progressively with the number of cycles of loading as shown in Figure 6.4, only if the cyclic deviatoric

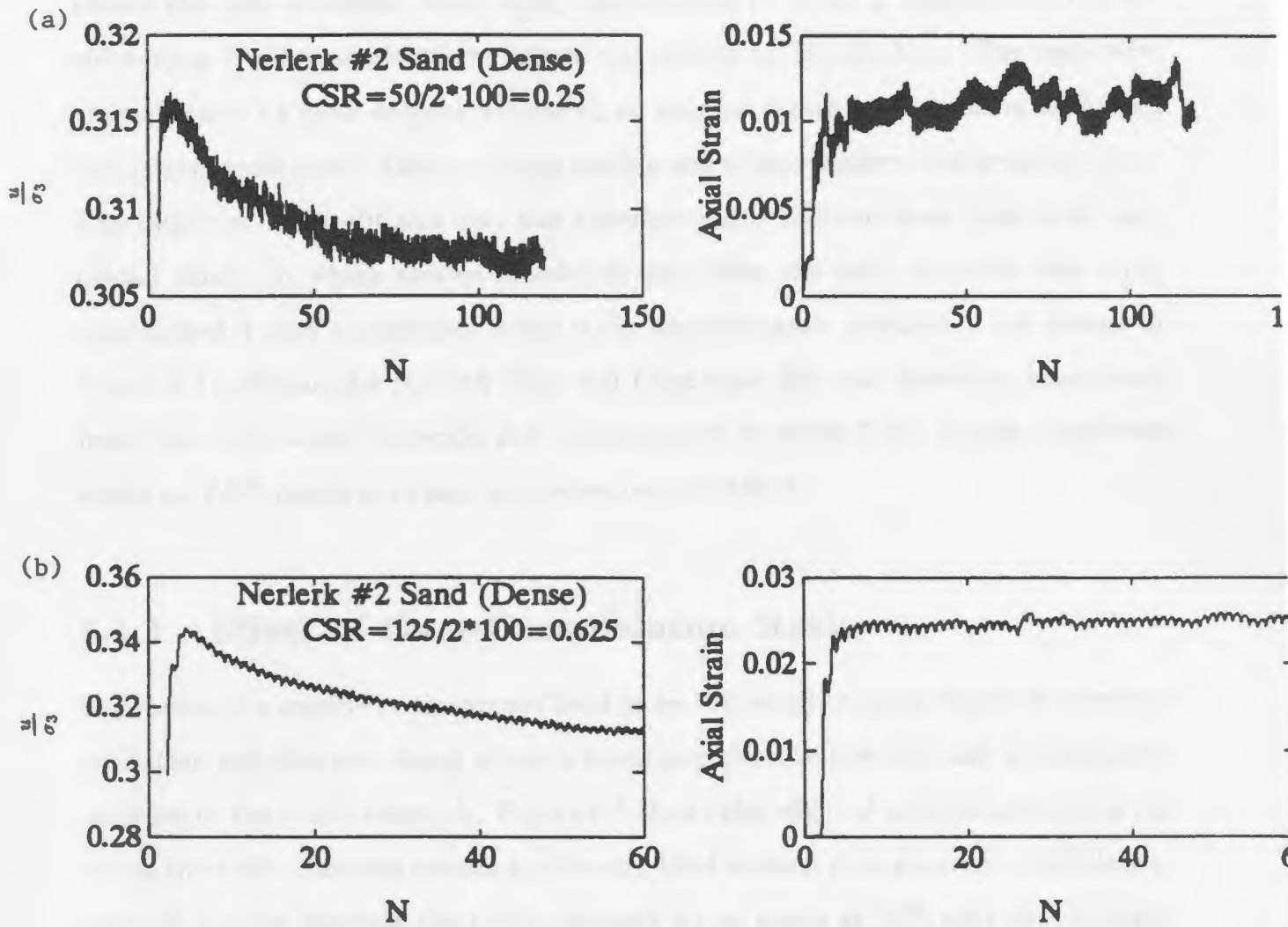


Figure 6.3: Effect of Dilatancy in Dense Nerlerk #2 (a) $CSR=0.25$ and (b) $CSR=0.625$.

stress level exceeded the stability threshold. The strain was not symmetrical about a horizontal axis even for the first few cycles except for those samples tested at a stress level below the stability threshold. Rather, the residual strain increased rapidly after the start of testing. For samples tested above the stability threshold, in most cases it was observed that large cyclic strains in excess of 2.5%, occurred before the pore pressure ratio, u/σ'_3 , approached 1. This is contrary to test results using Nerlerk sands where failure was caused by liquefaction. The tests were characterized by peak-to-peak strain, ϵ_c , or residual strain ϵ_a , increasing with each successive stress cycle. Failure during testing was always under a compression state. The behavior of the silt and clay was therefore quite different from that of the saturated sands, in which strains developed only after the pore pressure ratio u/σ'_3 approached 1 and accelerated when u/σ'_3 approximately equaled 1 (as shown in Figure 6.1). Failure for Nerlerk Mud and Lundrigan Silt was therefore determined from the cyclic strain criterion and corresponded to either 2.5% double amplitude strain or 2.5% residual strain, whichever occurred first.

6.4.1 Effect of Over-Consolidation Ratio

Sediments in a marine environment tend to be subjected to some degree of overconsolidation and this may bring about a hardening effect in the soils and a consequent increase in the cyclic strength. Figure 6.5 shows the effect of over-consolidation ratio on the CSR. The test results for Nerlerk Mud showed that an over-consolidation ratio of 2 could increase the cyclic strength by as much as 70% over the strength of normally consolidated specimens. The OCR effect in Lundrigan Silt was not as pronounced as in Nerlerk Mud. This may be interpreted as the influence of particle size.

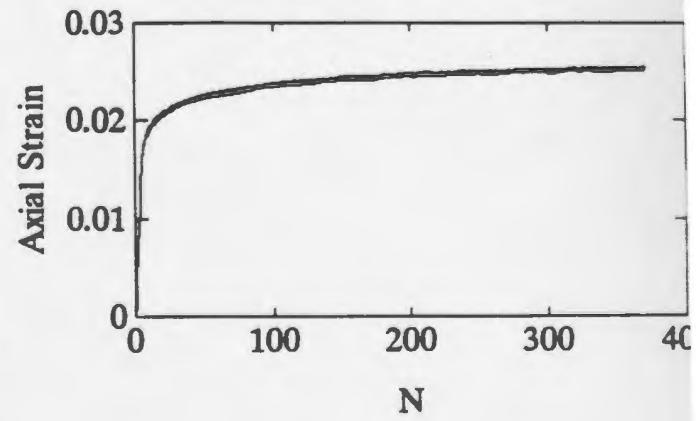
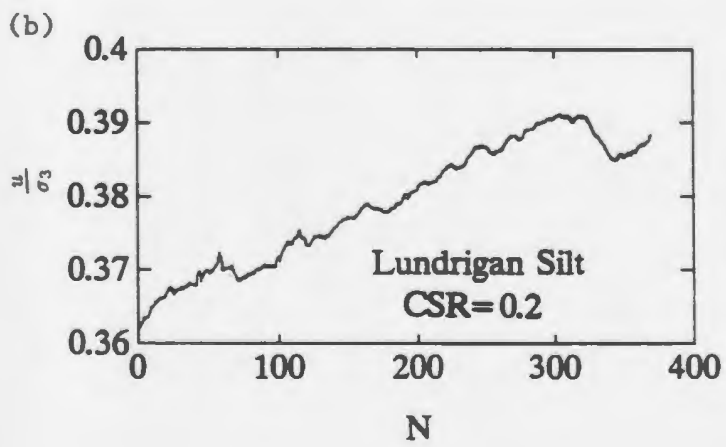
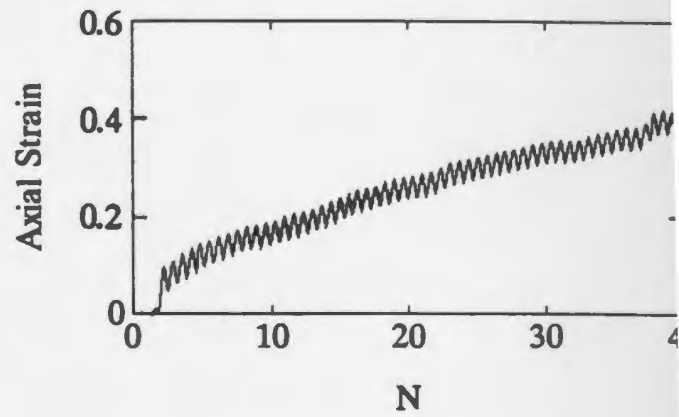
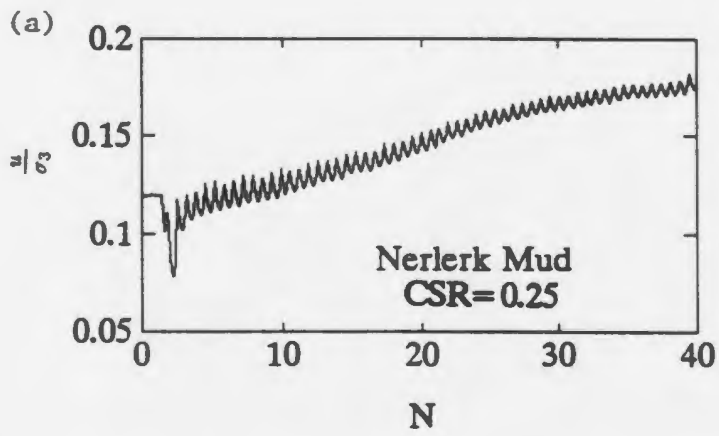


Figure 6.4: Typical Results for (a) Nerlerk Mud and (b) Lundrigan Silt.

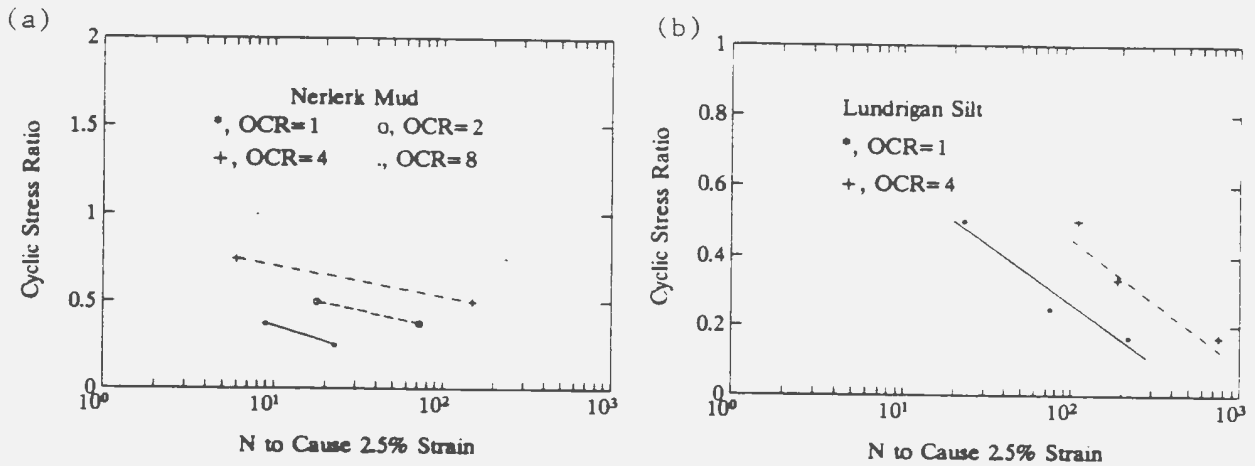


Figure 6.5: Effect of OCR on (a) Nerlerk Mud and (b) Lundrigan Silt.

6.4.2 Effect of Mean Particle Size

The CSR has been plotted in Figure 6.6 against the mean particle size, D_{50} , of the specimens. This figure shows that the strength increased as the mean particle size decreased to a certain extent and Lundrigan Silt had higher cyclic strength than Nerlerk Mud and the Nerlerk sands. The lower cyclic strength in Nerlerk Mud may be due to the high water content in the seafloor mud which could result in large deformations.

6.5 Stress-Strain Relationship

Typical curves for cyclic deviatoric stress vs axial strain (only for an initial limited number of cycles for each type of soil) are shown in Figure 6.7. In the specimens where positive pore pressure developed with increasing number of cycles, the backbone curve of the stress-strain relationship decreased gradually. In the specimens

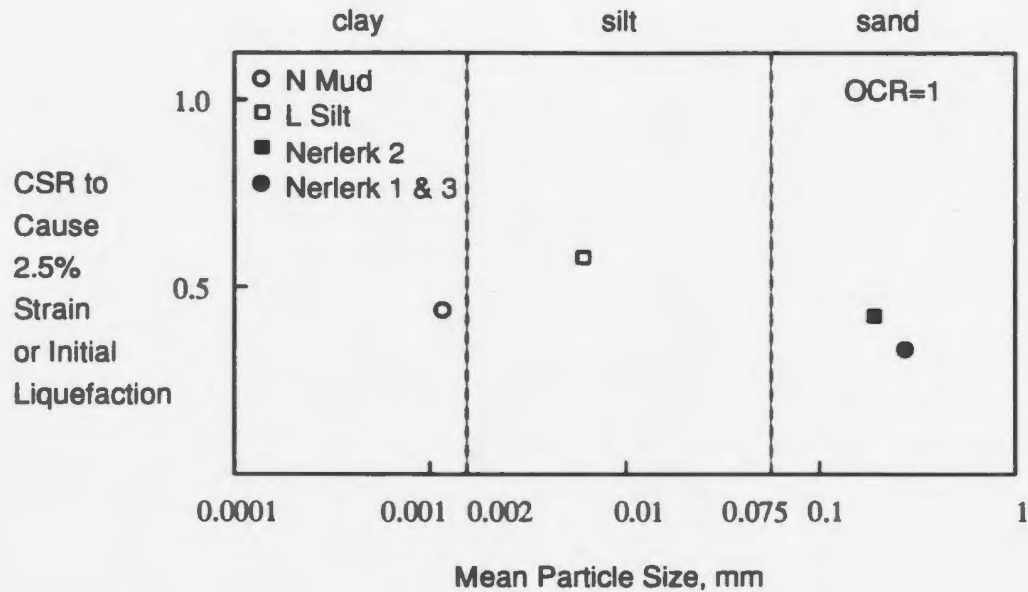


Figure 6.6: Effect of D_{50} .

such as dense Nerlerk #2 sand where positive pore pressure decreased after an initial increase as shown in Figure 6.3, the backbone curve increased (see Figure 6.7(b)). From these plots, greater deformation was measured for Nerlerk Mud than the rest of the soils for a given number of cycles as is shown in Figure 6.7. These curves of the cyclic stress-strain relationship can be used to determine shear moduli as discussed in Chapter 7.

6.6 Liquefaction Potential

Plots of CSR vs N to cause initial liquefaction in all the Nerlerk sands are presented in Figure 6.8(a). These test results indicate that Nerlerk #2 sand has a somewhat higher liquefaction resistance than Nerlerk #1 and #3 sands. This is interpreted to be caused by the fine grain fraction present in Nerlerk #2 sand preventing buildup of excess pore water pressure (see Figure 4.1).

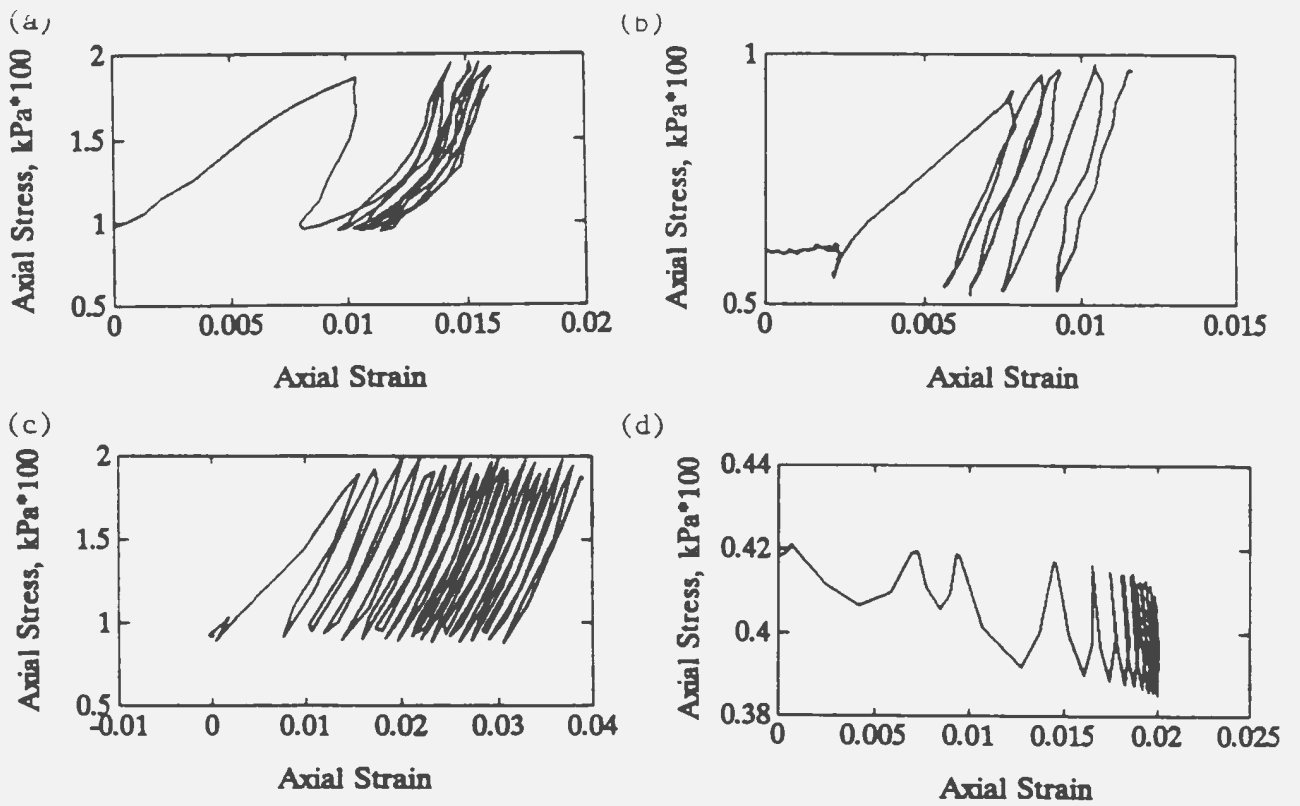


Figure 6.7: Stress-Strain Relationship for (a) Medium Dense Nerlerk #2 Sand, (b) Dense Nerlerk #2 Sand, (c) Nerlerk Mud, and (d) Lundrigan Silt.

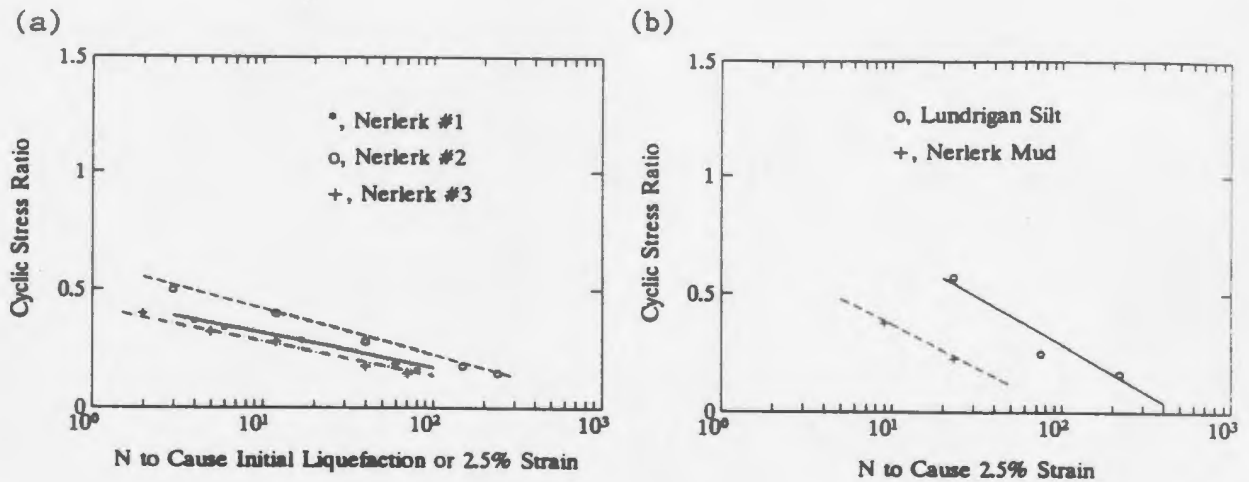


Figure 6.8: (a) Liquefaction Potential for Nerlerk Sands and (b) CSR vs N to Failure for Lundrigan Silt and Nerlerk Mud.

6.7 Cyclic Strength

The cyclic strength of a soil can be determined from CSR vs N plots such as that shown in Figure 6.8(b). This plot shows that Lundrigan Silt would retain its strength for a greater number of cycles (given a certain CSR) as compared to Nerlerk Mud. This is attributed to the fact that the high water content present in Nerlerk Mud caused much larger deformations and the specimens failed from excessive deformations.

Theoretically, the maximum cyclic stress ratio that can be applied to a cohesionless specimen is a function of effective confining pressure σ'_3 and effective angle of internal friction ϕ' . According to static limit equilibrium, for isotropically consolidated,

$$\frac{\sigma_d}{2\sigma'_3} = \frac{\sin\phi'}{(1 - \sin\phi')} \quad (6.1)$$

In reality, however, the combined deviatoric stresses measured in soils may be larger than those obtained from the above equation. This is due to strain rate effects in cyclic tests that result from the short duration of load application during each cycle. Nevertheless, under these conditions, failure in cyclic tests is imminent and the failure envelope from static tests may still provide an adequate reference strength.

Chapter 7

Stability Threshold and Dynamic Stiffness of Saturated Clays

A common approach in geotechnical earthquake engineering is to express the undrained resistance as a function of the number of load cycles to failure. However, when the number of load cycles is very large and they are applied over a long period of time, as in the case of wave loading, it is more convenient to express the cyclic undrained resistance of clayey soils as a threshold. This threshold (i.e., stability threshold) is defined as the stress level below which the soil will not fail regardless of the number of applied cycles.

An understanding of the dynamic stiffness of marine soils is also required in the analysis of offshore structures subjected to earthquake excitation or storm wave action. This behavior is commonly expressed in terms of a modulus degradation of the soil with an increase in strain.

The objective of this experimental investigation was to quantify the stability threshold and dynamic modulus of saturated Beaufort Sea clays at various over-consolidation ratios.

7.1 Stability Threshold

A compilation of published data on the stability threshold of clayey soils is presented in Table 7.1. This list is restricted to data obtained from one-way cyclic triaxial test results (which is the method used in the present experimental program), as it

is known that test type and loading conditions can influence the results.

This chapter presents the results of a laboratory testing program on the Beaufort Sea clayey soils aimed at studying the stability threshold problem. Stability thresholds were determined for both overconsolidated and normally consolidated specimens at a predetermined frequency.

7.1.1 Test Procedures

All tests were conducted on isotropically consolidated specimens subjected to undrained conditions. An all-around consolidation pressure, σ_c , higher than the apparent preconsolidation pressure, σ'_p , was used for tests requiring normally consolidated specimens. An all-around consolidation pressure lower than the apparent preconsolidation pressure was used for tests requiring overconsolidated clay specimens. Cyclic triaxial tests were performed under load-controlled conditions with a loading frequency of 1 Hz which is the commonly used frequency in the dynamic design of offshore structures. Deviator stress, σ_d , was alternated between zero and a pre-selected maximum value (i.e., one-way cyclic load). The values of deviatoric stress, σ_d , and confining pressure, σ_3 were recorded by a data acquisition system during testing.

The soil samples investigated in this study were Nerlerk Mud, Shelf Silty Clay, Shelf Clay, Marine Silt, and Beaufort Sea Clay. These soils were previously described in detail in Chapter 4.

7.1.2 Test Results

The typical development of normalized pore pressure, u/σ_c (or u/σ'_p for OC specimens), and axial strain, ϵ_a , with the number of loading cycles, N , is shown in Figure 7.1. The rest of the typical results for each type of soil are presented in Appendix B. Due to the limitations set on the length of the thesis, only two typical figures for each type of soil are presented in Appendix B.

The criterion for determining the stability threshold which was used in this portion of the study is as follows. It was noticed that as the cyclic stress ratio

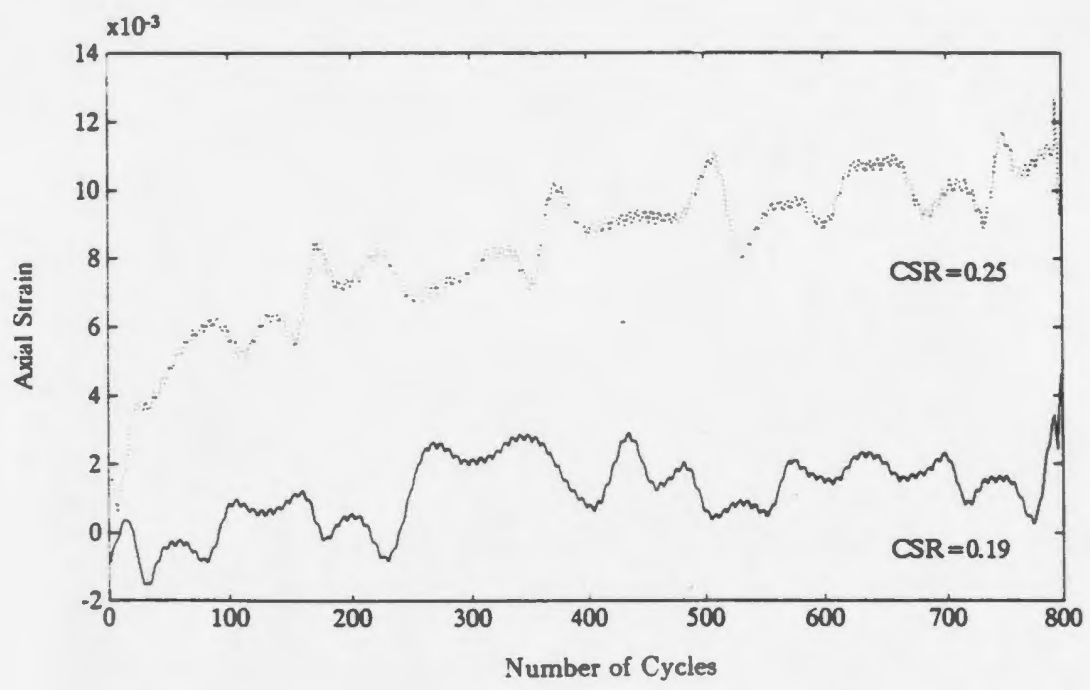
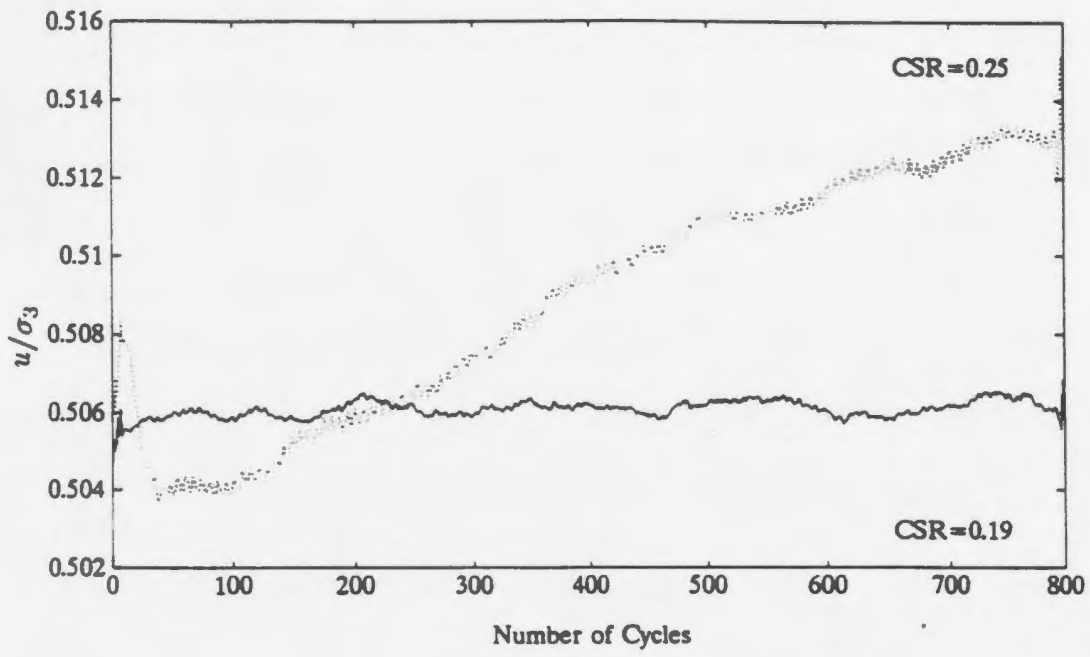


Figure 7.1: Test Results from Normally Consolidated Nerlerk Mud.

(CSR) was increased, the u/σ_c (or u/σ'_p) vs N plot or ϵ_a vs N plot changed from concave downward to concave upward as shown in Figure 7.1. This change in the shape of the curve to concave upward inferred that the soil would fail and was not "stable". The mean value of CSR of the first sample that was not stable and the CSR of "stable" sample was defined as the stability threshold. This criterion is essentially the same as the commonly used criterion, which states that the first CSR which would fail eventually is defined as the stability threshold (Houston and Herrmann, 1980; Lefebvre et al., 1989). Ideally, both methods require the CSR to be increased in small steps to determine the stability threshold. However, such a process would require many samples, and since a limited number of samples were available for the current study, the CSR was increased in relatively large steps.

Stability thresholds obtained from the tested samples are summarized in Table 7.2 through Table 7.6 for both normally consolidated and overconsolidated specimens.

Table 7.1: Published Data on Stability Thresholds, after Lefebvre et al., 1989
(including their data).

Soil	Reference	w %	w _L %	w _p %	I _p %	S _u	I _t	σ'_v kPa	Monotonic loading	Sampling technique	$(\sigma'_1 - \sigma'_3)$ kPa	Frequency Hz	Stability threshold
Casselman Clay	Raymond et al. (1977)	91	66	20	46	11 15	1.54	49	CID tests	Block	66	1	0.54
Ottawa Clay	Mitchell and King (1977)	33 38	34 41	18 20	-	15 25	-1	170 180	CIUC tests	Block	92 98	0.033 0.25	-0.5
Drammen Clay	Anderson et al. (1980)	52	55	28	27	-	0.89	NC	CIUC tests	Tube	110 (NC) 96 (OCR=4) 71 (OCR=10)	0.1	>0.68, <0.80 (NC) >0.52, <0.66 (OCR=4) >0.42, <0.68 (OCR=10)
Kaolinite	Hicher (1980)	-	-	-	-	-	-	NC	CIUC tests	Reconstituted	-	0.1	0.8
Bentonite	Hicher (1980)	-	-	-	-	-	-	NC	CIUC tests	Reconstituted	-	0.1	0.96
Pacific Hemi- pelagic Clay	Houston and Herrmann (1980)	69 118	51 68	20 32	-	<3	-	NC	CAUC tests	Box core	15	2	0.58
Keuper marl	Hyde and Ward (1985)	-	36	19	17	-	-	NC	CIUC tests	Reconstituted	-	0.1	0.50 (NC) 0.55 (OCR =4) 0.7 (OCR=10)
Pacific Pelagic Clay	Houston and Herrmann (1980)	81 128	85 101	-	42 74	<3	-	NC	CAUC tests	Piston Sampler	11-13	2	0.9
Atlantic calca- reous ooze	Houston and Herrmann (1980)	38	Nonplastic					NC	CAUC tests	Box core	48-62	2	0.18
San Francisco Bay mud	Houston and Herrmann (1980)	68	94	-	48	8	-	NC	CIUC tests	Piston Sampler	11-13	2	0.86
Grande Baleine Clay	Lefebvre and LeBoeuf (1989)	59	34	22	12	30	2.84	NC	CIUC tests	Block	40-60	0.01-2.0	0.19-0.28

Table 7.2: Stability Thresholds for Nerlerk Mud.

Type of Test	OCR	$\frac{(\sigma_1 - \sigma_3)_{max}}{2\sigma_3}$	Number of Cycles	Failure	ϵ_a	Approximate Stability Threshold $\frac{\epsilon_a}{2\sigma_3}$
<i>NM - CIUC_v - 8</i>	8.0	0.5 0.7	600 96	No Yes	0.95% 1.6%	0.6
<i>NM - CIUC_v - 4</i>	4.0	0.25 0.50	1000 120	No Yes	0.15% 1.9%	0.375
<i>NM - CIUC_v - 2</i>	2.0	0.25 0.375	700 120	No Yes	0.8% 3.4%	0.31
<i>NM - CIUC_v - 1</i>	1.0	0.19 0.25	500 120	No Yes	0.4% 3.8%	0.22

Table 7.3: Stability Thresholds for Marine Silt.

Type of Test	OCR	$\frac{(\sigma_1 - \sigma_3)_{max}}{2\sigma_3}$	Number of Cycles	Failure	ϵ_a	Approximate Stability Threshold $\frac{\epsilon_a}{2\sigma_3}$
<i>MS - CIUC_v - OC</i>	4	0.5 0.67	1000 120	No Yes	1.2% 2.5%	0.58
<i>MS - CIUC_v - OC</i>	2	0.33 0.5	700 120	No Yes	0.8% 2.0%	0.415
<i>MS - CIUC_v - NC</i>	1	0.167 0.33	600 120	No Yes	0.4% 1.1%	0.25

Table 7.4: Stability Thresholds for Shelf Clay.

Type of Test	OCR	$\frac{(\sigma_1 - \sigma_3)_{max}}{2\sigma_3}$	Number of Cycles	Failure	ϵ_a	Approximate Stability Threshold $\frac{\epsilon_a}{2\sigma_3}$
<i>SC - CIUC_v - OC</i>	2.0	0.25	1000	No	0.6%	0.375
		0.50	100	Yes	1.6%	
<i>SC - CIUC_v - NC</i>	1.0	0.125	900	No	0.7%	0.19
		0.25	120	Yes	2.8%	

Table 7.5: Stability Thresholds for Shelf Silty Clay.

Type of Test	OCR	$\frac{(\sigma_1 - \sigma_3)_{max}}{2\sigma_3}$	Number of Cycles	Failure	ϵ_a	Approximate Stability Threshold $\frac{\epsilon_a}{2\sigma_3}$
<i>SSC - CIUC_v - OC</i>	4.4	0.227	1000	No	1.8%	0.28
		0.34	110	Yes	3.8%	
<i>SSC - CIUC_v - OC</i>	2.2	0.17	1000	No	0.7%	0.2
		0.227	120	Yes	1.9%	
<i>SSC - CIUC_v - NC</i>	1.1	0.11	1000	No	0.6%	0.14
		0.17	120	Yes	2.3%	

Table 7.6: Stability Thresholds for Beaufort Sea Clay.

Type of Test	OCR	$\frac{(\sigma_1 - \sigma_3)_{max}}{2\sigma_3}$	Number of Cycles	Failure	ϵ_a	Approximate Stability Threshold $\frac{\sigma_a}{2\sigma_3}$
<i>BSC - CIUC_v - OC</i>	4	0.33	1000	No	0.9%	0.42
		0.5	340	Yes	1.3%	
<i>BSC - CIUC_v - OC</i>	2	0.125	1000	No	0.6%	0.2
		0.175	480	Yes	1.2%	
<i>BSC - CIUC_v - NC</i>	1	0.08	1000	No	0.6%	0.1
		0.116	225	Yes	1.6%	

The stability thresholds in the above five tables are shown in Figure 7.2.

7.1.3 Discussion

The results show that the Beaufort Sea soils exhibit very good normalized behavior with respect to consolidation stress, σ_c , or preconsolidation pressure, σ'_p .

The following conclusions can be made from the test results:

- In general, at low stress levels, the larger increases in pore pressure were generated during the first few loading cycles.
- For samples tested above the stability threshold, axial strain increased slowly with each loading cycle, but increased suddenly when the sample approached failure. When the CSR value was below the stability threshold, the axial strain increased slowly with each loading cycle but the samples did not fail.
- The maximum axial strain of the non-stabilized samples by the time the curve became concave upward (it was before failure for most samples) ranged

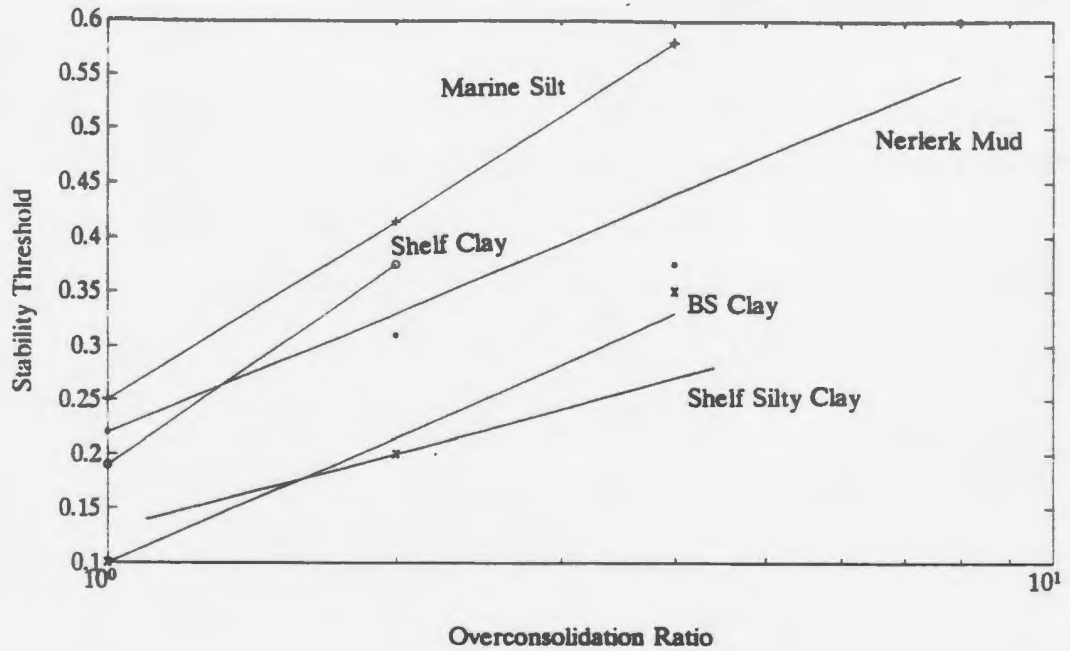


Figure 7.2: Stability Threshold versus Overconsolidation Ratio.

between 1.6% (Beaufort Sea Clay) and 3.8% (Nerlerk Mud) for normally consolidated soils, between 1.2% (Beaufort Sea Clay) and 3.4% (Nerlerk Mud) for slightly overconsolidated soils ($1 < OCR \leq 2$), and between 1.0% (Beaufort Sea Clay) and 2.4% (Marine Silt) for highly overconsolidated soils ($OCR \geq 3$). These results indicate that the maximum measured strain at failure in overconsolidated soils is less than that of normally consolidated soils.

- A survey of the maximum axial strains measured in the stabilized cyclic tests (those tests in which CSR was less than the stability threshold) shows that the maximum strain was less than 0.7% for normally consolidated soils (Shelf Clay), less than 0.8% for slightly overconsolidated soils (Nerlerk Mud), and less than 1.2% for highly overconsolidated soils (Shelf Clay) ($OCR \geq 3$). From this, it can be seen that the strain in the stabilized tests was much smaller than that in the non-stabilized tests as the specimens approached failure. In addition, strain should be smaller in highly overconsolidated specimens

than in slightly overconsolidated specimens or normally consolidated specimens in the above stabilized cyclic tests. These results were not observed in the stabilized samples for the following reasons. The first reason was that the deformation eventually stabilized, and the curves remained practically horizontal with additional loading cycles. Therefore, no essential difference existed whether the permanent strain was higher or lower. The second reason was that in the above stabilized tests, by chance, the CSR values chosen for the OC soils were closer to their thresholds than the CSR values chosen for the NC soils.

- The buildup of pore pressure was somewhat difficult to measure even in specimens where failure occurred, and it generally did not show a sudden increase before failure. The normalized pore pressure curves slowly increased even after a large number of cycles for normally consolidated and overconsolidated soils. This behavior is attributed to the high plasticity of the samples; in low plasticity soil (e.g., Marine Silt), pore pressure response was slightly higher.
- The higher the OCR, the higher the stability threshold. The more apparent effect of OCR was found in specimens of high plasticity such as Beaufort Sea Clay and Shelf Clay. From Table 7.2 through Table 7.6, the following statistical results can be obtained: the increment of CSR caused by OCR for those specimens of high plasticity (Shelf Clay and Beaufort Sea Clay) from OCR=1 to 4 ranged between 173 ~ 320%; for low and medium plasticity specimens such as Marine Silt, Shelf Silty Clay and Nerlerk Mud, the increment was between 100 ~ 132%. The expected more evident OCR effect did not occur in Nerlerk Mud probably due to the fine and medium sand components presented in this material. The sand particles reduced the plasticity of the Nerlerk Mud and weakened the OCR effect.
- In normally consolidated specimens, higher stability thresholds were found in Marine Silt and Nerlerk Mud. This is attributed to good grading in these two soils. In overconsolidated specimens, the higher stability thresholds were

found in high plasticity clayey soils such as the Beaufort Sea Clay and Shelf Clay. This can be attributed to the OCR effect described above. However, the stability thresholds appeared to be independent of either individual consolidation pressure or individual preconsolidation pressure. The stability threshold values of relatively well graded and medium plasticity Shelf Silty Clay fell between the values obtained for the above two soils.

- The average stability threshold for the clays was approximately 17.0% of σ_c for normally consolidated specimens, 29.5% of σ'_p for overconsolidated soils of OCR=2, and 39.8% of σ'_p for overconsolidated soils of OCR=4. For the silty clay, these values were approximately 14%, 20% and 28%, respectively and for the silt, approximately 25%, 41.5% and 58%, respectively. The OCR effect is shown in Figure 7.3. The figure indicates that the effect of an increase in OCR appears to be the same for all three types of soil.

7.1.4 Comparison with Other Results

A comparison of the stability thresholds for the clays obtained from this group of experiments with the results for Grande Baleine clay from Hudson Bay in north-western Quebec (Lefebvre et al., 1989), indicates that the stability thresholds of the different types of the Beaufort Sea clays are lower than those reported by Lefebvre et al. (1989) whether the clays are normally consolidated or overconsolidated. The reason for this could be that the marine clays tested in this research had higher water contents and the slight disturbance in some samples like the Nerlerk Mud due to long-distance transport and long duration of storage degraded the clay structure. Also, the difference in test results could be due to the shape of the particles and mineralogy.

7.2 Dynamic Young's Modulus

Clay stiffness during cyclic loading can be expressed using an undrained secant modulus, such as dynamic Young's modulus, E_d , and dynamic shear modulus, G_d .

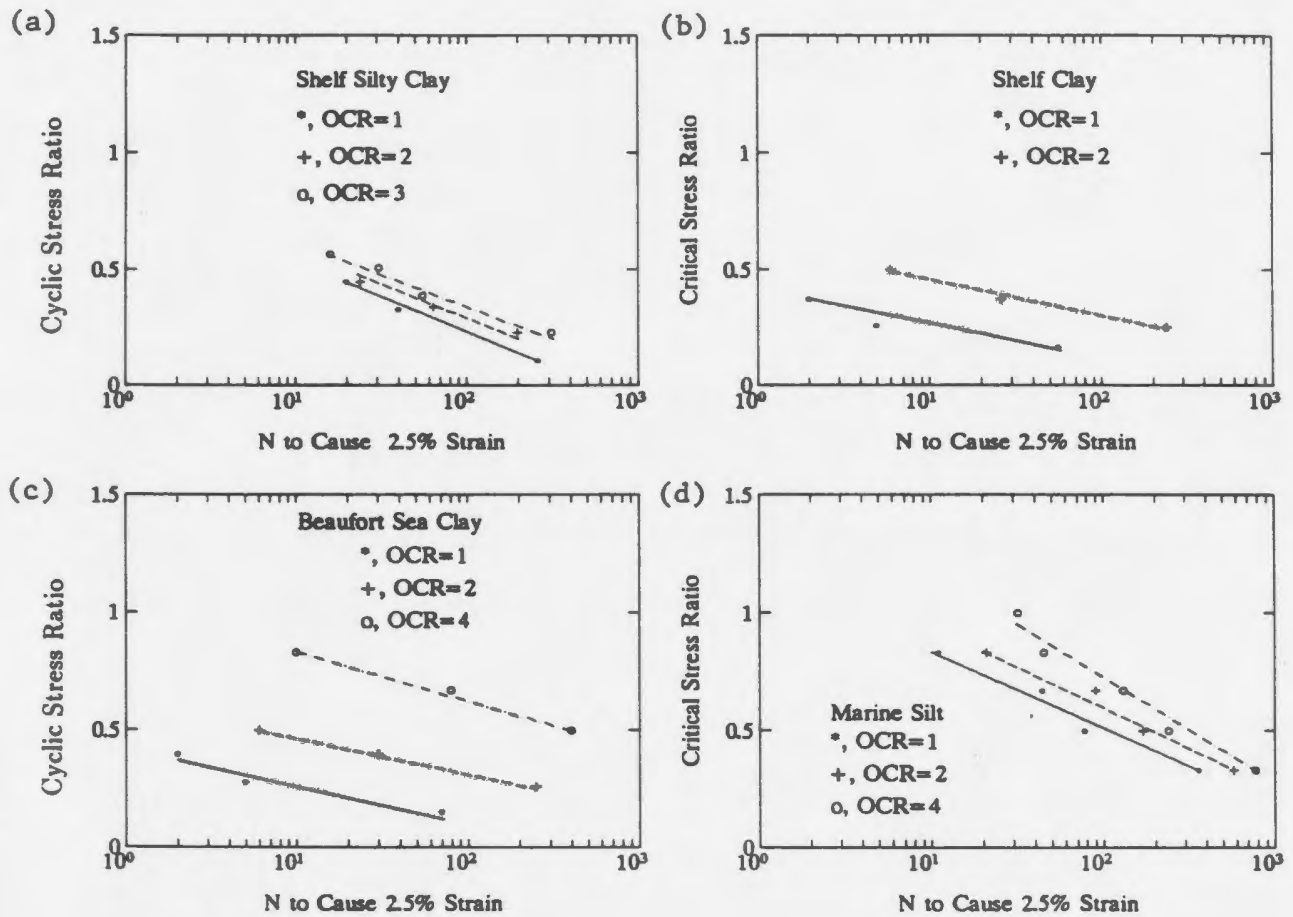


Figure 7.3: Effect of Overconsolidation Ratio.

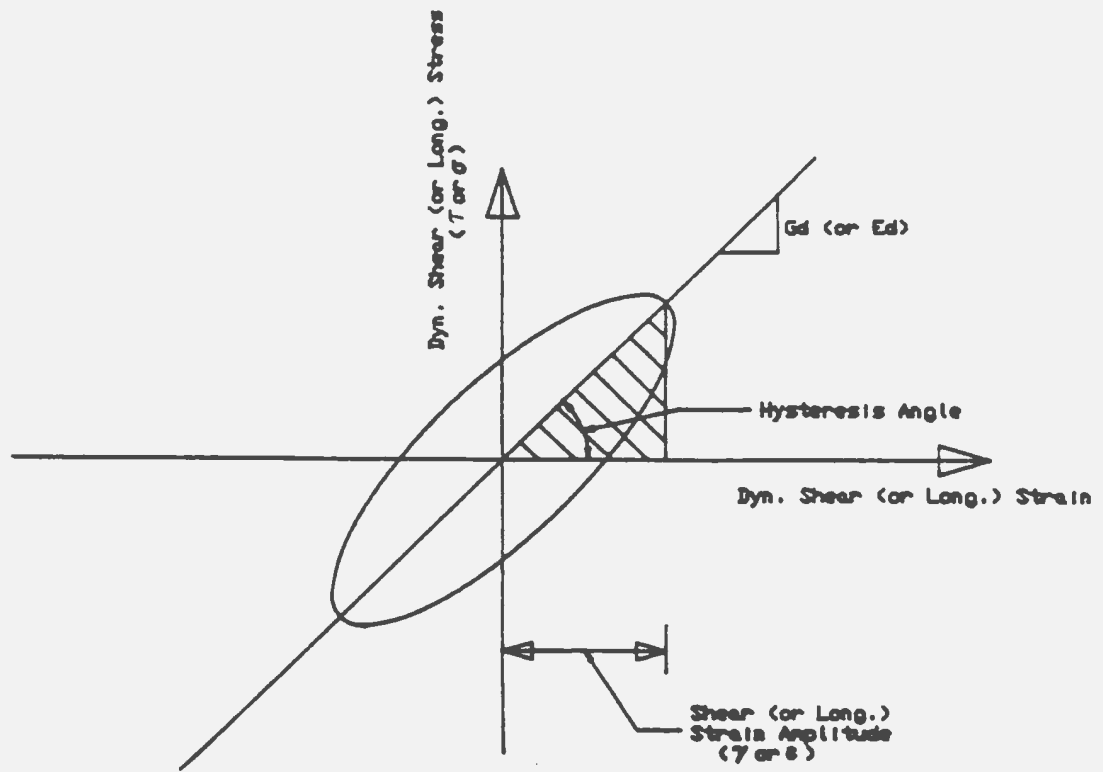


Figure 7.4: The Definition of Moduli.

The definition of these two moduli are shown in Figure 7.4 for cyclic triaxial tests.

The relation between longitudinal strain (or axial strain) and shear strain is

$$\gamma_d = (1 + \nu)\epsilon_d \quad (7.1)$$

where

γ_d is the dynamic shear strain,

ϵ_d is the dynamic longitudinal strain, and

ν is the Poisson's ratio (for undrained samples, $\nu = 0.5$).

Hence, the dynamic shear modulus can be expressed as

$$G_d = \frac{\tau_d}{\gamma_d} = \frac{\sigma_d}{2(1 + \nu)\epsilon_d} = \frac{E_d}{2(1 + \nu)} \quad (7.2)$$

where

τ_d is the dynamic shear stress, and

σ_d is the dynamic deviatoric stress ($\tau_d = \frac{1}{2}\sigma_d$).

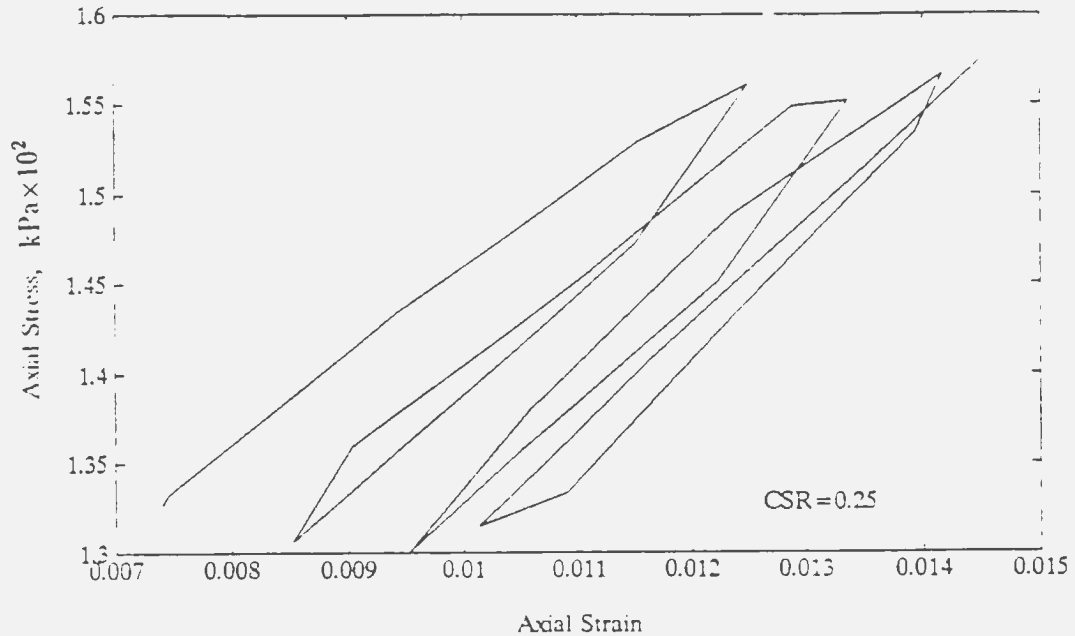


Figure 7.5: Stress-Strain Relationship for Normally Consolidated Shelf Clay.

7.2.1 Test Results

Figure 7.5 shows a typical curve of the corresponding cyclic stress - strain relationship obtained from the normally consolidated Shelf Clay. Figure 7.6 - Figure 7.9 show the dynamic Young's modulus, E_d , vs ϵ_a curves for the Beaufort Sea Soils.

7.2.2 Discussion

For all soils, the cyclic stress-strain hysteresis loops were normally not closed. This indicates that the hysteresis angle (see Figure 7.4) for each loading cycle was not constant. This was due to plastic flow in the soil. Therefore, the soil can not be described simply as a mass-damping-spring system. It can be concluded that the elastic and damping parameters for the system are not constant. The response shown in Figure 7.4 corresponds to an ideal visco-elastic soil only.

In Figure 7.6 - Figure 7.9, it is seen that the dynamic Young's Modulus decreased with an increase in axial strain for all types of soil and for all OCR's. The

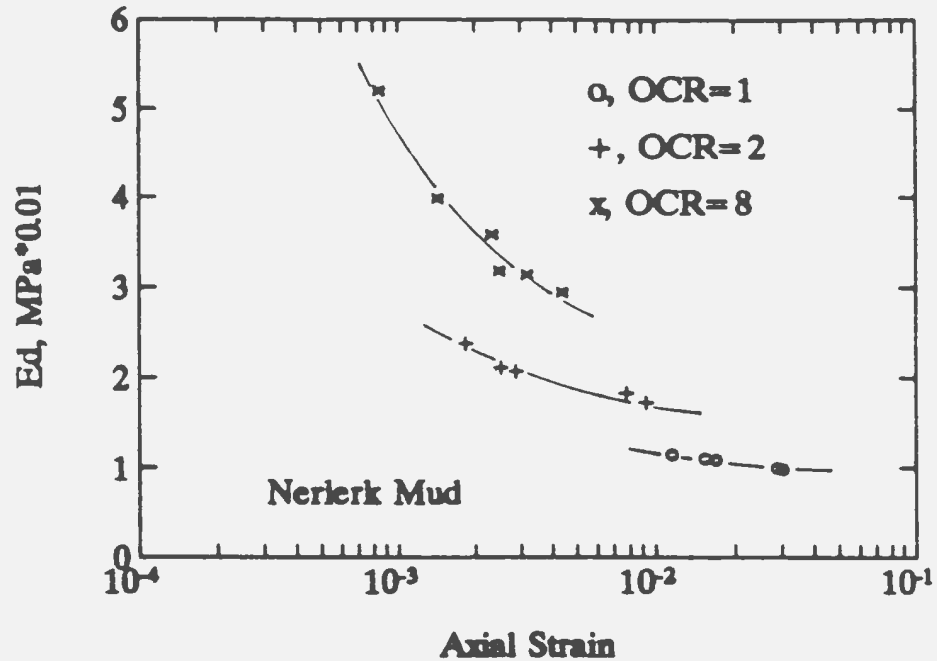


Figure 7.6: Dynamic Young's Modulus vs Axial Strain for Nerlerk Mud.

effect of overconsolidation ratio was pronounced in all types of soil. Therefore, overconsolidation ratio must be considered an important factor in the dynamic design of offshore structures. In most cases, the magnitude of change in dynamic Young's modulus for OC soils decreased with an increase in axial strain faster than for NC soils during the range of large strain (see Figures 7.5, 7.6 and 7.7). This indicates that large strains in the soil weakened the effect of OCR.

An interesting observation can be made from these figures. For cohesionless soil (Marine Silt), E_d/σ_c (or E_d/σ'_p) vs ϵ_a curves are concave downward; for cohesive soils (Beaufort Sea Clay and Nerlerk Mud), the curves are concave upward; while for silty clay (Shelf Silty Clay), the curves are a combination: OC state is downward and NC state is upward. It is known from previous work (Skotheim et al., 1985) that E_d/σ_c (or E_d/σ'_p) vs ϵ_a curves are eventually concave upward as shown in Figure 2.7. Marine Silt did not reach a final concave upward state because of higher bearing strength as compared to clays and silty clays. Similarly, the phenomenon

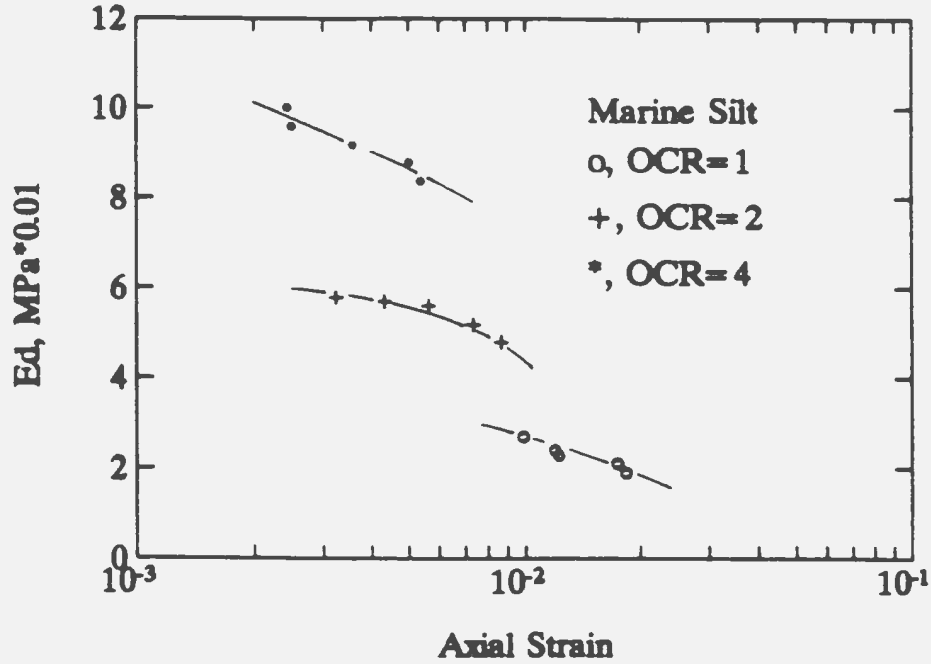


Figure 7.7: Dynamic Young's Modulus vs Axial Strain for Marine Silt.

in Shelf Silty Clay could be interpreted as higher strength in its OC state than its NC state.

It is known that dynamic moduli obtained from cyclic triaxial tests correspond to large strains, and those obtained from resonant column tests correspond to small strains. If small strain moduli had been obtained in this study, the complete curves similar to Figure 2.7 would have resulted. The expression for these curves is given by (see Eq. 2.6):

$$\frac{G_d}{G_{max}} = \frac{1}{1 + \frac{\gamma_d}{\gamma_r}} \quad (7.3)$$

where

G_{max} is the maximum shear modulus and corresponds to a shear modulus for a very low strain range, and

γ_r is the reference strain, $\gamma_r = \tau_{max}/G_{max}$.

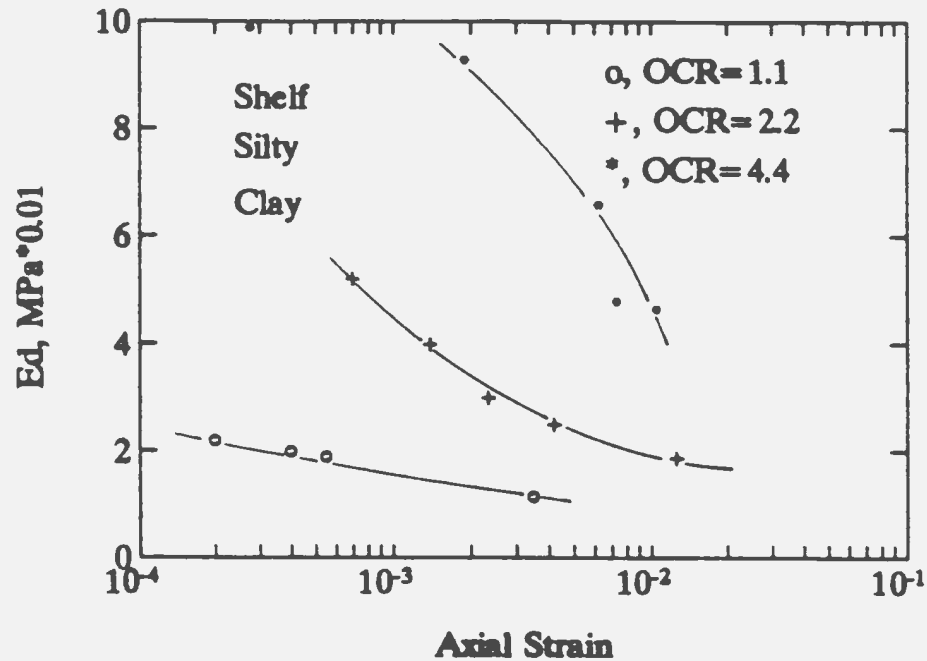


Figure 7.8: Dynamic Young's Modulus vs Axial Strain for Shelf Silty Clay.

Because of the limitation of the experimental setup and the limited number of samples, the overall trend of the stress - strain relationship shown in Figure 2.7 could not be obtained.

Figure 7.5 shows that the slope of the stress - strain curve decreases with the number of loading cycles, N (one hysteresis loop represents one cycle). This indicates that the dynamic Young's modulus of the soils degraded with the number of cycles, N .

Cyclic modulus degradation can be evaluated by a degradation index, δ , defined as the ratio of G in cycle N (G_N) to G in the first cycle (G_1). It has been empirically found that the effect of degradation in clay accumulates with the increase of cyclic straining and δ decreases monotonically with N , such that δ versus N for NC and OC clays plots as a straight line in a log-log scale. The degradation index δ can be therefore determined as (Vucetic and Dobry, 1988)

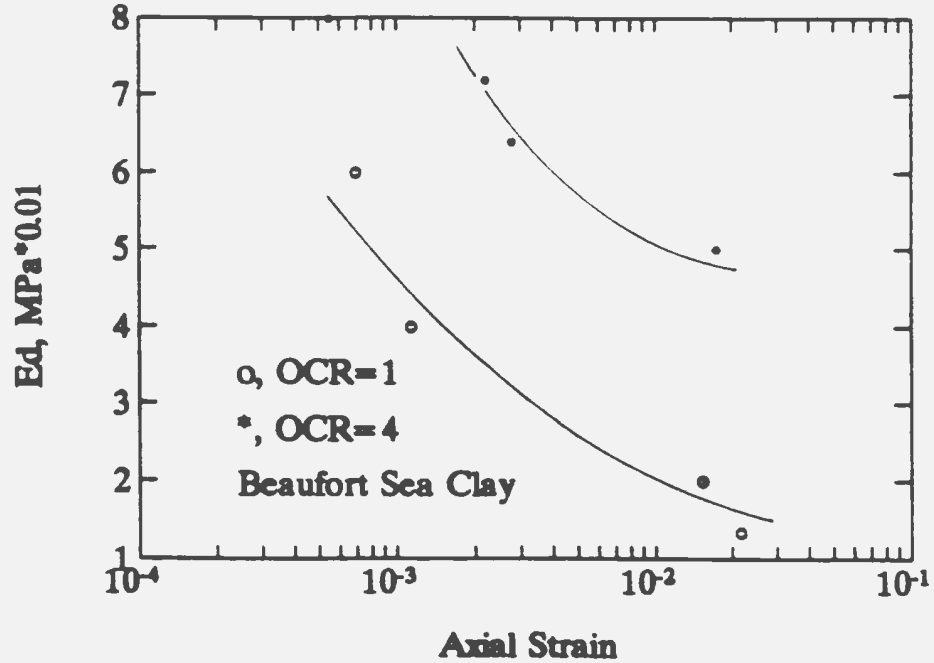


Figure 7.9: Dynamic Young's Modulus vs Axial Strain for Beaufort Sea Clay.

$$\delta = N^{-t} \quad (7.4)$$

where t is the negative slope of the δ vs N line, measuring the rate of change of δ . It is called the degradation parameter.

In a strain-controlled test, t can be obtained directly from $\log(\delta)$ vs $\log(N)$ curves or from the relationship:

$$t = -\frac{\log \delta}{\log N}. \quad (7.5)$$

In a stress-controlled test, the method to obtain t is more complex. Normally, the following method is adopted. A family of G_d vs N curves are plotted in a log-log scale. The points on different curves where the same shear strain, γ_d , can be found are then joined. Consequently, a family of straight γ_d contour lines can be obtained. The slope of each line is the degradation parameter corresponding to that γ_d value.

Since the author did not have enough samples of undisturbed Beaufort Sea soil, the data obtained from the load-controlled tests were not sufficient to determine a reliable modulus degradation index, δ .

Chapter 8

Conclusions

8.1 Deformation under Long Term Cyclic Loading

The results from a long term cyclic loading triaxial test program were compared to a variety of rheological models. The experimental results and numerical analysis show that close correspondence of strain path and final strain can be achieved through the input of proper parameters. This indicates that for one-dimensional loading, a theoretical treatment of the mechanical process is feasible.

On the basis of the analyses of test and theoretical results obtained from this portion of the study, the following conclusions can be drawn for deformation characteristics and predictions of seafloor sediment deformation under long term cyclic loadings:

- A number of different rheological soil models were tested, and, after back-analysis, good agreement was found between theoretical and experimental results.
- Due to these promising results from the theoretical analyses, this one-dimensional study should be further developed for use in engineering applications, and
- Rheological analysis of cyclic loaded soils may supplement other techniques as a means of predicting long term deformations under cyclic loading.

8.2 Liquefaction Potential and Cyclic Strength

The following conclusions can be made from the liquefaction and cyclic strength experimental program:

- A general increase of normalized cyclic resistance (i.e., CSR for a given number of cycles) with increasing plasticity was observed during testing (i.e. the effect of mean particle size). It is known that clay is less susceptible to densification by vibration than sands. However, it seems likely that cyclic resistance depends on other factors in addition to the plasticity.
- A heavily overconsolidated clay is in a dilative state. The overconsolidated clay would be expected to have relatively high cyclic strength and would therefore generate very little positive pore pressure during cyclic loading. When clays, which are composed of many aggregates of clay particles and condensed salt molecules like marine soils, become overconsolidated, the effective surface area for adsorption of pore water is increased.
- The effect of drainage on cyclic strength (i.e., the increase of liquefaction resistance or cyclic strength with the improvement of drainage conditions) should be considered in the light of the data presented herein. However, determination of the effect of drainage for a particular application would have to be studied further on a site-specific basis according to the drainage conditions, the thickness of the soil layer, the type of soil and the particular engineering requirement for the site. Also, an effective stress approach must be taken if partial drainage conditions are to be taken into account.

8.3 Stability Threshold and Cyclic Modulus

The following conclusions can be made from the stability threshold and cyclic modulus experimental program:

- Axial strain increased slowly at the beginning of testing, but increased suddenly when the sample approached failure. While the pore water pressure buildup

was somewhat difficult to measure even in specimens where failure occurred, it generally did not show a sudden increase before failure.

- The maximum measured strain of the non-stabilized samples at failure in overconsolidated soils was less than that of normally consolidated soils. The higher the OCR, the higher the stability threshold. An increase with OCR appeared to be the same for all types of soil.
- For normally consolidated specimens, higher stability thresholds were found in Marine Silt and in Nerlerk Mud. For overconsolidated specimens, the higher stability thresholds were found in high plasticity clayey soils such as the Beaufort Sea Clay and Shelf Clay. The stability threshold values of relatively well graded and medium plasticity Shelf Silty Clay fell between the values of the above two types of soil.
- The open-ended stress-strain hysteresis loops indicate that the soil can not be described simply as a mass-damping-spring system since the elastic parameter and damping parameter for the system were not constant. The OCR effect of silty and clayey marine soils was pronounced. However, large strains in soil weakened the effect. The OC state of a soil had a higher modulus than its NC state.
- In general, the dynamic moduli of the silt and clays degraded with the number of cycles. The test results indicate that Marine Silt had a higher modulus than Shelf Silty Clay, and Shelf Silty Clay had a higher modulus than Beaufort Sea Clay and Nerlerk Mud. In other words, Marine Silt had the highest bearing strength among these samples. This is attributed to the relatively low plastic index and the relatively low water content of Marine Silt.

Chapter 9

References

Andersen, K. H., Phukunhaphan, A., Douglas, B.J., and Martin, G.R., 1983. *Cyclic Behavior of Six Marine Clays*, Proc., Session No. 52, 1983 ASCE Annual Convention, Houston, Texas, pp. 17-21.

Annaki, M. and Lee, K. L., 1976. *Equivalent Uniform Cycle Concept for Soil Dynamics Liquefaction Problems in Geotechnical Engineering*, ASCE, Preprint 2752, Philadelphia, Pa., September.

Berre, T., 1981. *Triaxial Testing at the Norwegian Geotechnical Institute*, NGI, Publication NR. 134, Oslo, pp. 1-17.

Castro, G., and Poulos, S. J., 1977. *Factors Affecting Liquefaction and Cyclic Mobility*, J. Geot. Engg. Div., ASCE, Vol. 103, pp. 501-516.

Conn, G. M., and Hyde, A. F. L., 1986. *Critical Level of Repeated Loading for a Silty Clay*, Proc., 3rd Canadian Conference on Marine Geotechnical Engineering, St. John's, Nfld., vol. 2, pp. 691-705.

Cullingford, G., Lashine, A. K. F., and Paar, G. B., 1972. *Servo Controlled Equipment for Dynamic Triaxial Testing of Soils*, Geotechnique, Vol. 22, No. 3, pp. 526-599.

Das, B. M., 1983. *Fundamentals of Soil Dynamics*, Elsevier Science Publishers B. V., 399p.

Dobry, R., and Vucetic, M., 1987. *State-of-the-art Report: Dynamic Properties and Response of Soft Clay Deposits*, Proc., Int. Symp. on Geot. Engg. of Soft Soils, Vol. 2, pp. 51-87.

Eide, O., Anderson, K. H., and Lunne, T., 1979. *Observed Foundation Behavior of Concrete Gravity Platforms Installed in the North Sea, 1973-1978*, Paper No. 78, 2nd Int. Conf. Behavior of Offshore Structures, London, pp. 435-456.

Ferry, J. D., 1980. *Viscoelastic Properties of Polymers*, John Wiley & Sons, Inc, New York, 641p.

Foott, R., and Ladd, C. C., 1981. *Undrained Settlement of Plastic and Organic Clays*, J. Geot. Engg. Div., ASCE, Vol. 107, No. GT8, Aug., pp. 1079-1094.

Geological Survey of Canada, 1990. *GSC Open File Report 2408*.

Golder Associates, 1989. *Report to Gulf Canada Resources Ltd.-Laboratory Testing of Nerlerk Sand and Clay Samples*, Calgary, June.

Grainger, G. D., and Lister, N. W., 1962. *A Laboratory Apparatus for Studying the Behavior of Soils under Repeated Loading*, Geotechnique, Vol. 12, No. 1, pp. 3-14.

Hardin, B. O., and Drnevich, 1972. *Shear Modulus and Damping in Soils: Design Equations and Curves*, J. Soil Mech. and Fdn. Engg. Div., ASCE, Vol. 98, No. SM7, pp. 667-692.

Herrmann, H. G., and Houston, W. N., 1978. *Behavior of Seafloor Soils subjected to Cyclic Loading*, Proc., 10th Offshore Technology Conference, Houston, Texas, May.

Herrmann, H. G., and Houston, W. N., 1976. *Response of Seafloor Soil to Combined Static and Cyclic Loading*, Proc., 8th Offshore Technology Conference Houston, Texas, May.

Houston, W. N., and Herrmann, H. G., 1980. *Undrained Cyclic Strength of Marine Soils*, J. Geot. Engg. Div., ASCE, Vol. 106, No. GT6, June, pp. 691-712.

Idriss, I. M, Dobry, R., and Singh, R. D., 1978. *Nonlinear Behavior of Soft Clays during Cyclic Loading*, J. Geot. Engg. Div., ASCE, Vol. 104, No. GT12, Dec., pp. 1427-1447.

Idriss, I. M, Moriwaki, Y., Wright, S. G., and Doyle, E. H., 1980. *Behavior of Normally Consolidated Clay under Simulated Earthquake and Ocean Wave Loading Conditions*, Proc., International Symposium on Soils under Cyclic and Transient Loading, Vol. 1, A. A. Balkema, Rotterdam, the Netherland, Jan., pp. 437-445.

Ishihara, K., Sodekawa, M., and Tanaka, Y., 1978. *Effects of Overconsolidation on Liquefaction Characteristics of Sands Containing Fines*, Dynamic Geotechnical Testing, ASTM STP 654, American Society for Testing and Materials, pp. 246-264.

Jefferies, M. G., 1988. *Independence of Geostatic Stress from Overconsolidation in Some Beaufort Sea Clays, Reply*, Canadian Geotechnical Journal, Vol. 25, pp. 624-630.

Jefferies, M. G., 1987. *Independence of Geostatic Stress from Overconsolidation in Some Beaufort Sea Clays*, Canadian Geotechnical Journal, Vol. 24, pp. 342-256.

- Jefferies, M. G., Ruffel, J. P., Crooks, J. H. A., and Hughes, J. M. O., 1985. *Some Aspects of the Behavior of Beaufort Sea Clays*, Strength Testing of Marine Sediments and In-situ Measurements, ASTM STP 883 Philadelphia, pp. 487-514.
- Khan, Z. A., 1985. *Triaxial Testing on Soils from Newfoundland Areas: Results of Monotonic and Cyclic Tests*, M.Eng. Thesis, Memorial University of Newfoundland, St. John's.
- Klementev, I., 1983. *Simple Cyclic Loading in Soil Mechanics*, Geotechnique, Vol. 33, No. 3, pp. 344-347.
- Konrad, J.-M., 1985. *Undrained Cyclic Behavior of Beaufort Sea Silt*, Arctic Offshore Engineering, pp. 830-837.
- Koutsoftas, D. C., and Fischer, J. A., 1980. *Dynamic Properties of Two Marine Clays*, J. Geot. Engg. Div., ASCE, Vol. 106, No. 6, pp. 645-657.
- Koutsoftas, D. C., and Ladd, C. C., 1985. *Design Strength for an Offshore Clay*, J. Geot. Engg. Div., ASCE, Vol. 111, No. GT3, March, pp. 753-786.
- Kurfurst, P., 1984. *Geotechnical Investigations in the Southern Beaufort Sea*, Geological Survey of Canada, Open File Report 1078, June.
- Ladd, C. C., and Foott, R., 1974. *New Design Procedure for Stability of Soft Clays*, J. Geot. Engg. Div., ASCE, Vol. 100, No. GT7, July, pp. 763-786.
- Ladd, C. C., Foott, R., Ishihara, K., Schlosser, F., and Poulos, H. G., 1977. *Stress-Deformation and Strength Characteristics*, State of the Art Report, Session I, IX ICSMFE, Tokyo, Vol. 2, pp. 421-494.

- Ladd, C. C., Weaver, J. S., Germaine, J. T., and Sauls, D. P., 1985. *Strength-Deformation Properties of Arctic Silt*, Arctic Offshore Engineering, pp. 820-829.
- Ladd, R. S., 1976. Lecture Notes-Short Course, *Quality Geotechnical Laboratory Testing-Cyclic Behavior of Sand as Determined in the Laboratory for Earthquake Analysis*, University of Missouri, Rolla, May.
- Lee, K. L., 1979. *Cyclic Strength of a Sensitive Clay of Eastern Canada*, Can. Geot. J., Vol. 16, pp. 165-185.
- Lee, K. L., and Fitton, J. A., 1969. *Factors Affecting the Cyclic Loading Strength of Soil*, in *Vibration Effects of Earthquakes on Soils and Foundations*, ASTM STP 450.
- Lee, K. L., and Focht, J. A., Jr., 1975. *Liquefaction Potential at Ekofisk Tank in North Sea*, Journal of Geotechnical Engineering, ASCE, Vol. 101, No. GT1, Jan., pp. 1-18.
- Lee, K. L., and Seed, H. B., 1966. *Strength of Anisotropically Consolidated Samples of Saturated Sand Under Pulsating Loading Conditions*, Report No. TE-66-3, Department of Civil Engineering, University of California, Berkeley, July.
- Lefebvre, G. D., and LeBoeuf, D., 1987. *Rate Effects and Cyclic Loading of Sensitive Clays*, J. Geot. Engg. Div., ASCE, Vol. 113, pp. 476-489.
- Lefebvre, G. D., LeBoeuf, D., and Demers, B., 1989. *Stability Threshold for Cyclic Loading of Saturated Clay*, Can. Geot. J., Vol. 26, pp. 122-131.
- Lockett, F. J., 1972. *Nonlinear Viscoelastic Solids*, Academic Press, New York, 195p.

Lodde, P. F., and Stokoe, K. H., II, 1982. *Dynamic Response of San Francisco Bay Mud*, Geot. Engg. Report GT-82-2, University of Texas at Austin, Texas.

McCarron, W. O., and Been, K., 1990. *Response of a Beaufort Sea Clay to Monotonic and Cyclic Loading*, Vol. 4, OMAE '90, Proc., 9th Houston, Texas, pp. 329-336.

Meyerhof, G. G. 1979. *Geotechnical Properties of Offshore Soils*, 1st Canadian Conf. on Marine Geot. Engg, Calgary, Alberta, pp. 253-260.

Mitchell, J. K., Chatoian, J.M., and Carpenter, G. C., 1976. *The Influences of Sand Fabric on Liquefaction Behavior*, WES CR S-76-5, U.S. Army Engineer Waterways Experiment Station, Corps of Engineers, Vicksburg, Miss., June.

Moran, K., Hill, P. R., and Blasco, S. M., 1989. *Interpretation of Piezocone Penetrometer Profiles in Sediment from the Mackenzie Trough, Canadian Beaufort Sea*. J. of Sedimentary Petrology, Vol. 59, pp. 88-97.

Mulilis, J. P., 1975. *The Effects of Method of Sample Preparation on the Cyclic Stress-Strain Behavior of Sands*, EERC Report 75-18, College of Engineering, University of California, Berkeley, July.

Mulilis, J. P., Seed, H. B., Chan, C. K., Mitchell, J. K., and Arulanandan, K.. 1977. *Effects of Sample Preparation on Sand Liquefaction*, Journal of Geotechnical Engineering Division, ASCE, Vol. 103, No. GT2, Feb., pp. 91-108.

Mulilis, J. P., Townsend, F. C., and Horz, R. C., 1978. *Triaxial Testing Techniques and Sand Liquefaction*, Dynamic Geotechnical Testing, ASTM STP 654, pp. 265-279.

Pamukcu, S., and Suhayda, J. N., 1985. *Evaluation of Shear Modulus for Soft Marine Clays, Mississippi Delta*, Strength Testing of Marine Sediments: Laboratory and In-Situ Measurements, ASTM STP 883, American Society for Testing and Materials, Philadelphia, pp. 352-362.

Procter, D. C., and Khaffaf, J. H., 1984. *Cyclic Triaxial Tests on Remoulded Clays*, J. Geot. Engg. Div., ASCE, Vol. 110, No. GT10, Oct., pp. 1431-1445.

Saxena, S. K., Avramidis, A.S., and Reddy, K. R., 1988. *Dynamic Moduli and Damping Ratios for Cemented Sands at Low Strains*, Can. Geot. J., Vol. 25, pp. 353-368.

Scott, R. F., 1985. *Plasticity and Constitutive Relations in Soil Mechanics*, J. Geot. Engg., ASCE, Vol. 111, pp. 563-605.

Seed, H. B., and Idriss, I. M., 1971. *A Simplified Procedure for Evaluating Soil Liquefaction Potential*, J. Soil Mech. and Fdn. Engg. Div., ASCE, Vol. 97, No. SM9, pp. 1249-1273.

Seed, R. B., Lee, S. R., and Jong, H-L, 1988. *Penetration and Liquefaction Resistances: Prior Seismic History Effects*, J. Geot. Engg. Div., ASCE, Vol. 114, No. GT6, June, pp. 691-694.

Sereeter, V. L., Wglie, E. B., and Richard, F. E., Jr, 1974. *Soil Motion Computation by Characteristics Method*, J. Geot. Engg. Div., ASCE, Vol. 100, No. GT3, pp. 247-263.

Skotheim, A., Janbu, N., and Senneset, K., 1985. *Determination of Effective Stress-Based Shear Strength Parameters from Static and Cyclic Triaxial Tests*, Strength

- Testing of Marine Sediments: Laboratory and In-Situ Measurements. ASTM STP 883, American Society for Testing and Materials, Philadelphia, pp. 318-335.
- Sladen, J. A., D'Hollander, R. D., and Krahn, J., 1985. *The Liquefaction of Sands, a Collapse Surface Approach*, Can. Geot. J., Vol. 22, pp. 564-578.
- Sladen, J. A., and Oswell, J. M., 1989. *The Behavior of Very Loose Sand in the Triaxial Compression Test*, Can. Geot. J., Vol. 26, No. 2, pp. 103-113.
- Stokoe, K. H., Isenhower, W. M., and Hsu, J. R., 1980. *Dynamic Properties of Offshore Silty Samples*, Proc., Offshore Technology Conference, OCT 3771, pp. 289-302.
- Stokoe, K. H., and Seed, H. B., 1978. *Dynamic Response of San Francisco Bay Mud*, Proc., the Earthquake Engineering and Soil Dynamics Conference, Pasadena, Ca., ASCE, Vol. II, June, pp. 940-959.
- Thiers, G. R., and Seed, H. B., 1969. *Strength and Stress-Strain Characteristics of Clays Subjected to Seismic Loading Conditions*, ASTM Special Technical Publication 450, pp. 3-56.
- Townsend, F. C. and Mulilis, J. P., 1978. *Liquefaction Potential of Sands Under Static and Cyclic Loadings*, U.S. Army Engineer Waterways Experiment Station. Corps of Engineers, Vicksburg, Miss., Report.
- Vucetic, M., 1988. *Normalized Behavior of Offshore Clay under Uniform Cyclic Loading*, Can. Geot. J., Vol. 25, No. 1, pp. 33-41.
- Vucetic, M., and Dobry, R., 1991. *Effect of Soil Plasticity on Cyclic Response*, J. Geot. Engg. Div., ASCE, Vol. 117, No. GT1, pp. 89-107.

Vucetic, M., and Dobry, R., 1988. *Degradation of Marine Clays under Cyclic Loading*, Journal of Geotechnical Engineering Division, ASCE, Vol. 114, No. 2, Feb., pp. 133-149.

Vucetic, M., and Thilakaratne, V., 1987. *Degradation of Clay Stiffness under Irregular Cyclic Loading*, Proc., Int. Symp. on Geot. Engg. of Soft Soils, Mexico City, pp. 155-162.

Walberg, F. C., 1977. *Soils—Investigation of Effects of Freezing Sand Samples*, Presentation 12, Division Laboratory Conference, Corps of Engineers, Dallas, April.

Wang, J. L., Vivatrat, V., and Ruser, J. R., 1982. *Geotechnical Properties of Alaska OC Marine Silts*, Proc., Offshore Technology Conference, Houston, Texas, Vol. 4, OTC Paper No. 4412.

Wang, M-S., 1972. *Liquefaction of Triaxial Sand Samples Under Different Frequencies of Cyclic Loading*, M.Eng. Thesis, University of Western Ontario, May.

Wong, R. T., Seed, H. B., and Chan, C. K., 1975. *Cyclic Loading Liquefaction of Gravelly Soils*, Journal of Geotechnical Engineering Division, ASCE, Vol. 101, No. GT6, June, pp. 571-583.

Appendix A

A.1 Derivation of Equations 4.3 and 4.4

$$\begin{aligned}
 \epsilon(\bar{t}) &= \sigma * J(t) \\
 &= \sigma_d \sum_{k=0}^{N-1} [I(t - 2kT) - I(t - 2kT - T)] * J(t) \\
 &= \sigma_d \sum_{k=0}^{N-1} [J(t - 2kT) - J(t - 2kT - T)] + \\
 &\quad \sigma_d * [J(\bar{t}) - J(\bar{t} - T)I(\bar{t} - T)]
 \end{aligned} \tag{A.1}$$

i.e.,

for the loading period

$$\begin{aligned}
 \epsilon(\bar{t}) &= \sigma_d \sum_{k=0}^{N-1} [J(t - 2kT) - J(t - 2kT - T)] + \sigma_d * [J(t - 2NT)] \\
 &= \sigma_d \sum_{k=0}^{N-1} [J(t - 2kT) - J(t - 2kT - T)] + \sigma_d * [J(\bar{t})]
 \end{aligned}$$

for the unloading period

$$\begin{aligned}
 \epsilon(\bar{t}) &= \sigma_d \sum_{k=0}^{N-1} [J(t - 2kT) - J(t - 2kT - T)] + \\
 &\quad \sigma_d * [J(t - 2NT) - J(t - 2NT - T)] \\
 &= \sigma_d \sum_{k=0}^{N-1} [J(t - 2kT) - J(t - 2kT - T)] + \\
 &\quad \sigma_d * [J(\bar{t}) - J(\bar{t} - T)]
 \end{aligned} \tag{A.2}$$

where \bar{t} is the local time coordinate within one cycle, $\bar{t} = t - 2NT$, $0 \leq \bar{t} \leq 2T$.

A.2 Derivation of Equations 4.7 and 4.8

The creep function for the Maxwell Model is given by (Lockett, 1972)

$$J(t) = \left(\frac{1}{\mu} + \frac{1}{\eta}t\right) * I(t) \quad (\text{A.3})$$

By substituting this equation for $J(t)$ in Eqn (A.2), the following can be derived:
for the loading period

$$\begin{aligned} \epsilon(\bar{t}) &= \sigma_d \sum_{k=0}^{N-1} \left[\left(\frac{1}{\mu} + \frac{1}{\eta}(t - 2kT)\right) - \left(\frac{1}{\mu} + \frac{1}{\eta}(t - 2kT - T)\right) \right] + \\ &\quad \sigma_d * \left[\frac{1}{\mu} + \frac{1}{\eta}\bar{t} \right] \\ &= \sigma_d \sum_{k=0}^{N-1} \frac{T}{\eta} + \sigma_d * \left[\frac{1}{\mu} + \frac{1}{\eta}\bar{t} \right] \\ &= \sigma_d \frac{NT}{\eta} + \sigma_d * \left[\frac{1}{\mu} + \frac{1}{\eta}\bar{t} \right] \\ &= \left(\frac{1}{\mu} + \frac{NT}{\eta} + \frac{\bar{t}}{\eta} \right) \sigma_d \end{aligned} \quad (\text{A.4})$$

for the unloading period

$$\begin{aligned} \epsilon(\bar{t}) &= \epsilon(\bar{t})_{loading} - \sigma_d \left(\frac{1}{\mu} + \frac{1}{\eta}(\bar{t} - T) \right) \\ &= \sigma_d \left[\left(\frac{1}{\mu} + \frac{NT}{\eta} + \frac{\bar{t}}{\eta} \right) - \left(\frac{1}{\mu} + \frac{1}{\eta}(\bar{t} - T) \right) \right] \\ &= \sigma_d \left(\frac{NT}{\eta} + \frac{T}{\eta} \right) \\ &= \frac{(N+1)T}{\eta} \sigma_d \end{aligned} \quad (\text{A.5})$$

A.3 Derivation of Equations 4.10 and 4.11

The creep function of the Kelvin-Voigt Model is (Lockett, 1972)

$$J(t) = \frac{1}{\mu} (1 - e^{-\frac{\mu}{\eta}t}) I(t) \quad (\text{A.6})$$

Substitution of the above in Eqn (A.2) can lead to the deduction of the following:
for the loading period

$$\epsilon(\bar{t}) = \sigma_d \sum_{k=0}^{N-1} \left[\frac{1}{\mu} (1 - e^{-\frac{\mu}{\eta}(t-2kT)}) - \frac{1}{\mu} (1 - e^{-\frac{\mu}{\eta}(t-2kT-T)}) \right] +$$

$$\begin{aligned}
& \sigma_d * \frac{1}{\mu} (1 - e^{-\frac{\mu}{\eta} \bar{t}}) \\
= & \frac{\sigma_d}{\mu} \sum_{k=0}^{N-1} [-e^{-\frac{\mu}{\eta}(t-2kT)} + e^{-\frac{\mu}{\eta}(t-2kT-T)}] + \\
& \sigma_d * \frac{1}{\mu} (1 - e^{-\frac{\mu}{\eta} \bar{t}}) \\
= & \frac{\sigma_d}{\mu} (e^{\frac{\mu}{\eta} T} - 1) \sum_{k=0}^{N-1} e^{-\frac{\mu}{\eta}(t-2kT)} + \sigma_d * \frac{1}{\mu} (1 - e^{-\frac{\mu}{\eta} \bar{t}}) \\
= & \frac{\sigma_d}{\mu} (e^{\frac{\mu}{\eta} T} - 1) e^{-\frac{\mu}{\eta} t} \sum_{k=0}^{N-1} e^{\frac{2T\mu}{\eta} k} + \sigma_d * \frac{1}{\mu} (1 - e^{-\frac{\mu}{\eta} \bar{t}}) \\
= & \frac{\sigma_d}{\mu} (e^{\frac{\mu}{\eta} T} - 1) e^{-\frac{\mu}{\eta}(\bar{t}+2NT)} \frac{e^{\frac{2TN\mu}{\eta}} - 1}{e^{\frac{2T\mu}{\eta}} - 1} + \sigma_d * \frac{1}{\mu} (1 - e^{-\frac{\mu}{\eta} \bar{t}}) \\
= & \frac{\sigma_d(1 - e^{\frac{\mu}{\eta} T})(1 - e^{-\frac{2N\mu}{\eta} T})}{\mu(1 - e^{\frac{2\mu}{\eta} T})} e^{-\frac{\mu}{\eta} \bar{t}} + \\
& \frac{\sigma_d}{\mu} (1 - e^{-\frac{\mu}{\eta} \bar{t}})
\end{aligned} \tag{A.7}$$

for the unloading period

$$\begin{aligned}
\epsilon(\bar{t}) &= \epsilon(\bar{t})_{loading} - \frac{\sigma_d}{\mu} (1 - e^{-\frac{\mu}{\eta}(\bar{t}-T)}) \\
&= \frac{\sigma_d(1 - e^{\frac{\mu}{\eta} T})(1 - e^{-\frac{2N\mu}{\eta} T})}{\mu(1 - e^{\frac{2\mu}{\eta} T})} e^{-\frac{\mu}{\eta} \bar{t}} + \\
&\quad \frac{\sigma_d}{\mu} (1 - e^{-\frac{\mu}{\eta} \bar{t}}) - \frac{\sigma_d}{\mu} (1 - e^{-\frac{\mu}{\eta}(\bar{t}-T)}) \\
&= \left[\frac{\sigma_d(1 - e^{\frac{\mu}{\eta} T})(1 - e^{-\frac{2N\mu}{\eta} T})}{\mu(1 - e^{\frac{2\mu}{\eta} T})} + \right. \\
&\quad \left. \frac{\sigma_d}{\mu} (e^{\frac{\mu}{\eta} T} - 1) \right] e^{-\frac{\mu}{\eta} \bar{t}}
\end{aligned} \tag{A.8}$$

Appendix B

B.1 Typical Results of u/σ_c (or u/σ_p' for OC specimens) vs N and ϵ_a vs N in Chapter 7

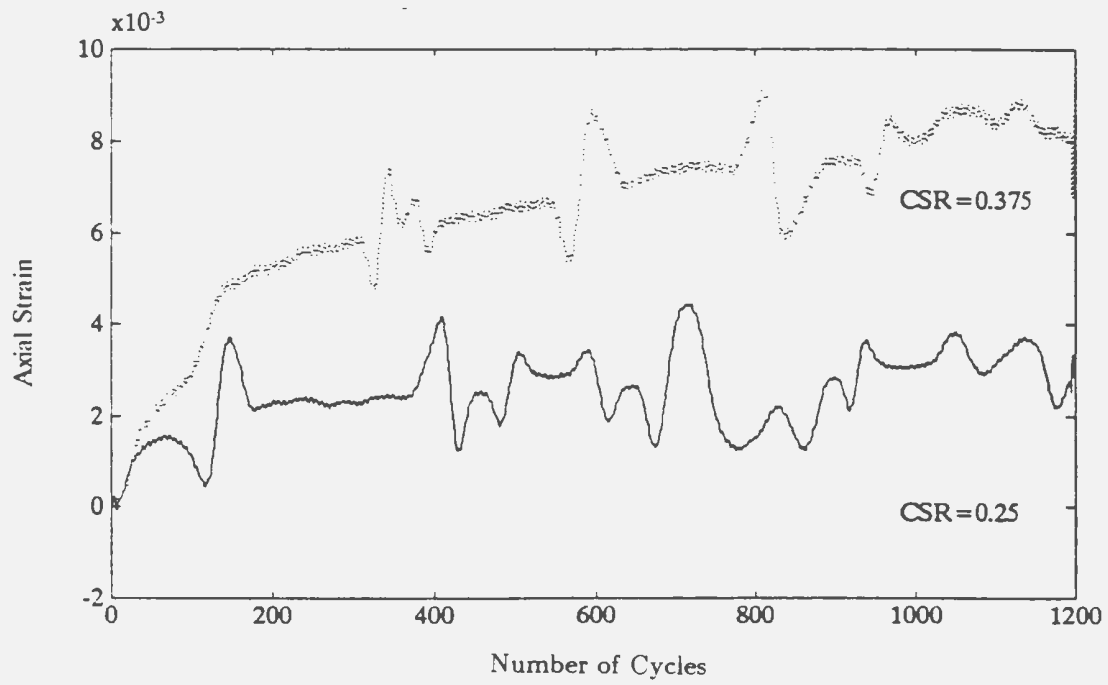
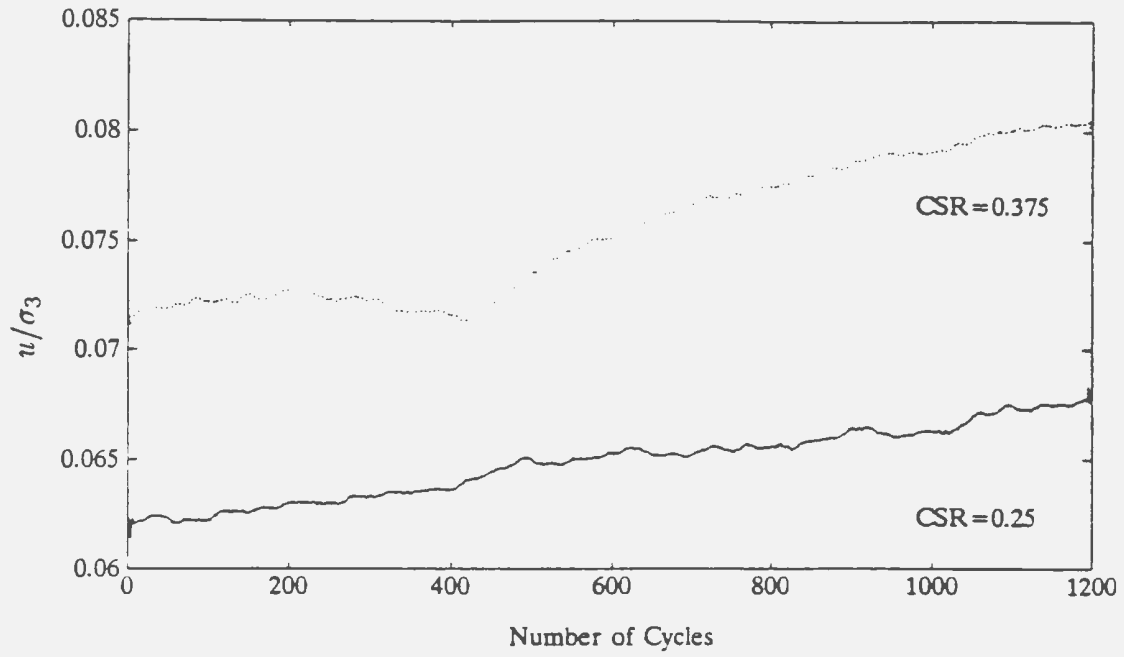


Figure B.1: Test Results from Overconsolidated Nerlerk Mud (OCR=2).

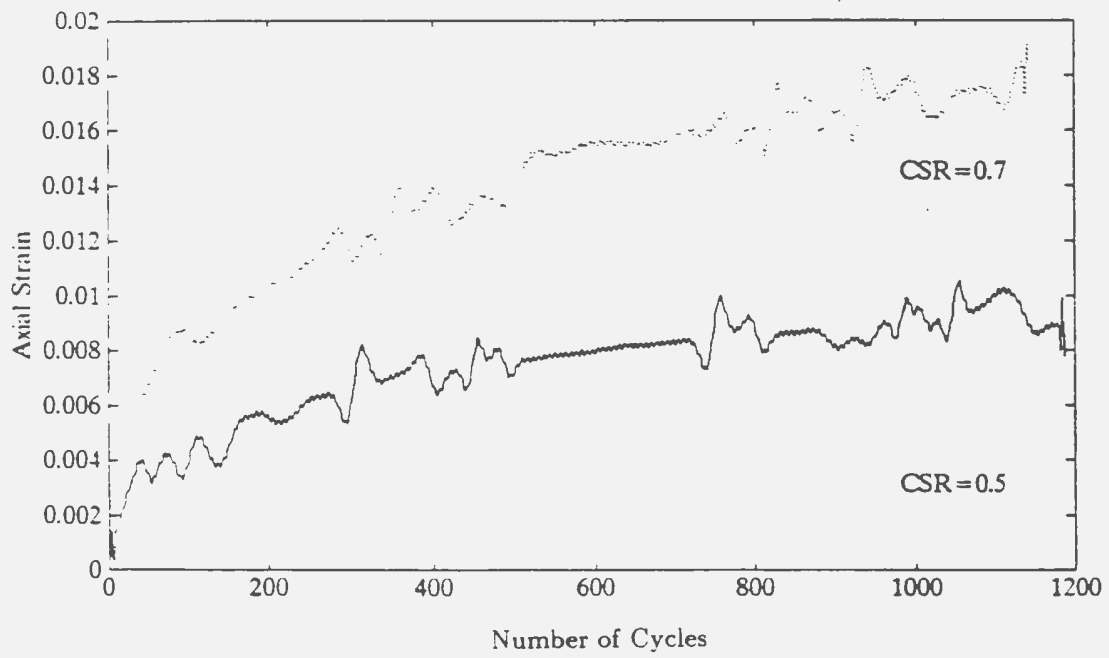
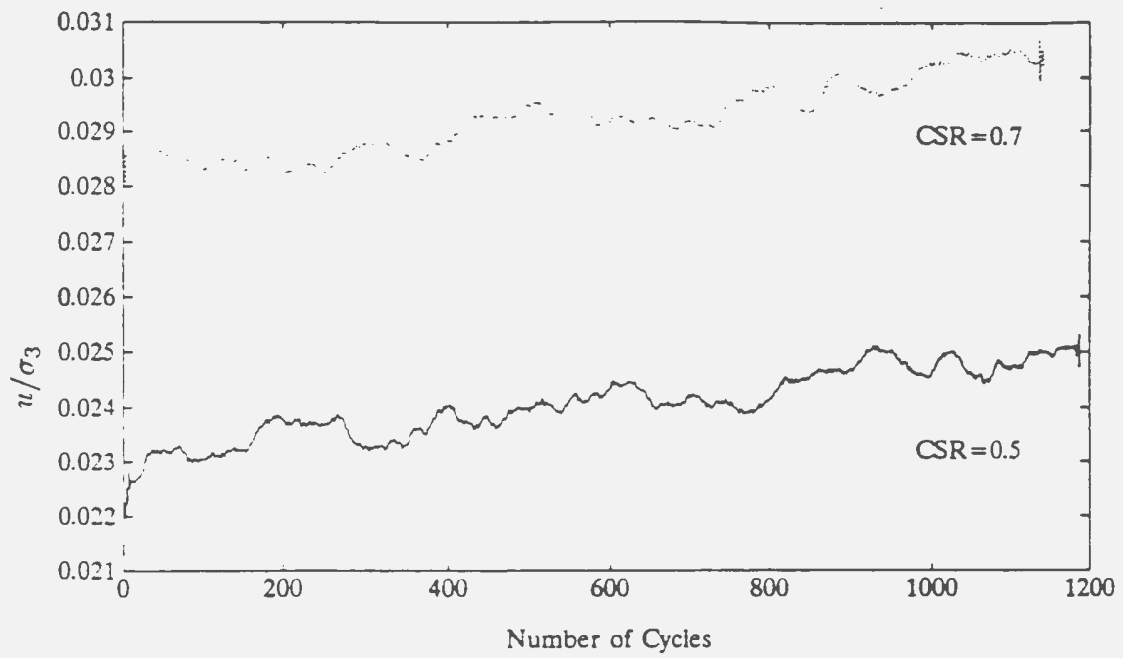


Figure B.2: Test Results from Overconsolidated Nerlerk Mud (OCR=8).

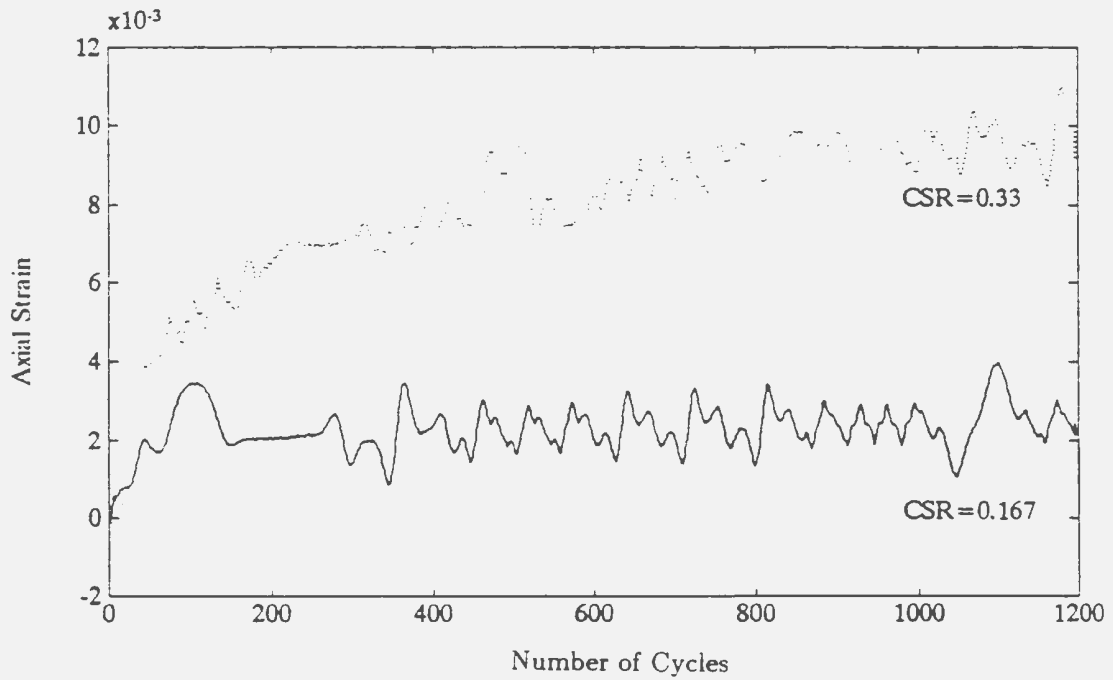
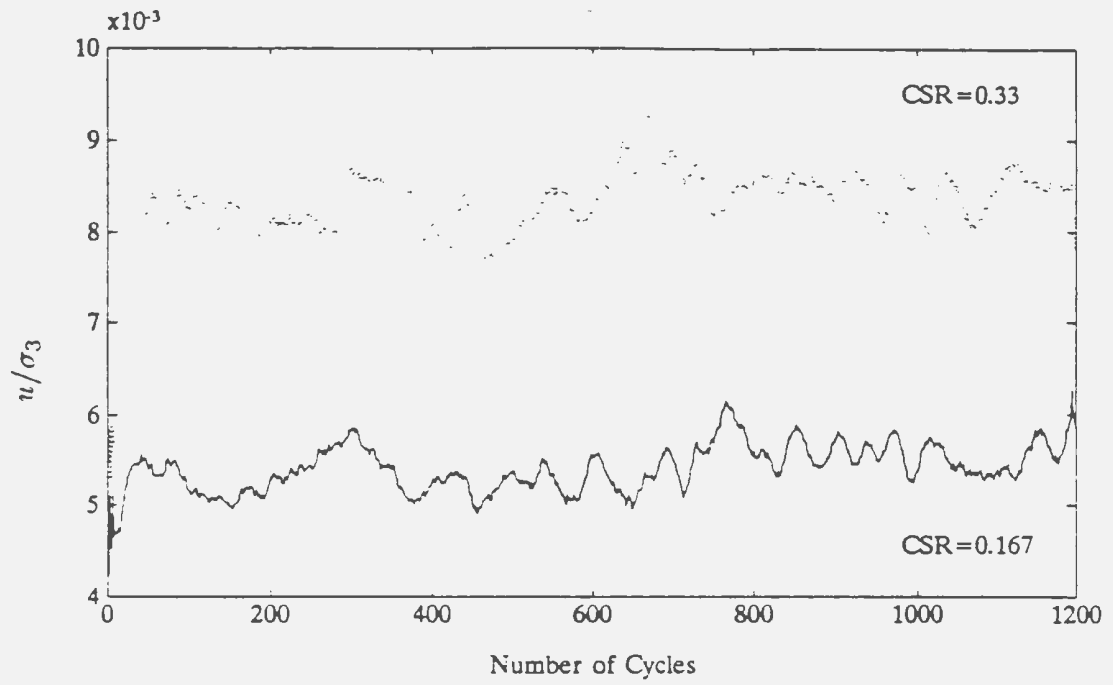


Figure B.3: Test Results from Normally Consolidated Marine Silt.

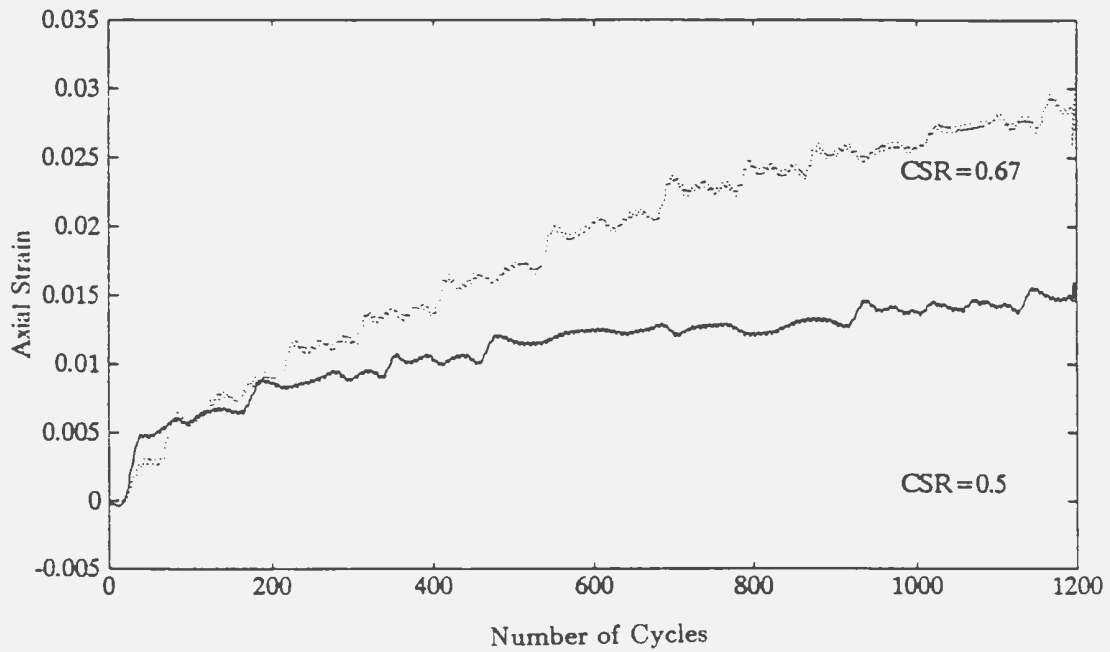
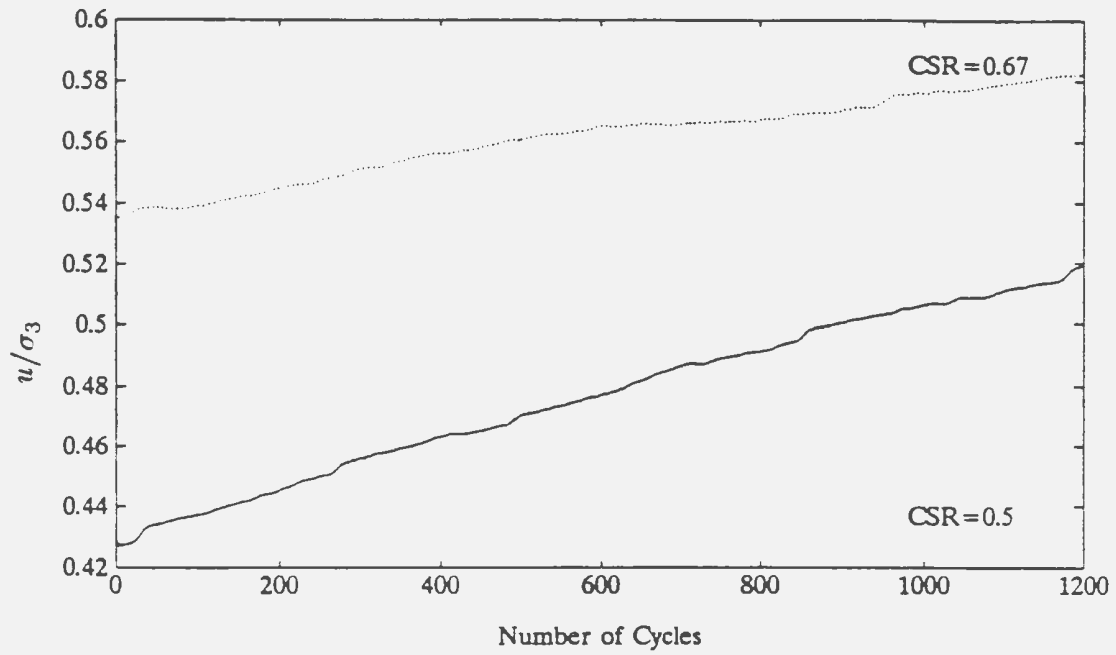


Figure B.4: Test Results from Overconsolidated Marine Silt (OCR=4).

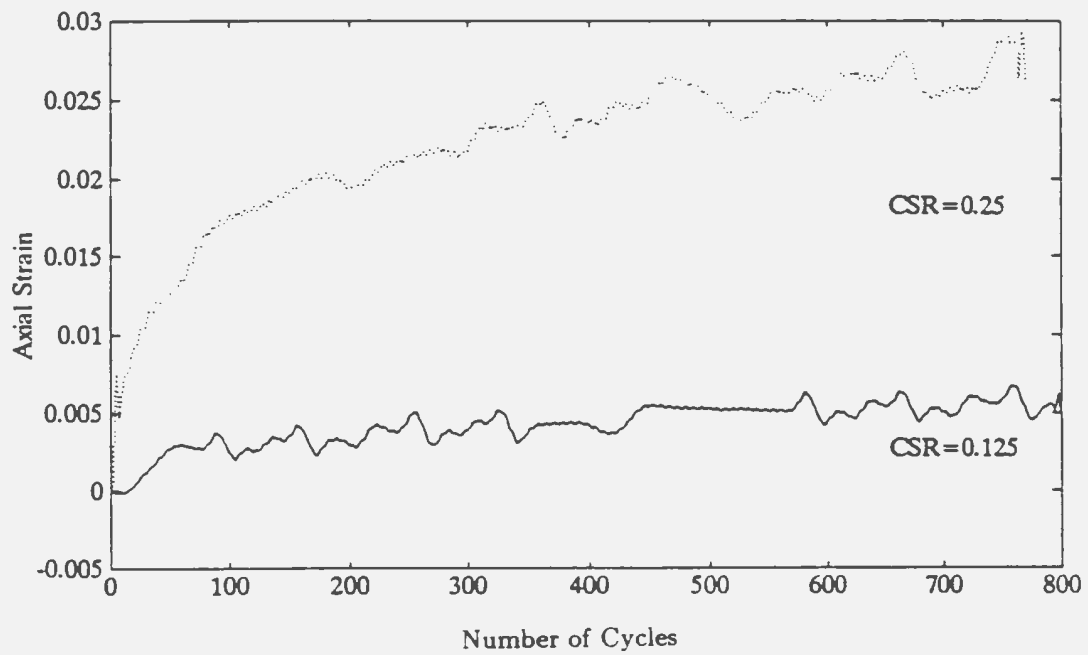
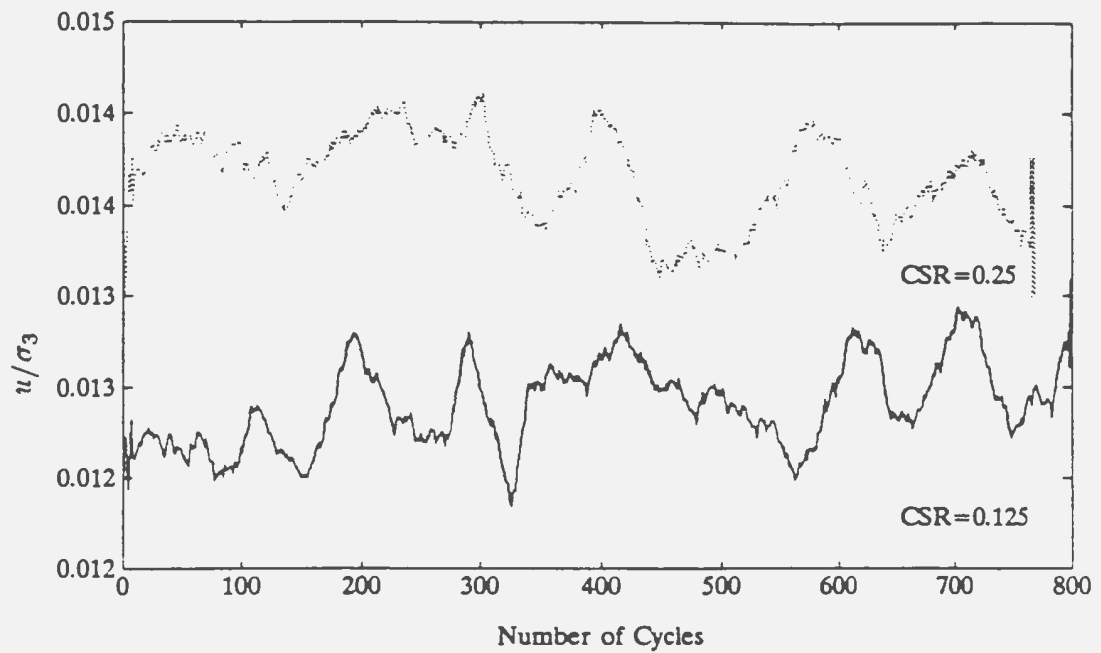


Figure B.5: Test Results from Normally Consolidated Shelf Clay.

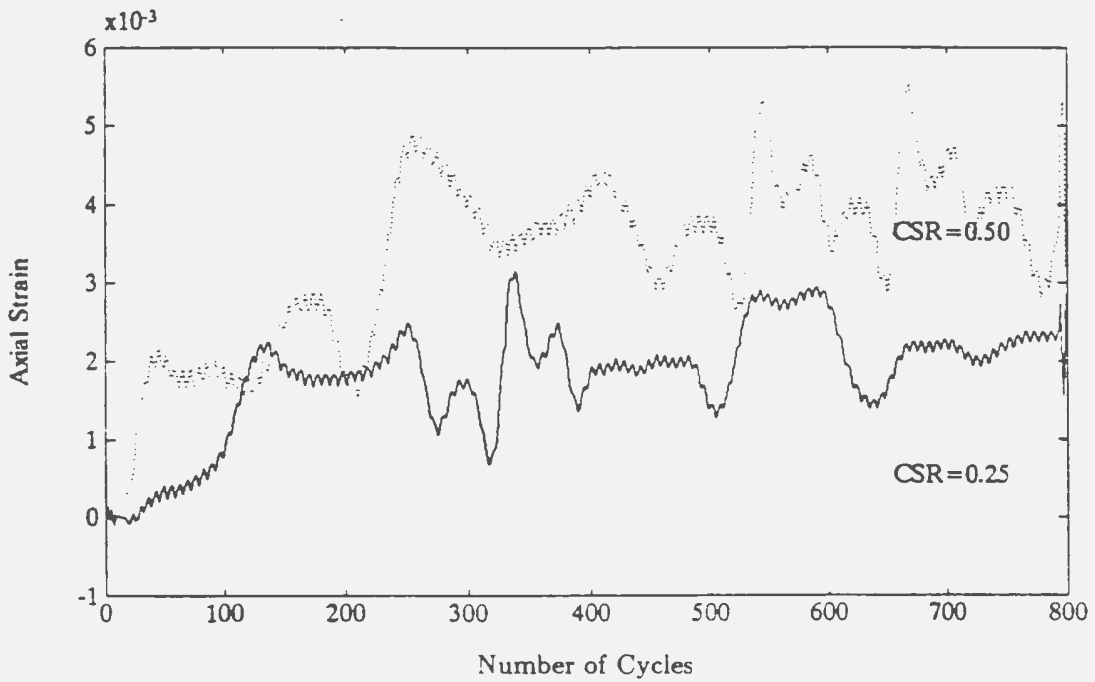
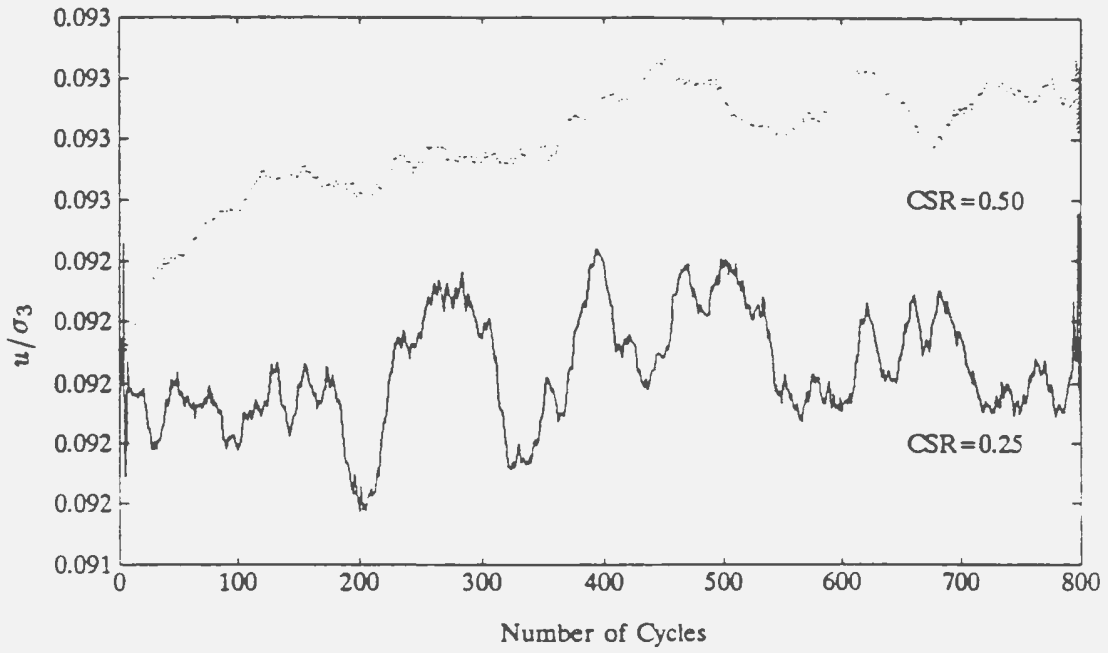


Figure B.6: Test Results from Overconsolidated Shelf Clay ($OCR=2$).

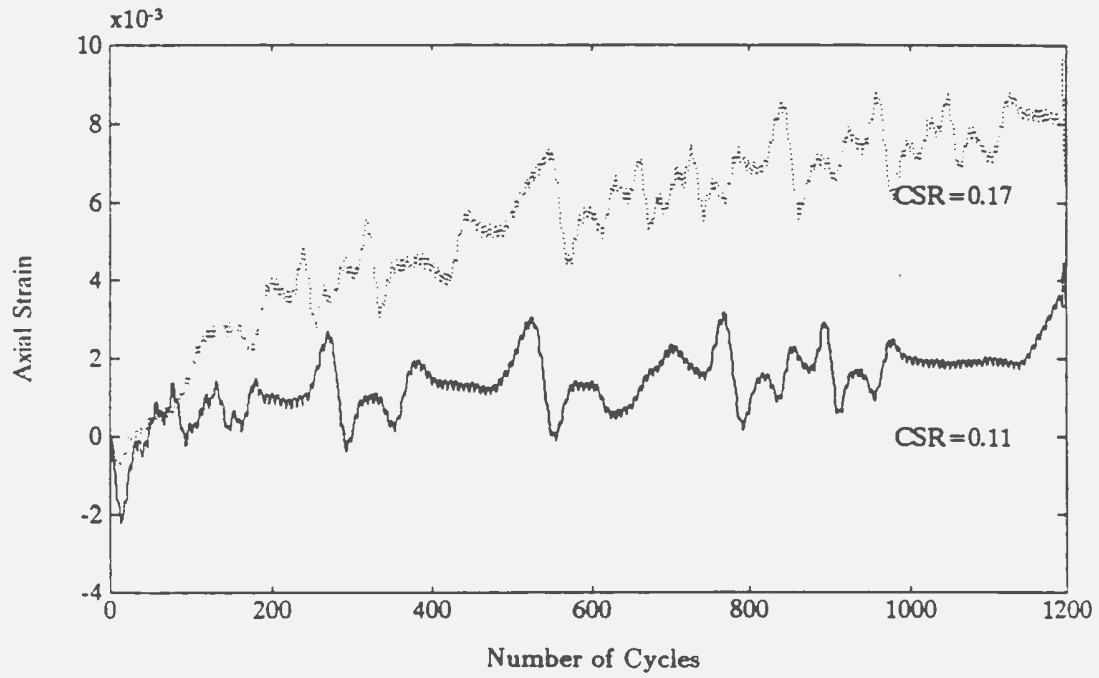
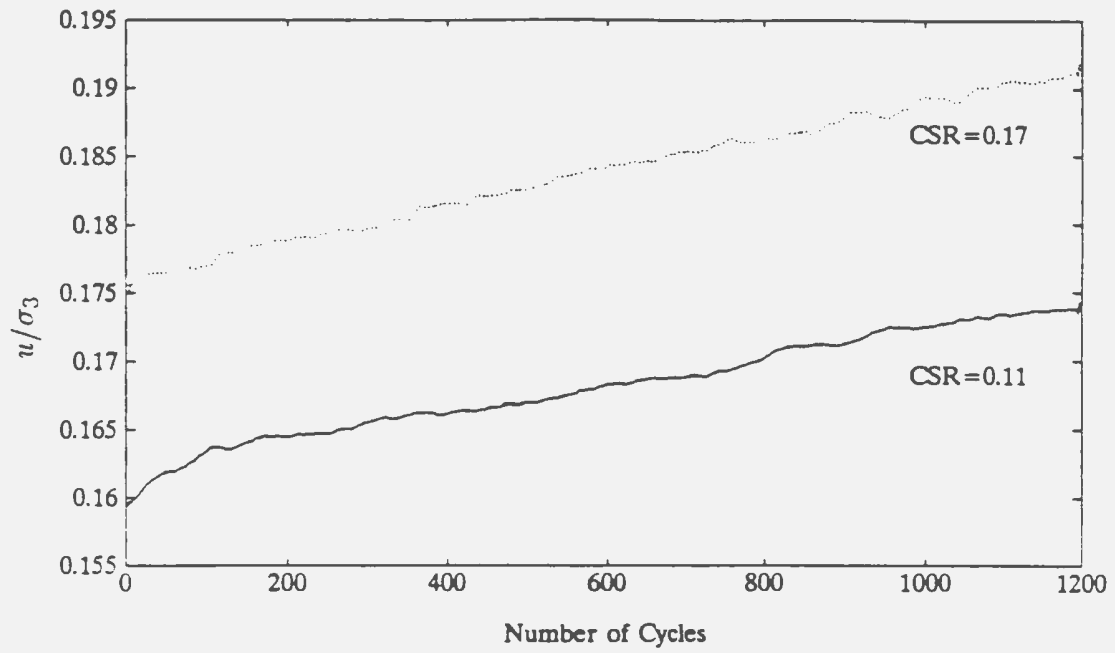


Figure B.7: Test Results from Slightly Overconsolidated Shelf Silty Clay (OCR=1.1).

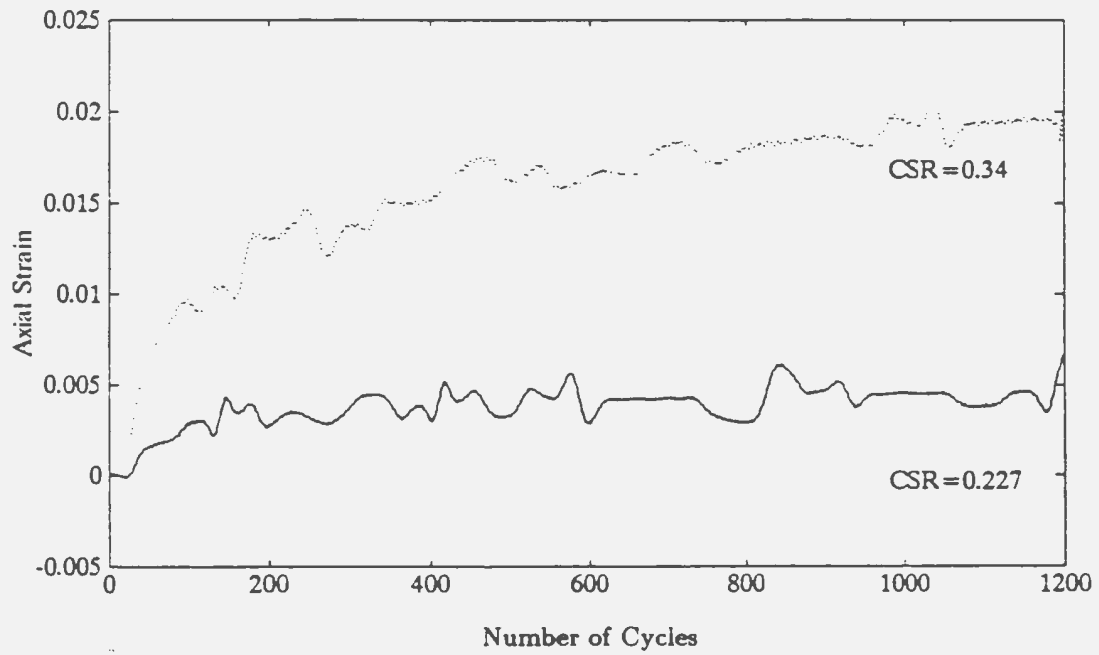
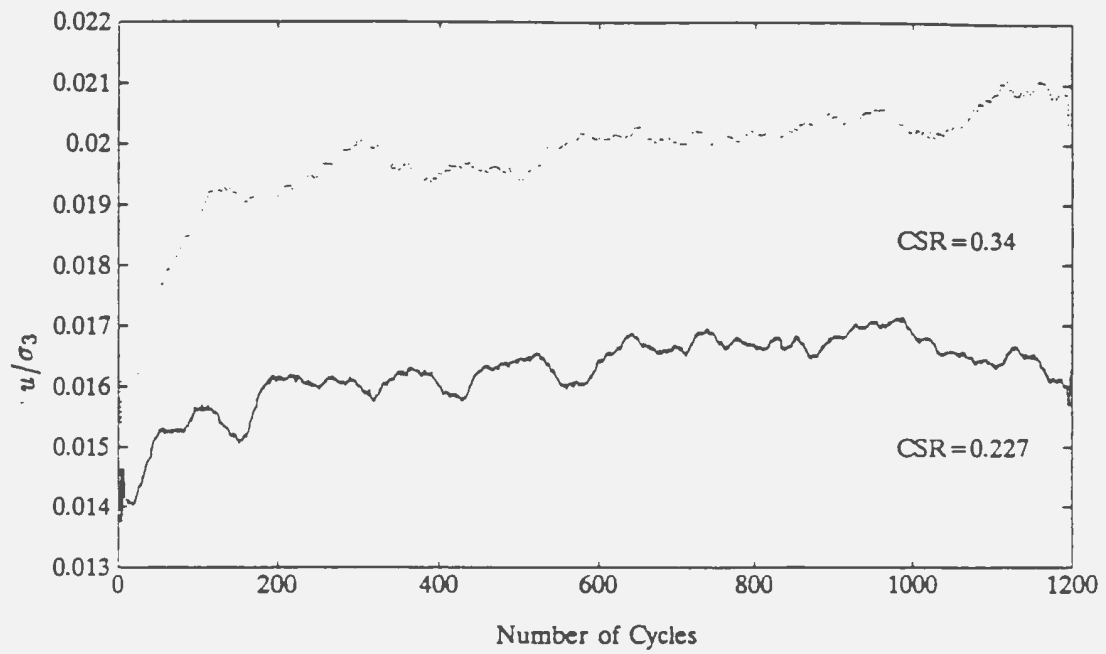


Figure B.8: Test Results from Overconsolidated Shelf Silty Clay (OCR=4.4).

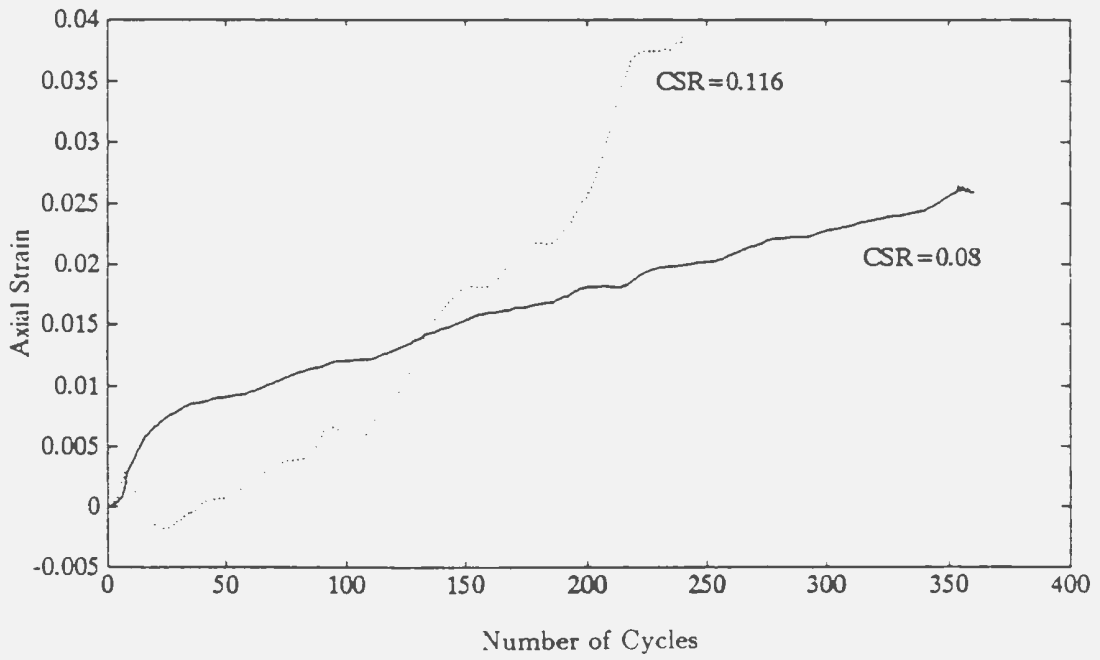
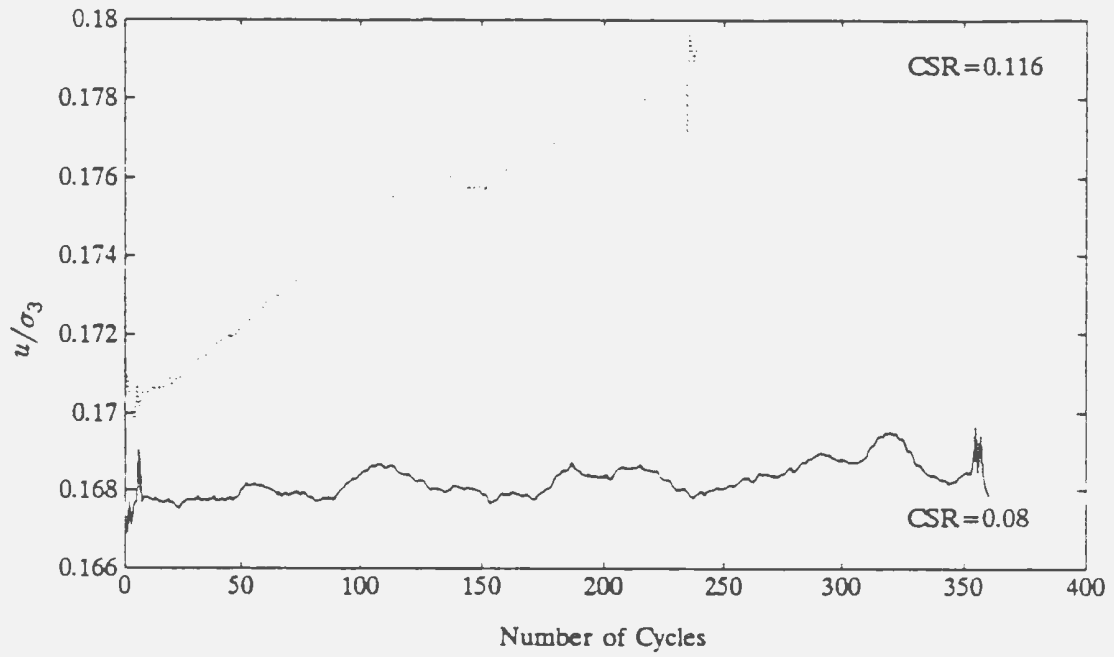


Figure B.9: Test Results from Normally Consolidated Beaufort Sea Clay.

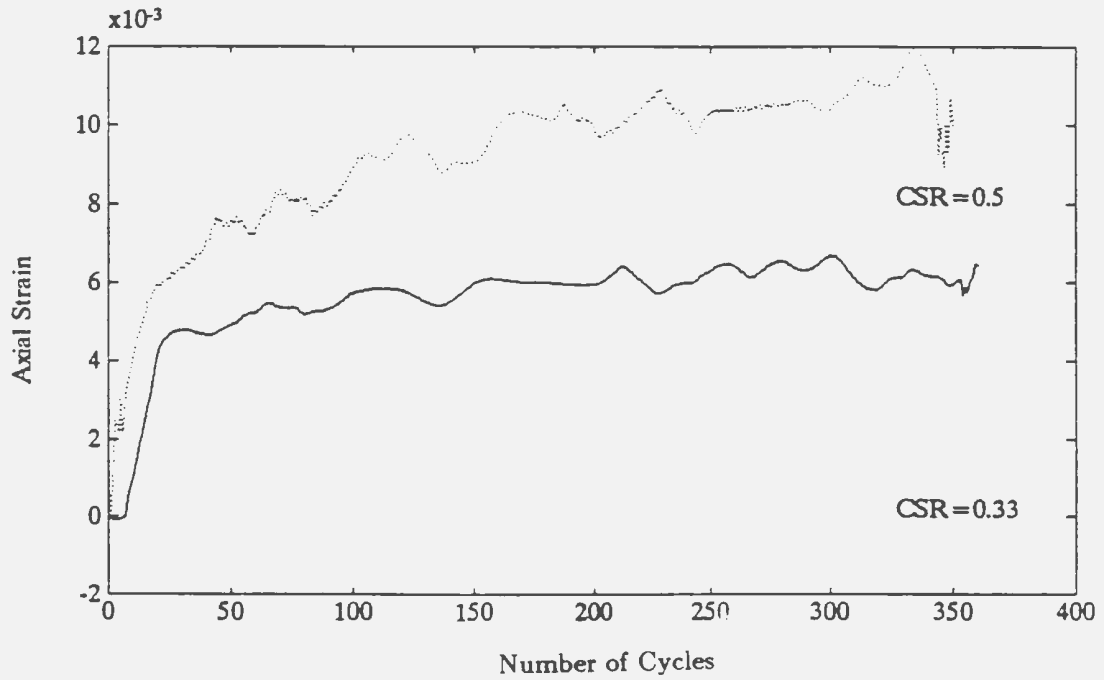
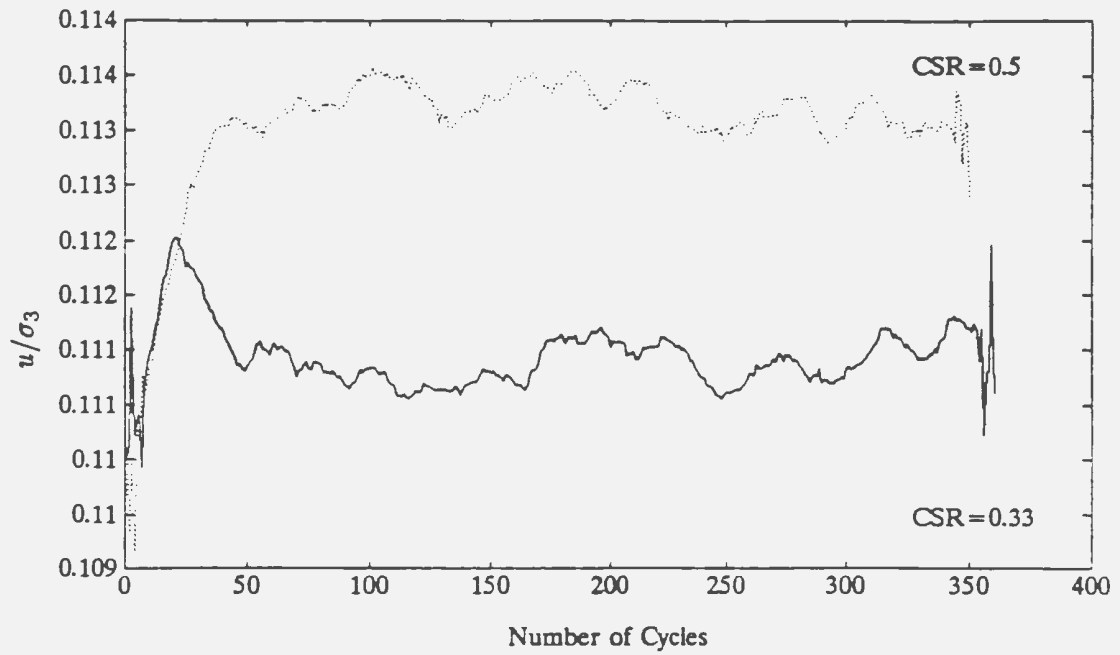


Figure B.10: Test Results from Overconsolidated Beaufort Sea Clay (OCR=4).

